MICROFLUIDIC DEVICE DESIGN INFORMED BY RED BLOOD CELL MORPHOLOGY FOR GLOBAL BLOOD DIAGNOSTICS AND BANKING

by
Kian A. Torabian

A dissertation submitted to The Department of Biomedical Engineering,
Cullen College of Engineering
in partial fulfillment of the requirements for the degree of

Doctor of Philosophy

in Biomedical Engineering

Chair of Committee: Dr. Sergey S. Shevkoplyas

Committee Member: Dr. Mohammad Reza Abidian

Committee Member: Dr. Howard Gifford

Committee Member: Dr. Sheereen Majd

Committee Member: Dr. Tianfu Wu

Committee Member: Dr. Vivien Sheehan M.D.

University of Houston
May 2020

ACKNOWLEDGEMENTS

I would first and foremost like to thank my colleagues and advisors in Dr. Sergey Shevkoplyas's lab, including of course Dr. Shevkoplyas, from whose example I learned the value of perseverance in research. Dr. Shevkoplyas has shown the patience of someone who charismatically embraces the uncertainty in this field in a way that I wish to emulate. Additionally, it is clear that he, like the UH BME department in general, values a diversity of backgrounds and experiences, and I have benefitted greatly from the opportunity to learn within such a global-minded environment. On that note, I would like to express my gratitude to Dr. Metin Akay, and The University of Houston, for encouraging and enabling me to attend conferences and seminars in the US and in Turkey, and would particularly like to acknowledge the financial support I received through The Embassy of France in the US and Dr. Shevkoplyas to conduct a nearly yearlong research endeavor in France. Moreover, in Montpellier and Lyon, Drs. Manouk Abkarian and Phillipe Connes generously opened up their laboratories and homes to me.

I would also like to thank Dr. Sean Gifford, and Dr. Vivien Sheehan M.D./PhD, for serving as additional advisors, Dr. Gifford in the lab, and Dr. Sheehan as a clinical collaborator, through much of the work we conducted in Houston. Their kindness and willingness to make themselves available was a great support to me. Finally, I would like to thank the additional members of my committee, Drs. Howard Gifford, Tianfu Wu, Sheereen Majd, and Mohammad Reza Abidian, and my academic advisors Drs. Charlotte Waits and Ting Chen, for their enthusiastic and thoughtful presence through the tasks and events associated with my PhD.

ABSTRACT

Just as blood diagnostic tests are ubiquitous in the clinic, blood component transfusions are among the most commonly performed medical procedures at the bedside. The many devices designed to process blood often rely on microscale flow of the complex non-Newtonian fluid. With approximately 40% of human blood comprised of red blood cells, flow dynamics are largely influenced by these relatively dense particles. Their delicate biconcave shape is essential to their deformability, aggregability, and overall viability, allowing them to bend, shear, expand, and stack as they navigate the microvasculature to deliver oxygen to surrounding tissues. As a result, shape and its many surrogates not only serve as biomarkers for their quality, but also can be exploited to improve diagnostic and blood banking devices.

In this work we study red blood cells with altered morphology in various forms of sickle cell disease and in animal models with uniquely adapted vascular systems, and use our findings to develop three devices with applications in blood banking and diagnostics: a simple gravity-based device to replace industrial centrifuges that wash stored red blood cells prior to transfusion, a multi-layered microfluidic platform to separate whole blood into its component blood transfusion products, and a paper-based diagnostic device for the altered hemoglobin molecule responsible for sickle cell disease. We explore the limitations and challenges associated with current technologies used to study red blood cell deformability and aggregation, ranging from micropipettes to ektacytometers and aggregometers, with respect to balancing diagnostic robustness, methodological throughput, and access and affordability. Additionally, we take advantage of inexpensive and biomimetic microfluidic platforms to inform a design process for global health applications, considering the potential scope of these devices to improve access to some of the most widely used biomedical tools.

TABLE OF CONTENTS

LIST OF TABLES

LIST OF FIGURES

LIST OF ABBREVIATIONS

3D	three dimensional
ACS	acute chest syndrome
ADP	adenosine diphosphate
AFM	atomic force microscopy
AMVN	artificial microvascular network
AUC	area under the curve
CIF	controlled incremental filtration
CPD	citrate phosphate dextrose
CV	coefficient of variation
EI	elongation index
ELISA	enzyme linked immunosorbent assay
GASP	glucose albumin saline phosphate
Hb	hemoglobin
HCT	hematocrit
HPLC	high performance liquid chromatography
HS	sodium hydrosulfite
HSA	human serum albumin
HU	hydroxyurea
IgA	immunoglobulin A
LOD	limit of detection
LORRCA	laser optical rotational red cell analyzer
LOS	limit of stability
M1	no-shear aggregation
M2	shear aggregation
MCHC	mean corpuscular hemoglobin concentration
MCV	mean corpuscular volume
MPC	microfluidic platelet concentrator
MS	sodium metabisulfite
NO	nitric oxide
NPV	negative predictive value

PCA	principal component analysis
PDMS	polydimethylsiloxane
PPP	platelet poor plasma
PPV	positive predictive value
PR	perfusion rate
pRBC	packed red blood cell
PRP	platelet rich plasma
PVP	polyvinylpyrrolidone
RBC	red blood cell
ROC	receiver operating characteristic
SCA	sickle cell anemia
SCD	sickle cell disease
SCT	sickle cell trait
SD	standard deviation
TR	transverse ratio
TRAP	thrombin receptor agonist peptide
WB	whole blood

INTRODUCTION

Red blood cell (RBC) morphology is a critical component of normal vascular functioning in humans. Under no stress, human RBCs take a unique biconcave discocytic shape, which optimizes surface to volume ratio to allow for large bending deformations as they flow through capillaries down to a quarter of the diameter of the discocyte's largest dimension. A number of biophysical conditions maintain the delicate osmotic balance and molecular interactions required to optimize RBC morphology for the delivery of oxygen and nutrients through the microvasculature to surrounding tissues. By understanding the relationship between these factors and their influence on blood flow, we can design devices that monitor or maintain healthy RBC perfusion when morphologically pathological RBCs are present. An effective approach to studying and manipulating small-scale flow is through the design of microfluidic devices that mimic specific aspects of the environment found in the microvasculature.

In this work we probe RBC shear deformability using ektacytometry and micropipette techniques, and describe its relationship to traditional hematological parameters, cell morphology, and flow and aggregation dynamics. We focus on morphological pathologies observed in the two most common forms of Sickle Cell Disease (SCD), *HbSS* and *HbSC* genotypes, and use animal models of llama, goat, and rooster RBCs as extreme examples of morphologies found in human hemoglobinopathies and other RBC membrane pathologies. Finally, we use these findings to model the flow and deformation dynamics of RBCs and related blood components in order to design

microfluidic devices that can diagnose, monitor, and filter RBCs with abnormal morphologies.

By comparing animal models with healthy and SCD human RBCs, we push the clinical limitations of the ektacytometer, a device that produces microfluidic Couette flow to shear RBCs and measures their resulting deformation via laser diffraction through a bulk population of RBCs. We found that the ability of the commonly used ektacytometry elongation index (EI) to predict flow patterns and perfusion rate through an artificial microvascular network (AMVN) in polydimethylsiloxane (PDMS) is limited to RBCs within a normal range of morphology and deformability. Further, we used an anomalous laser diffraction model on the ektacytometry diffraction patterns to characterize miscalculation of EI for RBCs with properties unsuitable for standard ektacytometry. We could then assess the limitations of these techniques to monitor the clinical severity of SCD and other pathologies that result from morphologically aberrant RBCs.

Next we apply our findings to develop devices that detect *HbSS* genotype RBCs, and filter blood components and pathological or poorly preserved populations of RBCs based on osmotic stability, size, and morphology. We modeled the sedimentation of RBCs due to gravity in laminar flow, allowing us to prototype a high-throughput microfluidic washing device. This device could be used at the bedside not only to better preserve packed RBC (pRBC) units by eliminating the wasteful process wherein hospitals coordinate with blood bank centrifuge washers, but also to remove morphologically abnormal RBCs by bursting those that are osmotically rigid and skimming those that are non-discocytic and unable to align into fast-sedimenting rouleaux. We also studied the effect of a novel high-throughput microfluidic device for

controlled incremental filtration (CIF) of platelets from plasma, on RBC EI and markers of platelet aggregation and plasma quality. Finally, we reformulate a paper microfluidic diagnostic device that traps HbS polymers to allow visual screening of sickle cell trait (SCT, or *HbAS*) and SCD blood drops by substituting sodium hydrosulfite (HS) with a higher concentration of sodium metabisulfite (MS), and produce a test kit with accessible off-the-shelf consumables and opensource diagnostic software, so that it can be accessed and stored without refrigeration or proprietary dependencies in the limited-resource settings where SCD is most common and least diagnosed.

Taken together, our findings on RBC morphology and the microfluidic devices they inspired in this work underscore the need for translation of techniques that quantify RBC deformability into medical devices. Since rigidity is a complex characteristic of RBCs with convolved biophysical influences, it can be used to inform the design of a range of devices. Throughout this work, we apply design thinking methodology developed by Ideo, a global design company, and Stanford d.school by using need-based, divergent thinking in our study of RBC morphology in chapters 1 and 2, and convergent thinking to build devices evaluated on their desirability, viability, and feasibility in chapters 3, 4 and 5. We find that although microfluidic devices lend themselves to such translational work because their production process is largely automated and adaptable to complex biomimetic specifications with affordable materials, there are many additional challenges to harnessing the power of microfluidics for global health applications. Such challenges are front and center as we engineer and evaluate the microfluidic devices described in this work.

CHAPTER 1 THE COMPLEXITY OF STUDYING RBC DEFORMABILITY AND AGGREGATION TO PREDICT PHYSIOLOGICAL OUTCOMES: Evaluating the effects of novel treatments on RBC deformability and aggregation in *HbSS* and *HbSC* patients

1.1 Introduction

Red blood cell (RBC) deformability is a multi-faceted property affected by several biophysical components of the cell. It can refer to a cell's ability to fold, characterized by the bending modulus of the lipid membrane, its ability to expand, characterized by the stretching modulus of the lipid membrane, or its ability to elongate uniaxially, characterized by the shear modulus of the cytoskeleton. Perhaps the simplest method to get a measure of RBC deformability is via a commercial ektacytometer, which automatically shears RBCs in flow and measures their elongation. In this chapter we use this measure of RBC deformability to characterize one aspect of the efficacy of treatments for sickle cell disease (SCD), a pathology influenced by a decrease in the deformability of RBCs. We find that although ektacytometry data were consistent between the two commercially available ektacytometers, and between patient populations in France and the USA with the same variants of SCD, one drawback of its measurement of shear deformability is that it does not have any clear fundamental physical or physiological implications since populations of rigid non-ellipsoidal RBCs can rotate in the ektacytometer flow fields instead of elongate. We recognized that flow conditions influence measurements of deformability and aggregation since they are all altered in complex ways by RBC morphology. In this chapter, we discuss our findings on the

influence of two potentially novel treatments for SCD on RBC deformability and aggregation in the context of measurement methods that use different flow conditions during measurement.

1.2 Background

SCD results from a mutation in the β-globin subunit of the oxygen-carrying protein found in RBCs, hemoglobin (Hb), creating a hydrophobic region when the mutated protein, known as HbS, is deoxygenated that causes it to polymerize with other HbS molecules. HbS protects against malaria, however over 5% of carriers have SCD (~0.25% of the global population) (Modell & Darlison, 2008). Estimates of SCD mortality can be higher than 50%, most commonly before the age of 12, especially if left untreated (Makani et al., 2011). The multisystem pathologies associated with SCD, ranging from acute illness to chronic organ damage, largely occur because HbS polymers form rigid structures inside of RBCs, causing them to become brittle, misshapen, and dense over repeated cycles of deoxygenated polymer formation and oxygenated rescue (Rees, Williams, & Gladwin, 2010).

The most common form of SCD, sickle cell anemia (SCA), which accounts for approximately 70% of cases in Africans, is caused by homozygous inheritance of the β^S allele, referred to as *HbSS*. The vast majority of remaining cases diagnosable as SCD are caused by compound heterozygous inheritance of β^S along with another detrimental β-globin mutation, typically either β^C, resulting in the *HbSC* genotype, or one of many mutations that cause β-thalassemia (Rees et al., 2010).

Currently the only cure for SCD is bone marrow transplant, therefore many SCD patients are treated with regular RBC transfusions from healthy donors while they consider or wait for the possibility of a transplant. Alternatively, hydroxyurea (HU), a chemotherapy drug, is the only FDA-approved compound to treat SCD and is often used before resorting to chronic blood transfusions. In 1995 the MSH clinical trial validated HU efficacy in *HbSS*, but not in the large population of SCD patients with compound-heterozygous mutations and more variable though often less-severe clinical outcomes than those with SCA: for example the efficacy of HU in treating *HbSC* patients, who make up roughly 40% of the African American SCD population, and smaller proportions of other SCD populations, is unknown (Modell & Darlison, 2008).

Since the RBCs of SCD patients often block capillaries to cause silent strokes and painful crises, and break or lyse to cause anemia and facilitate infection, deformability and aggregation strength of SCD RBCs are potentially critical parameters in disease outcome. Thus, as part of a clinical study in collaboration with Baylor College of Medicine (the SCYTHE clinical trial), we measured the shear deformability under non-sickled, oxygenated conditions of *HbSC* RBCs from patients through their first month of HU therapy. Additionally, we quantified the long-term effects of HU and transfusion on *HbSS* patient RBC shear deformability, and conducted a preliminary study *in vitro* inspired by medical case reporting (Boga, Kozanoglu, Ozdogu, & Ozyurek, 2007, Nader, 2017 #125) to explore the potential for plasmapheresis, or plasma exchange transfusion, as a treatment to increase the shear deformability or decrease the aggregation strength of *HbSS* and *HbSC* RBCs. We hypothesized that the deformability or aggregation of these RBCs when oxygenated could indicate disease pathology and outcome since

deoxygenation would cause therapeutic efficacy results between sickling *HbSS* RBCs and non-sickling *HbSC* RBCs to be less directly comparable.

To measure shear deformability, we used bulk ektacytometer and single-cell micropipette techniques. In commercial ektacytometers, shear stress on each molecular layer of a viscous RBC suspending medium, calculated using Newton's Law of Viscosity as the product of the mean geometric shear rate in the measurement gap and the suspending medium viscosity, is measured against the commonly reported deformability metric from ektacytometry known as elongation index (EI), calculated as

$$\mathrm{EI} = \frac{length - width}{length + width} \tag{1.1}$$

of an ellipse fitted to the diffraction pattern caused by an RBC sheared in the medium where length is in the direction of shear or flow and width is orthogonal to length and the laser path. We use two common commercially available ektacytometers, the Rheoscan-D (RheoMeditech Inc., Seoul, Republic of Korea) and the LORRCA (RR Mechatronics, Zwaag, The Netherlands), enabling us to observe if EI is comparable between studies that use one or the other. We also performed the studies evaluating HU on a cohort of SCD patients in Houston, TX, USA, and the studies evaluating plasmapheresis on a cohort in Lyon, France, to further test the translatability of EI between different demographics and geographies. In a small subset of the Lyon, France cohort, we also probed shear deformability with a well-characterized micropipette technique that produces the shear moduli of measured RBCs (Evans, 1980).

To measure aggregation, we also explored methodologies across multiple scales from secondary bulk measurements to direct measurement of single aggregates, to provide a balance between feasibility, viability, and desirability. Focusing on feasibility,

we performed bulk measurements with an aggregometer (MA1, Myrenne, Roentgen, Germany), which quickly and simply measures changes in turbidity as RBCs aggregate in various flow conditions. Then, prioritizing viability or longevity of the measurements, we present proof-of-concept of novel methods to measure the fundamental physical constant of aggregation energy in massive RBC aggregates of hundreds of RBCs in dextran (O. Baskurt, Neu, & Meiselman, 2011; Cines et al., 2014) using micropipette and atomic force-microscopy (AFM) techniques (Chaudhuri, Parekh, Lam, & Fletcher, 2009; Guevorkian, Colbert, Durth, Dufour, & Brochard-Wyart, 2010). Third, we provide a schematic of a microfluidic device to quantify aggregates of tens of RBCs under biomimetic conditions, that would provide a desirable measure of aggregation with more direct clinical implications.

1.3 Materials and Methods

The study protocols were approved by the University of Houston, Université de Lyon, and Baylor College of Medicine institutional review boards. SCD venous whole blood in EDTA was collected from consenting volunteers in Lyon France, and in Houston, TX, USA and from patients enrolled in the SCYTHE Clinical Trial at Baylor College of Medicine. The France cohort samples were washed twice in PBS and resuspended at 40% RBC volume fraction, or hematocrit (HCT), in either autologous plasma, or in plasma from consenting, healthy (*HbAA*), ABO/Rh-matched volunteers. After resuspending washed RBCs in plasma, they were left to incubate for 20 minutes at room temperature before measurement.

Samples from the Texas cohorts of *HbSS* and *HbSC* patients were analyzed by slit flow ektacytometry (Rheoscan-D, RheoMeditech Inc., Seoul, Republic of Korea) within 8 hrs of collection, and randomly corroborated by cup-and-bob ektacytometry (LORRCA, RR Mechatronics, Zwaag, The Netherlands) using standard procedure. Samples in the France cohort were analyzed only by cup-and-bob ektacytometry, within 8 hrs of collection and compared to results from the Texas cohort. RBCs were suspended in isotonic, viscous PBS-polyvinylpyrrolidone (PBS-PVP), and shear forces ranging from 0.3-30 Pa were applied by parabolic velocity profiles that caused the RBCs to elongate. A laser shone through the center of hundreds of RBCs produced a diffraction pattern that was fitted with an elipse to find the major and minor axes (length and width) of the RBCs at different shear elongations. EI at 3 and 30 Pa is compared between the samples using Tukey's Test.

Given the potentially low sensitivity of bulk ektacytometry and lack of detection of differences among samples, even between SCD RBC populations with different genotypes and thus expected different EIs, we corroborated the bulk RBC population dependent EI metrics with single RBC micropipette measurements of shear modulus. Figure 1.1 shows a multiscale schematic diagram of a hydraulic micropipette set-up for comparing shear deformability of SCD and *HbAA* RBCs in each other's plasma. Two fluid reservoirs leveled with the stage start at equal hydrostatic pressure through a direct connection controlled by a valve (Fig. 1.1a). Shutting the valve and manipulating the height of one reservoir with a fine micrometer allows high resolution differential wet/wet pressure control and sensing (DP15, Validyne, Northridge, CA) in a PLL-PEG (Nanosoft Polymers, Winston-Salem, NC) coated micropipette (~2 μm tip diameter) used to aspirate

the center of an RBC to measure shear deformability. Microcontrollers control the position of micropipettes in a chamber formed with rubber walls, a coverslip, and a PLL-PEG coated slide (Fig. 1.1b). A third reservoir is connected to a large micropipette (~50 μm diameter) that can change the plasma surrounding the RBC (Fig. 1.1c). The method described by Evans et al. (Evans, 1980), used a filamented borosilicate glass capillary (Cole-Parmer, Vernon Hills, IL) pulled (P-1000, Sutter Instruments, Novato, CA) and forged (MF-900, Narishige, Tokyo, Japan) into a micropipette with a ~2μm inner diameter and a flat circular tip with low gradation in the area where the RBC will be aspirated. Pipettes were cleaned in piranha solution, coated with PLL-PEG to prevent membrane adhesion, and filled with isotonic PBS. Two water reservoirs were attached to the micropipette through a pressure transducer linked to a multimeter (CD23, Validyne, Northridge, CA) calibrated to represent pressure difference between the reservoirs. The height of the reservoirs relative to the phase microscopy stage and to each other was controlled with translational stages connected to a micromanipulator rig (Fig. 1.1a). Valves were used to equalize or maintain hydrostatic pressure difference between the reservoirs. Micromanipulators also controlled the position of the micropipette relative to a sample holder (Fig. 1.1b) with RBCs in autologous plasma. To perform measurement, individual RBCs were suctioned to the micropipette at the non-stressed area of the discocyte, away from high curvature at the edges, and negative pressure was gradually increased by lowering the reservoir attached to the micropipette relative to the other reservoir, taking images and noting corresponding pressure on the multimeter for each image. After images at a range of pressures were taken, the same RBC was maintained against the pipette while a larger pipette (~50μm inner diameter) filled with plasma from

another Hb genotype was brought close to the RBC (Fig. 1.1c) with its pressure adjusted with yet another hydrostatic reservoir to produce a very low flow of exchange plasma in the area surrounding the RBC, before another set of images over a range of pressures was taken. The Skalak *et al.* law relating length of RBC insertion into the micropipette, L, to suction pressure in the pipette, P, for a given pipette inner radius, R_p, was used to calculate the linear RBC shear modulus (Dimitrakopoulos, 2012).

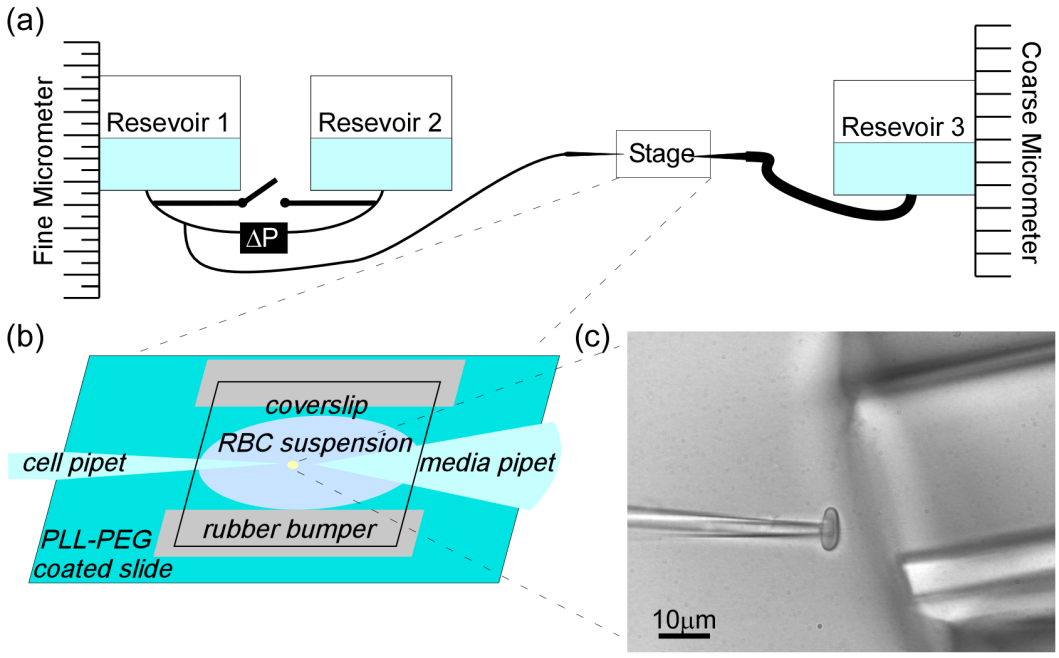

Figure 1.1: Multiscale schematic diagram of hydraulic micropipette set-up for comparing shear deformability of sickle cell disease (SCD) and healthy (*HbAA*) red blood cells (RBCs) in each other's plasma.

Additionally, sample aggregation was measured via aggregometry (MA1, Myrenne, Roentgen, Germany) as the percent change in light transmission through a film of blood as RBCs aggregate at stasis (M1) and under shear (M2) in a cone and plate viscometer. Differences in RBC aggregation as a result of changing suspending plasma were compared.

Given the largely negative bulk aggregation results, we suggest 3 novel techniques for measuring aggregation strength of RBCs that either correlate with fundamental aggregation energy or show aggregation dynamics in more physiological conditions. First, inspired by studies that measure aggregation energy between cells in tissues using micropipette aspiration (Guevorkian et al., 2010), we set out to form spheroidal aggregates of hundreds of RBCs without clotting components, that could be aspirated by a micropipette without breaking. We report a novel method for producing uniform aggregates using a combination of methods described in (Cines et al., 2014), (Flormann et al., 2017), and (Abkarian, Loiseau, & Massiera, 2011), in which we centrifuge RBCs suspended in PBS with 30 mg/mL of 2000 kDa dextran (Sigma-Aldrich, St. Louis, MO, USA) at 5000 x g for 10 mins in a syringe tip (34 gauge, Sigma-Aldrich, St. Louis, MO, USA) and then expelling the packed RBCs through the syringe tip at a fixed flow rate of 1 ml/min at a fixed radius of 1 centimeter from the center of a circular dish filled with the same dextran solution spinning at a fixed angular velocity of 300 rpm on a spin coater. The shear of the packed RBCs overcomes its surface tension at a controlled droplet size to form RBC aggregates forced together by centrifugation and held together by dextran during micropipette aspiration. Aggregation energy measurements could be compared between different RBC populations in dextran. The aggregation strength of these RBC spheroids was also measured using atomic force microscopy (AFM) techniques as in (Chaudhuri et al., 2009) and (Mgharbel, Delanoë-Ayari, & Rieu, 2009). The maximum force and corresponding contact area with the AFM cantilever were used to calculate surface energy of the RBC aggregate using the Young-Laplace equation.

Finally, a mask for use in soft-lithography microfluidics to measure aggregation of tens of RBCs under biomimetic flow conditions, was designed using CleWin (WieWeb software, Hengelo, The Netherlands). The device is designed to allow visualization of aggregation as RBCs deposit downstream of PDMS posts that cause an acute downstream flow angle, as in (Loiseau, Massiera, Mendez, Martinez, & Abkarian, 2015). Aggregate size, and the percentage of posts with an aggregate can be measured with image analysis software to provide a physiological measure of aggregation dynamics.

1.4 Results

Increasing shear caused higher EI (i.e., more elongated RBCs) for all samples, and all EIs were positive (the RBCs elongated in the direction of shear), indicating that no samples contained completely rigid RBCs. Figure 1.2 shows the effect of treatment on EI in SCD. Ektacytometer EI, a measure of cell aspect ratio where zero corresponds to a perfect circle, at 3Pa shear stress (physiological range) to estimate bulk shear deformability, is compared for *HbAA*, *HbSS*, and *HbSC* RBCs under various conditions. *HbAA* volunteers have the highest EI, even after 8-weeks of storage in a bag at 4°C— the longest RBCs would be stored before being transfused into SCD patients. *HbSC* patients have the lowest, and *HbSS* patients seem to increase with high variance under HU treatment (n = 49) and increase even more with less variance under TF therapy (n = 27) over untreated patients (n = 8). *HbSC* study subjects beginning experimental HU therapy have the lowest RBC EIs. The study subjects also display a time-course line of RBC EIs for each week (Subject 1 weeks 0-4, Subjects 2-4 weeks 1-4) after beginning HU, which

show no consistent effect of HU on RBC EI within the first month of treatment. In summary, fresh healthy cells were most deformable, followed by packed RBCs stored according to blood bank regulations for 8-weeks. Long-term *HbSS* transfusion patients had the most deformable SCD RBCs, followed by long-term *HbSS* HU patients, and finally *HbSC* patients starting HU. *HbSC* HU patients showed high variability and no improvement in EI over the initial 4-week time-course of HU treatment.

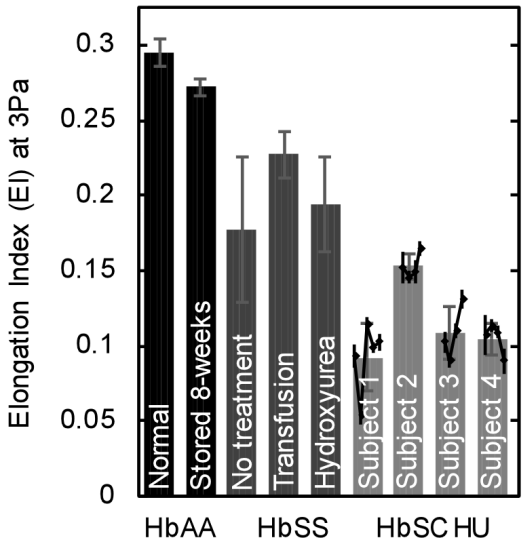

Figure 1.2: The effect of treatment on elongation index (EI) in sickle cell disease (SCD).

Additionally, HU treated *HbSS* and *HbSC* patient RBCs exhibit higher inter-sample variability than other SCD patients ($p < .05$), including *HbSS* transfusion patients. Figure 1.3 shows a histogram and t-distribution of EIs in SCD patients undergoing treatment. EIs of (n = 8) untreated *HbSS* patients, and *HbSS* patients undergoing TF (n = 27) or HU (n=49) therapy, were compared to EIs of (n = 19) *HbSC* patients beginning experimental HU therapy which did not yet show a change in EI. Despite histograms that appear potentially non-normal, Shapiro-Wilk Test p-values ($p > .05$) do not reject that EIs

are normally distributed, thus t-Test p-values confirm clear distinctions between all groups except untreated (nt) *HbSS* patients (red) and those treated with HU (purple).

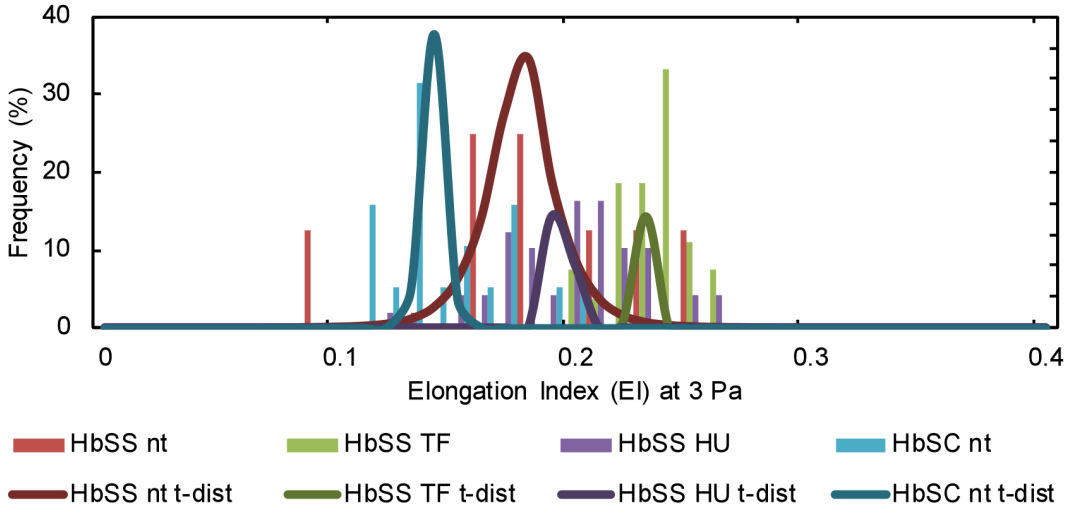

Figure 1.3: Histogram and t-distribution of elongation indexes (EIs) in sickle cell disease (SCD) patients undergoing treatment.

Given that the data are weakly normal, we display a 5-number summary (minimum, 1st quartile, median, 3rd quartile, and maximum) of EI and aggregation data for comparison between and within cohorts but use comparison statistics that assume normality. Figure 1.4 shows summarized EIs of the Houston, TX cohort of SCD patients. 5-number summary of RBC EI at 3Pa shear stress measured by ektacytometer (Rheoscan-D, RheoMeditech Inc., Seoul, Republic of Korea) is shown for untreated (n=8) *HbSS* patient RBCs, and those of patients undergoing HU therapy (n=49) and TF therapy (n=27), and for nt *HbSC* patient RBCs (n=19).

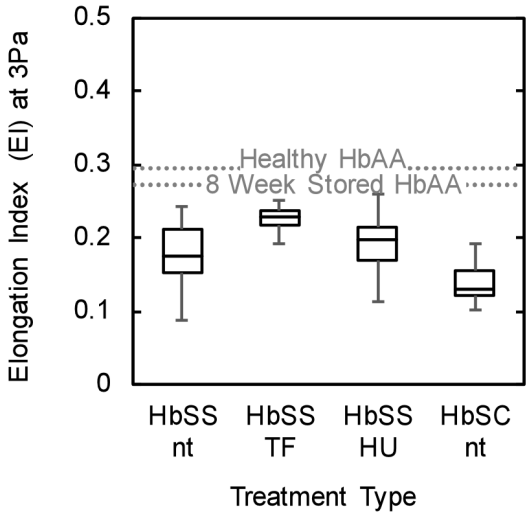

Figure 1.4: Summarized elongation indexes (EI) of Houston, TX cohort of sickle cell disease (SCD) patients.

Figure 1.5 compares the 5-number summary of Ektacytometer (LORRCA, RR Mechatronics, Zwaag, The Netherlands) EI at 3 Pa of the Lyon, France cohort of *HbAA* donor RBC samples in autologous plasma (n = 17) and in ABO/Rh-matched *HbSS* plasma (n = 12) and *HbSC* plasma (n = 12) , and *HbSS* and *HbSC* patient RBC samples in autologous plasma (n = 13 for *HbSS* and n = 12 for *HbSC*) and in ABO/Rh-matched *HbAA* donor plasma from the aforementioned ABO/Rh-matched *HbAA* donors (n = 13 for *HbSS* and n = 12 for *HbSC*). It shows no significant effects of switching plasma for either *HbAA*, *HbSS* or *HbSC* RBCs. However, it does display the difference between *HbAA*, *HbSS*, and *HbSC* EI at 3 Pa (Tukey's Test; $p < .05$), with values highly correlated with those from the Texas *HbAA* donors and SCD patients.

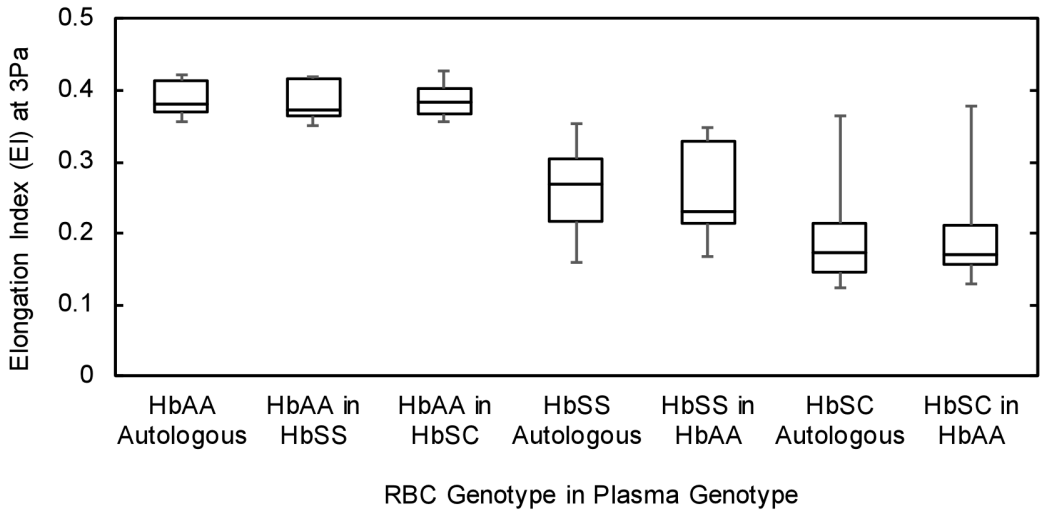

Figure 1.5: The effect of plasma on elongation index (EI; 5-number summary) in sickle cell disease (SCD).

Figure 1.6 shows the effect of plasma on high shear EI (5-number summary) in SCD. Ektacytometer (LORRCA, RR Mechatronics, Zwaag, The Netherlands) EI of the Lyon, France cohort of *HbSS* patient RBCs measured in *HbAA* (n = 13) vs. autologous plasma (n = 13), *HbSC* RBCs in *HbAA* (n = 12) vs. autologous plasma (n = 12), and *HbAA* RBCs in *HbSS* (n = 12), *HbSC* (n = 12), and autologous plasma (n = 17) at 30Pa shear stress, shows significant differences between *HbAA*, and SCD RBCs with no bearing on plasma using Tukey's Test ($p < .05$). *HbSS* plasma significantly reduced *HbAA* RBC EI weakly suggesting decreased shear deformability than when in autologous plasma ("*"; t-test; $p < .05$). Comparison with Figure 1.5 indicates that EI at 30 Pa may be better for statistically significant discrimination between *HbAA* and SCD RBC genotypes, but worse for discrimination between SCD genotypes.

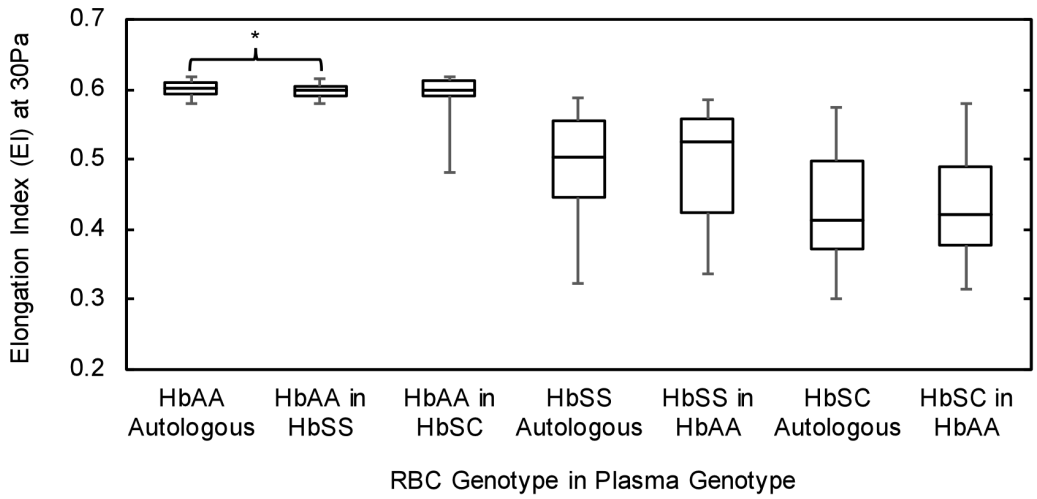

Figure 1.6: The effect of plasma on high shear elongation index (EI; 5-number summary) in sickle cell disease (SCD).

Figure 1.7a shows the representative RBC micropipette aspiration images used to measure RBC shear modulus in autologous and ABO/Rh-matched plasma from other Hb genotypes. The left column shows a healthy RBC, the central column shows an *HbSC* RBC, and the right column shows an *HbSS* RBC being aspirated into a micropipette at increasing pressure from top to bottom until the RBC finally buckles into the micropipette. Healthy and *HbSS* images were taken at 60 x, and *HbSC* images were taken at 100 x magnification (Eclipse Ti2, Nikon, Tokyo, Japan). Figure 1.7b shows the linear relationship between suction pressure and the length of membrane pulled into the pipette tip, and Figure 1.7c uses the Skalak *et al.* law to relate a function of the length of the RBC insertion into the pipette (y-axis) to a function of pressure (x-axis), where the slope of the linear fit between the points corresponds to the linear shear modulus of the RBCs pictured in Figure 1.7a. Lambda (λ) derived from Dimitrakopoulos 2012 as (2L/r-1)*(L/r+r/2L+1/2), is the unitless extension ratio between the length of shear hardening RBC membrane sucked into the micropipette (L) and the inner radius of the micropipet

tip (r), vs. shear stress tau (τ) on the RBC calculated as the suction pressure in the pipet multiplied by its inner radius. Shear moduli (G) of 1.7, 2.8, and 5.7μN/m for the healthy, *HbSC*, and *HbSS* RBCs in the figure respectively were calculated.

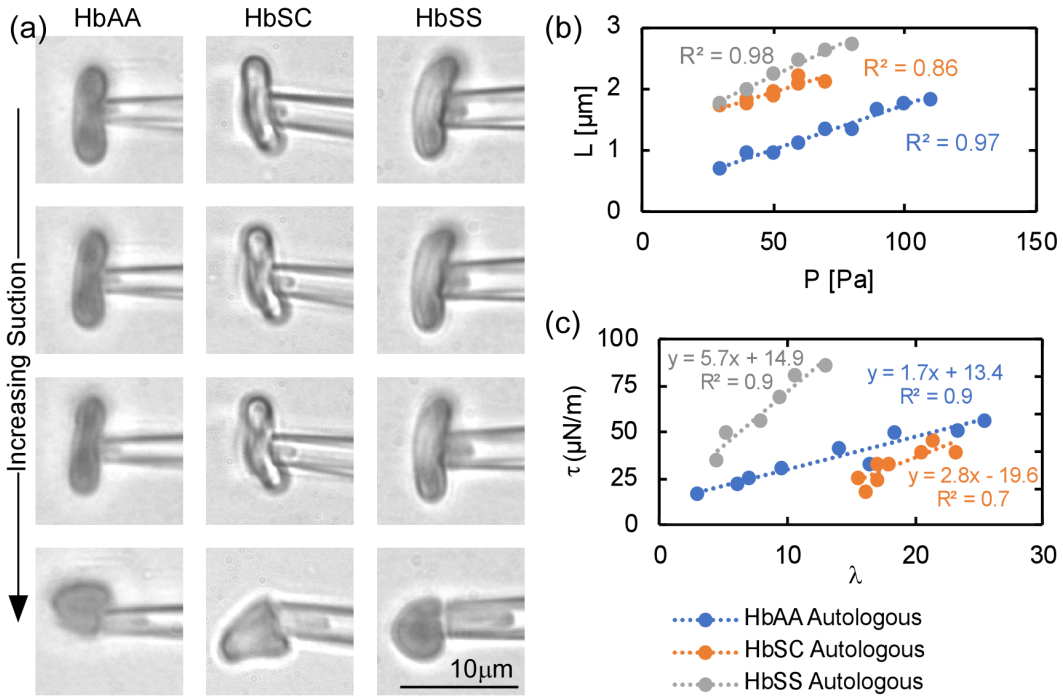

Figure 1.7: Micropipette red blood cell (RBC) shearing experiments comparing healthy, *HbSC*, and *HbSS* RBCs.

In Figure 1.8a, an RBC from one healthy volunteer (triangle marker, solid line) in autologous plasma (blue) (G = 1.7 μN/m) and plasma from an *HbSS* patient (grey) (G = 0.6 μN/m), and an RBC from another healthy volunteer (circle marker, dotted line) in autologous plasma (blue) (G = 1.7 μN/m) and plasma from an HbSC patient (orange) (G = 1.2 μN/m) suggest decrease in shear moduli of an *HbAA* RBC when suspended in SCD plasma. In Figure 1.8b, an RBC from the *HbSC* patient in Figure 1.8a in the plasma of the corresponding healthy volunteer in Figure 1.8a suggests a corresponding increase in the

shear modulus of the *HbSC* RBC when placed in the *HbAA* plasma (G = 1.8 μN/m) instead of autologous plasma (G = 1.2 μN/m).

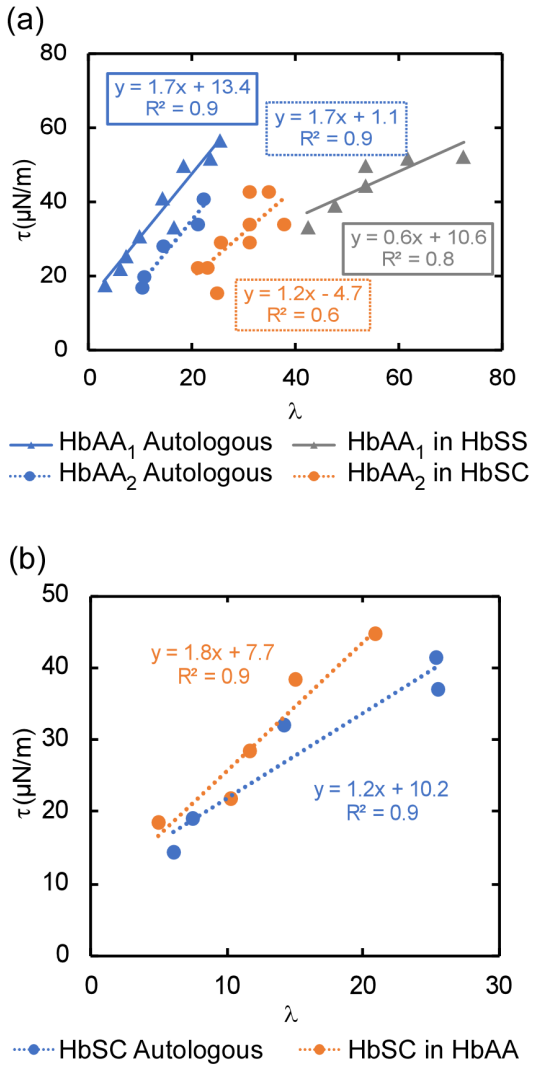

Figure 1.8: Micropipette red blood cell (RBC) shearing experiments quantifying change in shear moduli of sickle cell disease (SCD) and healthy (*HbAA*) RBCs in each other's plasma.

Bulk aggregation of the same Lyon, France cohort RBC population was also measured to test the effects of switching plasma sourced from blood with different Hb genotypes. Figure 1.9 and 1.10 show RBC aggregation measured as percentage decrease in transmittance over 10 seconds in no shear (M1) and shear (M2) for the same RBC-

plasma genotype sample pairs as in Figures 1.5 and 1.6. *HbSS* patient RBCs measured in *HbAA* (n = 13) vs. autologous plasma (n = 13), *HbSC* RBCs in *HbAA* (n = 12) vs. autologous plasma (n = 12), and *HbAA* RBCs in *HbSS* (n = 12), *HbSC* (n = 12), and autologous plasma (n = 17) were measured. Figure 1.9 show no significant differences between *HbAA*, and SCD RBCs and no bearing on plasma using Tukey's Test ($p < .05$). *HbSC* plasma significantly reduced *HbAA* RBC M1 weakly suggesting increased aggregation than when in autologous plasma ("*"; t-test; $p < .05$).

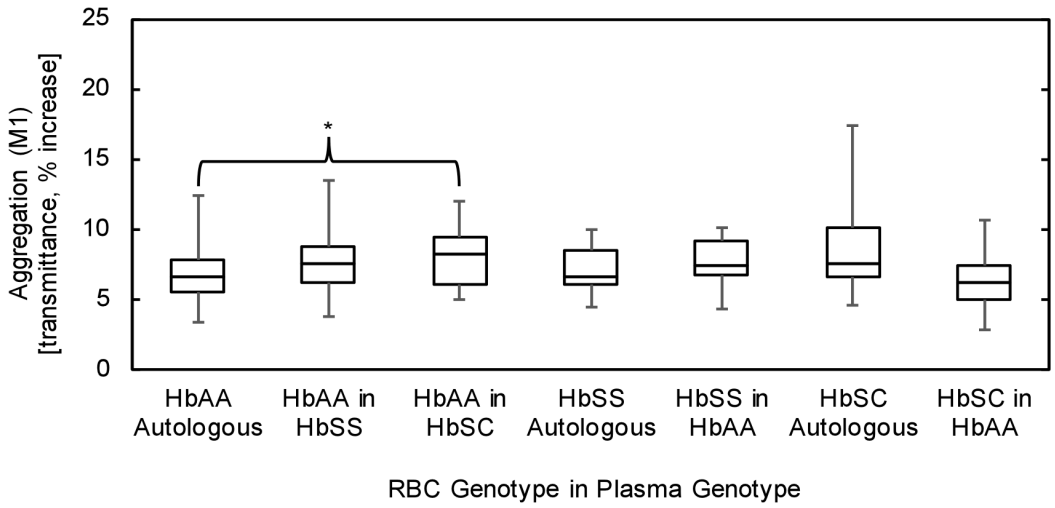

Figure 1.9: No-shear aggregation (M1; 5-number summary) of sickle cell disease (SCD) patients in each other's plasma.

Figure 1.10 shows no significant increase in M2 for any RBC-plasma Hb genotype pair tested (Tukey's Test; $p < .05$), though some correlation of M2 to M1.

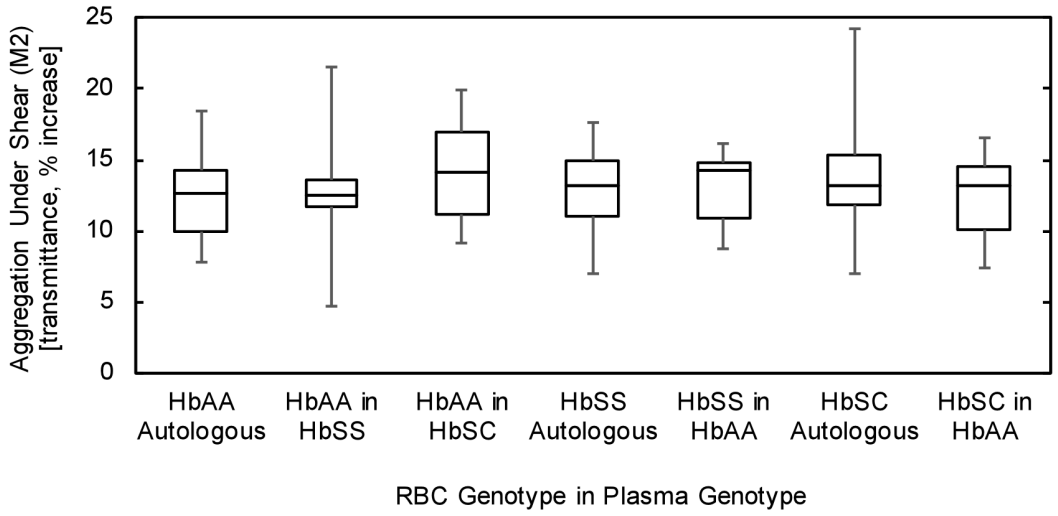

Figure 1.10: Shear aggregation (M2; 5-number summary) of sickle cell disease (SCD) patients in each other's plasma.

Figure 1.11 illustrates proof-of-concept for two new methods to measure aggregation in single spheroidal aggregates of hundreds of RBCs in dextran solution. Figure 1.11a demonstrates a method to quantify aggregation energy using a micropipette. Preliminary micropipette aspiration experiments show a relationship between the pressure in the pipette and the aspirated portion of the RBC ball with some hysteresis in the aggregation energy of these RBCs over multiple trials. Figure 1.11b demonstrates a method to quantify surface energy using an AFM with a mirror to show the side-view of the aggregate underneath the cantilever. Figure 1.11c displays the corresponding force-distance curve from which a maximum force of 8 μN can be extracted and used to calculate a plausible RBC ball surface energy of 20 $\mu J/m^2$ with the contact area with the probe and the Young-Laplace equation.

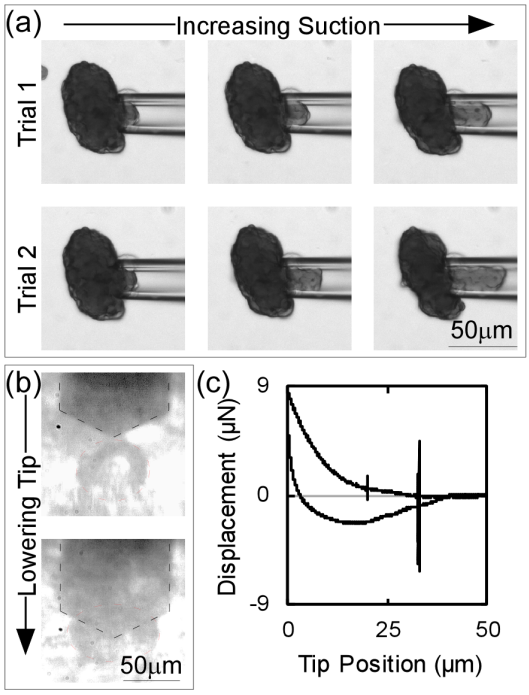

Figure 1.11: Potential methods for measuring red blood cell (RBC) aggregation energy using novel RBC aggregates.

We also designed the specifications of a photomask for use in soft-lithography to produce a microfluidic device that can quantify aggregation in biomimetic flow patterns. Figure 1.12a shows the approximate size of the mask, with the large grey square indicating the size of a typical glass slide. It allows for four grids of four devices with posts varying in curvature and flow angle in a 3-inch diameter circle. The devices contain channels that allow quasi-uniform flow around posts with different angles and curvatures varied in each of four sections. Figure 1.12b is a ~5x magnification of Figure 1.12a, showing 2 such devices. Figure 1.12c, a ~50x magnification of Figure 1.12a, shows the inlet and outlet connected to the straight channel network containing posts by a low curvature bifurcated tree that minimizes enrichment of certain RBC subpopulations to certain channel locations from laminar flow effects including dean-flow and inertial focusing. Figure 1.12d, a ~100x magnification of Figure 1.12a, shows posts of uniform

shape spaced at a minimum distance of three times their longest dimension from each other and the nearest wall to minimize heterogeneity of flow conditions at each post. The white rectangle highlights a 480 x 480 μm field of view with 30 posts visible. Designed channel depth is ~60 μm to maintain low aspect ratio for narrow walls between channels. In normal saline *HbSS* RBCs have been shown to aggregate around posts like these (Loiseau et al., 2015), so simple software can track the percent of posts with aggregates and the average aggregate size over time to quantify aggregation.

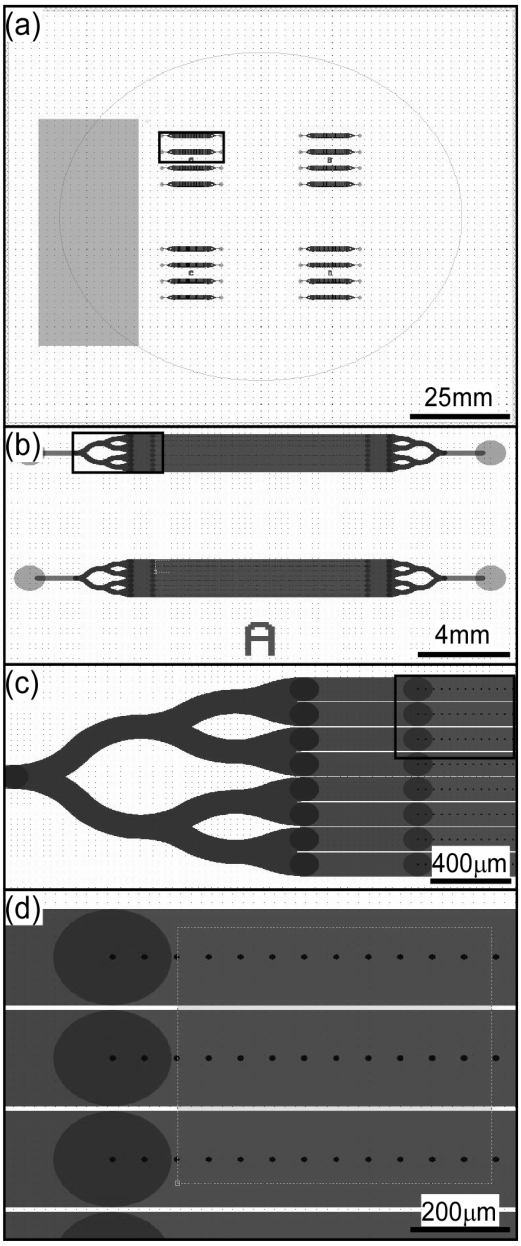

Figure 1.12: Mask design schematic of a prototypical microfluidic device for measuring physiologically relevant metrics of red blood cell (RBC) aggregation.

1.5 Discussion

Though *HbSC* patients typically exhibit better clinical outcomes than *HbSS* patients, their RBC EIs are lower than *HbSS* RBCs when oxygenated. This may be attributable to the fact that *HbSC* RBCs do not tend to adopt the *HbSS* sickle shape and

thus *HbSC* RBCs do not rotate during EI measurement while *HbSS* RBCs do. This is an example of how EI measurement is misleading as an indication of shear deformability.

Still, these data show that HU does not improve EI of *HbSC* RBCs in the first month of treatment, though longer-term data with more hematological metrics should be collected to qualify the efficacy of HU as a treatment for *HbSC*. They also show that plasma exchange does not have a consistent effect on the EI of SCD RBCs while both TF and HU therapy seem to increase EI of *HbSS* patient RBCs, though only TF does so significantly ($p < .05$). The increased variability of the EI of SCD patients on HU treatment as compared to other SCD patients and healthy subjects, may also shed light onto the idiosyncratic nature of HU to affect patients differently.

This research also shows that ektacytometry and bulk aggregometry of RBCs may not be sensitive enough to changes in RBC shear deformability and aggregation strength respectively to serve as useful diagnostic tools for the comparison of pathological RBC populations present in *HbSS* and *HbSC* SCD. Better measuring devices could improve our understanding of overall perfuse-ability as well as the compensation mechanisms (such as decreasing cell size and Hb concentration) characteristic of each genotype-treatment combination.

1.6 Conclusion

Rigid, misshapen RBCs are common in SCD and contribute to anemia and associated pathologies in the disease. SCD patients have limited treatment options that depend on the specific Hb-associated genotype causing the condition. The only drug approved for any form of SCD, HU, has only been validated in patients with the

homozygous *HbSS* genotype, the most common form of the disease. Even in *HbSS*, efficacy of HU is patient-dependent and not fully understood. In an attempt to better understand the effects of HU, we measure the EI of RBCs in patients with *HbSS* and compare it to that of untreated *HbSS* carriers and those who receive chronic transfusions of healthy RBCs. We then evaluate HU as a potentially novel treatment for patients with the second most common form of SCD, *HbSC*, who have inherited the gene for HbS heterozygously with the gene for another harmful form of hemoglobin, HbC, by measuring EI weekly through their first month of treatment. Through comparison of the *HbSC* HU-treated cohort, with the *HbSS* HU-treated cohort, we evaluate whether HU similarly affects RBC EI in both forms of the disease. We find that although EI captures a difference between the *HbSS* and *HbSC* RBCs treated with HU, namely that HU does not seem to increase EI of *HbSC* patients in the first month of treatment the way it may for *HbSS* patients after long-term treatment, the measurement does not seem to agree with preliminary shear deformability results from micropipette experiments. We theorize that this may be due to the convolved effects of the behavior of the most morphologically abnormal populations of RBCs to rotate instead of elongate during EI measurement. In the next chapter, we further try to understand how this rotation effect influences EI measurements, and what EI measurements can indicate about the behavior of pathological populations of RBCs *in vivo*.

CHAPTER 2 EKTACYTOMETRY VERSUS AN ARTIFICIAL MICROVASCULAR NETWORK TO MEASURE RBC PERFUSION: Comparing deformability and perfusion of human and non-human RBCs

2.1 Introduction

The morphology and deformability of red blood cells (RBCs) are critical to the ability of blood to efficiently transport oxygen and metabolites between tissues, however some animal species have developed RBCs with shapes and deformabilities that would cause serious hemorheological pathologies in humans. Human, goat, llama and rooster RBC deformabilities were compared by measuring their shear elongation index (EI) in a conventional ektacytometer at fluid shear stresses ranging from 0.3-30 Pa and their flow direction and perfusion rate (PR) through an artificial microvascular network (AMVN) at 10 cmH_2O driving pressure, both at sample-specific physiological hematocrits (HCTs) and at equalized average human physiological HCT. Human RBCs had the greatest 30 Pa-shear-stress EI and equalized-HCT PR, followed by goat (EI: 54% of human, PR: 95% of human), rooster (EI: 4.4%, PR 66%) and llama (EI: -16% i.e., misaligned, PR: 59%) RBCs. At sample-specific physiological HCT, human PR was still highest, followed by llama (PR: 83% of human), goat (80%) and rooster (47%). Bulk shear deformability measured by the ektacytometer at greater than physiological shear stresses was weakly correlated with AMVN PR. Rotation and misalignment of rigid or non-spheroidal RBCs provided elongation results that are misleading with respect to RBC perfusion ability, oxygen delivery capacity and vaso-occlusion risk. The AMVN provided a measure of morphology and deformability based on combined rheological effects that is

more predictive of the severity of hemorheological pathologies caused by abnormal RBCs.

2.2 Background

The ability of blood to perfuse microvascular networks is critical for the delivery of oxygen and other nutrients as well as for the removal of waste products from metabolizing tissues and vital end organs (Burrin, Ferrell, Eisemann, Britton, & Nienaber, 1989; Lassen, 1959). Shape, size, concentration and deformability of RBCs are some of the most influential factors in maintaining healthy blood perfusion through the microvasculature (Aarts, Heethaar, & Sixma, 1984; Chien, 1987; Skalak & Branemark, 1969). The interspecies variation in these factors is far greater than that observed intraspecies, even among the most pathological RBC populations within a species (Diez-Silva, Dao, Han, Lim, & Suresh, 2010; Weiss & Wardrop, 2011). For example, volume and concentration of RBCs range from 80-96 fL and 4.2-6.1x10^6 RBCs/μL for healthy humans, and the range expands to 60-140 fL for patients with severe forms of micro- and macrocytic anemias and 3.1-7.1x10^6 RBCs/μL for those with severely cytopoenic and polycythemic anemias, which are narrower still than the ranges 25-126 fL and 2.1-12.1x10^6 RBCs/μL spanned by the species in this study (Sarma, 1990, Veda, 2013 #110; Wasserman & Gilbert, 1963).

The shape, size, concentration or deformability of capra aegagrus (goat), lama glama (llama), or gallus gallus domesticus (rooster) RBCs would likely result in severe rheological dysfunction if adopted by human RBCs. However, these animals have different microvascular architectures and metabolic needs which allow RBCs with

different physical parameters to maintain appropriate perfusion to continually sustain surrounding tissues (O. K. Baskurt, Hardeman, & Rampling, 2007). The flow of these aberrant RBCs can be studied to understand the complex interactions between many RBC characteristics that are of great interest to developing therapies for human blood and vascular disorders (Antonelou et al., 2011, Lamarre, 2012 #32; Ballas, Dover, & Charache, 1989). Some *in vitro* rheological assays attempt to understand bulk *in vivo* RBC perfusion by quantifying one specific mechanical blood property (e.g., ektacytometry, aggregometry, viscometry) but do not evaluate the interactions between multiple properties. Utilization of an AMVN – a physiologically inspired microfluidic model of mammalian microvasculature which more closely simulates the wide range of environments and stresses experienced by RBCs in complex microvascular networks – enables evaluation of the combined impact of multiple properties on RBC perfusion (Burns, Yang, Forouzan, Sosa, & Shevkoplyas, 2012). To better understand how physical RBC parameters combine to maintain blood perfusion we studied human, goat, llama and rooster RBCs in parallel and compared mean RBC volume (MCV), RBC count, ektacytometer EI and AMVN PR. To better qualify clinical EI measurements in the context of pathological human RBC populations, we focused on how conventionally measured EIs are not good predictors of PRs for RBCs with abnormal characteristics.

RBC morphology is one characteristic that serves as a critical component of normal vascular functioning in humans (Suresh, 2006). A number of biophysical conditions maintain the delicate osmotic balance and molecular interactions required to optimize human RBC morphology for perfusion through the microvasculature (Chien, 1987; Shiga, Maeda, & Kon, 1990; Weed, LaCelle, & Merrill, 1969; P. Wong, 2006).

Human RBCs have a unique biconcave discocytic shape with an average MCV of 90 fL which optimizes surface area to volume ratio to allow for large bending deformations as they flow through capillaries down to a quarter of the diameter of a discocyte (Canham, 1970; Fischer, Haest, Stöhr-Liesen, Schmid-Schönbein, & Skalak, 1981). For comparison, Figure 2.1 shows bright-field microscopy and laser diffraction pattern images of goat, rooster, and llama RBCs. Microscope (IX73, Olympus, Tokyo, Japan) images taken through a 420 ± 2 nm wavelength bandpass filter at 40 x magnification show small, asymmetrical goat RBCs, large rooster RBCs, and prolate ellipsoidal llama RBCs suspended in normal saline. Diffraction patterns taken via provided ektacytometer software (LORRCA, RR Mechatronics, Zwaag, The Netherlands) at 30 Pa shear flow show noisy, rotating and misaligning goat, rooster, and llama RBCs respectively. The red arrow indicates the direction of shear. Goat RBCs are classified as poikilocytes, or morphologically aberrant discocytes, and are approximately one-quarter of the volume of human RBCs, with an average normal MCV of 20 fL (Fig. 2.1a). The aberrant membrane protrusions and small size of goat RBCs are in some ways an exaggerated version of the pathology observed in human patients with sickle cell anemia (Jain, Kono, Myers, & Bottomly, 1980). Llama RBCs are prolate ellipsoids with an MCV of 26 fL (Fig. 2.1b). The much lower surface to volume ratio of RBCs with such spheroidal morphology could suggest higher rigidity, such that, along with their compact size, llama RBCs could reveal what might happen in human patients with hemoglobin SC disease, a form of sickle cell disease common in some West African, Caribbean, and American subpopulations (Ronald L Nagel, Mary E Fabry, & Martin H Steinberg, 2003; Torabian, Lezzar, Piety, George, & Shevkoplyas, 2017). Rooster RBCs are significantly different from those of

mammalian species, as mammals are the only animals with denucleated RBCs. Nucleated rooster RBCs have an MCV of 115 fL (Fig. 2.1c). The large size, high rigidity and more prolate morphology from containing nuclear and non-mammalian cytoskeletal components, can in some ways predict how RBC perfusion may be altered in humans with hereditary spherocytosis (O. K. Baskurt et al., 2007; Salomao et al., 2006; Weiss & Wardrop, 2011).

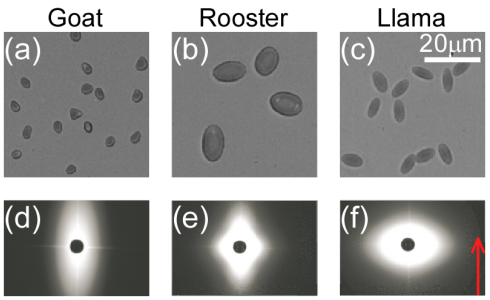

Figure 2.1: Bright-field microscopy and laser diffraction pattern images of goat, rooster, and llama red blood cells (RBCs).

RBC size is inversely correlated with RBC count across these species, such that mean cell hemoglobin concentration (MCHC), HCT – the volume fraction of whole blood that is occupied by RBCs – and, as a result, the volumetric amount of oxygen available in the blood of different animals are held within relatively narrow ranges despite differences in other RBC properties. The ranges of MCHC and HCT across species may be more tightly constrained than the ranges of other RBC attributes because increasing MCHC leads to higher cytoplasmic viscosity and hemoglobin insolubility causing RBCs to become too rigid, and increasing HCT exponentially increases blood viscosity particularly in smaller vessels above certain HCT thresholds due to the attenuation of the Fahraeus-Lindqvist effect (O. K. Baskurt et al., 2007; Itano, 1953;

Whittaker & Winton, 1933). As such, we observed RBC flow in the AMVN at physiological HCT for each species (measured at the time of donation) to understand how these RBCs might function differently to deliver oxygen *in vivo*, and at average human HCT of 40% to provide a more controlled condition for comparison. Using bulk EI and PR of RBCs from different species at the same HCT, we then compared how these measures of RBC deformability under flow were influenced by RBC morphology to understand how EI might function to predict PR.

The flow conditions in the ektacytometer and AMVN differ greatly. Due to the much higher number of flow conditions present in the AMVN, we hypothesized that EI may at best quantify RBC behavior in a small percentage of the AMVN and play a minimal role in prediction of PR. Though the AMVN more closely mimics physiological flow patterns, EI provides a measurement that in ideal cases can more directly be compared to the physical quantity of RBC membrane shear modulus. The viscosity of blood plasma, which is primarily composed of water, causes the formation of a shear stress field within blood vessels, and the variation of shear rate along the cross-section of microvasculature induces shear deformation in RBCs, particularly near the vessel boundaries where variation in shear rate is highest (David Bruce Dill & David L Costill, 1974).(D. B. Dill & D. L. Costill, 1974) For a fluid undergoing laminar flow in a physiological cylindrical vessel, or a rectangular microfluidic channel as in the AMVN, the shear field can be modeled as roughly parabolic and radially symmetric over the channel cross section given realistic boundary conditions. According to Poiseuille's law, the shear stress in a cylindrical vessel is given by

$$\tau = \frac{4Q\mu}{\pi r^3}, \tag{2.1}$$

where shear stress, τ, is directly proportional to Q, the volumetric flow rate of the fluid, and μ, the dynamic viscosity of the fluid, and inversely proportional to the cube of r, the radial position in the vessel (Bruus, 2014). Secondary effects on the shear rate in complex, non-Newtonian fluids like blood, such as the Fåhræus-Lindqvist effect, are not included in the estimations of shear stress experienced by RBCs in the microchannels. Thus Poiseuille's law provides an upper bound on the fluid shear stress imposed on RBCs in microvasculature (Fahraeus & Lindqvist, 1931). In addition to stress caused by the fluid medium, cell-cell and cell-wall interactions also play a role in determining overall flow rate. As larger cells may experience fewer collisions but less transverse motion through complicated networks (Gifford et al., 2018), we analyzed flow patterns of individual RBCs in the AMVN to see if variations caused by these interactions as a result of RBC size may be reduced in the AMVN by equalizing HCT between samples.

Unlike the AMVN, conventional ektacytometry induces shear stress on RBCs by shearing blood in a viscous buffer between two plates, either through a high aspect ratio rectangular channel, or between two rotating concentric cylinders (also known as a LORRCA or laser-assisted rotational cell analyzer). The deformability measurements of cell populations are in agreement between the two designs (S. Shin, J. Hou, J. Suh, & M. Singh, 2007).(S. Shin, J. X. Hou, J. S. Suh, & M. Singh, 2007) The latter was used in this study to produce Couette flow with a linear shear field given by

$$\tau = \frac{\mu\omega r}{d}, \tag{2.2}$$

where τ is the fluid shear stress, μ is the dynamic viscosity of the fluid, ω is the angular velocity of the inner cylinder relative to the outer cylinder, r is the radius of the inner cylinder and d is the length of the gap between cylinders. The linear shear profile produced in Couette flow and the parabolic shear profiles produced by Poisseuille flow in microvessels are similar relative to the sheared RBC when the diameter of the channel or gap is much larger than the RBC, such that the parabolic shear profile can be discretized into linear components spanning the RBC. Thus ektacytometry may model shear deformation of RBCs in the large channels of the AMVN well, if not for frequent collisions, but will not predict shear and bending deformation found in the smaller, capillary-sized channels of the AMVN.

The conventional high viscosity conditions in ektacytometers have been shown to be unsuitable for calculating a rational EI at high fluid shear for some rigid or highly non-spherical human and non-human RBC populations, as some RBCs may rotate or misalign instead of elongating (Smith, Mohandas, & Shohet, 1979). RBC rotation causes under-estimation of EI as RBCs aligned non-parallel to the shear strain superimpose diffracted light that causes overestimation of the width of the diffraction pattern generated by elongated RBCs. Misalignment can cause calculation of a negative EI uncorrelated with shear since the longer axis of the RBC is misaligned with the shear field and interpreted as the width by ektacytometer EI ellipse fitting software. In a previous study, rotation may have been responsible for underestimation of the magnitude of changes in PR with respect to EI, though in some cases EI underestimation may correlate better with PR results since PR has also previously been shown to be more sensitive than EI to certain changes in RBC deformability that do not cause rotation in the ektacytometer (Sosa,

Nielsen, Vignes, Chen, & Shevkoplyas, 2014; Vörös, Piety, Strachan, Lu, & Shevkoplyas, 2018).

Understanding the complex relationship between EI and PR for RBCs with abnormal morphology and deformability can qualify the use of EI as a clinical marker for pathological RBC populations. To this end, we applied an anomalous diffraction model assuming optically-soft (somewhat transparent) ellipsoids, to the diffraction pattern images produced by the ektacytometer to better understand the varying sources and degrees of misestimating RBC morphology when calculating EI.

2.3 Materials and Methods

The study protocol was approved by the University of Houston institutional review boards. Venous whole blood samples were obtained with written informed consent in 4 mL Vacutainer tubes (K2EDTA, BD, Franklin Lakes, NJ, USA) from healthy, normal human volunteers. Blood samples were stored at room temperature and used within 8 hours following collection. Blood samples from goat, rooster and llama in K2EDTA were obtained from Lampire, Inc., Pipersville, USA.

Two sets of samples were run through the AMVN, one set at the sample-specific physiological HCT obtained at time of donation, and the other with HCTs equalized to an average human physiological HCT of 40%. To prepare equalized-HCT blood samples for the AMVN, whole blood samples were diluted 1:50,000 in phosphate buffered saline (PBS) (pH 7.4). The cell count and mean cell volume (MCV) of RBCs from each species were then calculated using a coulter counter (Beckman Coulter, Indianapolis, IN), setting

appropriate size thresholds to exclude other cell types. RBC count was multiplied by MCV and scaled (divided by 10) to calculate HCT in the original whole blood. Original blood samples were then leukoreduced by centrifuging at 1600×g for 10 minutes and removing the buffy coat and supernatant plasma with a pipet, accounting for the volume removed to control HCT. Pelleted RBCs were then resuspended at 40% HCT in GASP buffer (9 mmol/L Na_2HPO_4, 1.3 mmol/L NaH_2PO_4, 140 mmol/L NaCl, 5.5 mmol/L glucose, 1% (weight/volume) bovine serum albumin (BSA), 290 mmol/kg, pH 7.4) for equalized-HCT samples and resuspended at their original HCT in GASP for sample-specific physiological HCT samples. GASP was used as suspending medium to minimize the effects of plasma viscosity and RBC aggregation from plasma proteins on flow through the AMVN.

The AMVN devices were created using soft lithography as previously described in detail (Burns et al., 2012; Sia & Whitesides, 2003; Whitesides, Ostuni, Takayama, Jiang, & Ingber, 2001). To enable flow of the non-human RBCs used in this study, the previous protocol was altered to produce channels that were twice as deep, and the driving pressure across the AMVN was halved during measurement to compensate. Briefly, the patterned silicone wafer was prepared by spin-coating (PWM32-PS-R790, Headway Reseach Inc., Garland, TX) a 10μm layer of SU8-negative photoresist onto the silicone wafer (University Wafer, South Boston, MA), and otherwise following the procedure detailed previously. The wafer was used to replica-mold all polydimethyl-siloxane (PDMS) (Sylgard 184, Dow Corning Corp., Midland, MI) AMVN devices used in the study. Before making the AMVN measurement, we filled assembled devices with a

1% (w/v) solution of mPEG-silane (Laysan Bio Inc., Arab, AL) in GASP and incubated for at least 8 hours at 4°C to prevent RBCs from adhering to the PDMS channel walls.

The measurement was carried out as previously described in detail (Burns et al., 2012; Piety, Reinhart, Pourreau, Abidi, & Shevkoplyas, 2016; Piety, Reinhart, Stutz, & Shevkoplyas, 2017). Briefly, the device was fixed to the stage of an inverted brightfield microscope (IX73, Olympus America Inc., Center Valley, PA). GASP solution containing mPEG-silane was removed from the inlets and flushed from the network for 10 minutes with GASP driven at 10 cmH_2O vacuum pressure produced by controlling the height of a water column connected to the outlet. GASP was then removed from the inlets before loading them with RBC samples. Samples were allowed to flow for 3 minutes to flush remaining GASP and fill the device with RBCs. The subsequent recording period consisted of a 1-minute interval at 0 cmH_2O driving pressure to measure a baseline flow rate from each inlet before the water column was lowered 10 cm and samples were allowed to flow at 10 cmH_2O driving pressure for 3 minutes. Bursts of 10 images of the most downstream channel were taken at 150 fps every 10 seconds throughout the recording period and analyzed with a custom MATLAB (Mathworks, Natick, MA) script to calculate flow rate over time.

Short videos (256 frames at 15 fps) of RBCs at sample-specific HCT moving through a complex part of the AMVN capillary network were also recorded for each species and analyzed with a custom MATLAB script which used the built-in Farneback optical flow tracking algorithm with 3 pyramid levels and a 17-pixel neighborhood to track movement of individual RBCs as they traversed the network. A transverse ratio was then calculated as the magnitude-scaled horizontal movement through the network

divided by the total movement, to understand if variations in PR caused by differences in cell-cell or cell-wall interactions resulting from differences in MCV may be reduced in the AMVN by equalizing HCT between samples, as larger RBCs may experience fewer collisions but less transverse motion through complicated networks.

For ektacytometry, original whole blood samples were suspended at 0.5% (v/v) in a proprietary buffered polyvinylpyrrolidone (PVP) solution to measure cell deformability in a conventional Lorrca Maxsis Osmoscan ektacytometer (R&R Mechatronics, Hoorn, The Netherlands) using standard procedure (Hardeman, Goedhart, Dobbe, & Lettinga, 1994). Briefly, 900 µL of each sample in PVP was pipetted into the 300 µm gap between a thermostatic (37°C) glass bob and cup. The "Deformability Test" software function of the Lorrca was then used to rotate the cup and produce fluid shear stress ranging from 0.3-30 Pa, calculated by using Newton's Law of Viscosity with a known PVP medium viscosity (~31 mPa•s) and a motor-controlled shear rate as the cup is rotated around the bob to produce Couette flow in the gap. A diffraction pattern was produced by passing a 670 nm wavelength, 4 mW diode laser in the bob through the thin layer of RBCs in the gap to a screen monitored by a CCD-camera connected to a computer. The screen masks the center of the pattern from the camera to prevent saturation from the central laser beam. Built-in software fits an ellipse to the diffraction pattern at various fluid shear stresses to calculate an elongation index (EI).

Principal component analysis (PCA) was performed using MatLab (MathWorks, Natick, MA, USA) to generate biplots displaying the linear contribution of each measured RBC attribute to variation between samples from each species. The attributes were solved as variable coefficients that maximize distance between each animal species'

RBC's observation score. Similarity between samples was plotted with respect to all variables, and separately with respect only to deformability measurement variables (EIs and PR). Squared Pearson Correlation Coefficient (r^2) between PR and EI for all animal species was calculated at each EI shear stress as well.

To determine how the ektacytometry diffraction patterns, used to calculate EIs by fitting an ellipse to the pattern, related to the maximally elongated shape of RBCs in the ektacytometer gap, an anomalous diffraction model for elliptical scattering objects,

$$I_A = I_0 \left(\frac{1}{k^2 r^2}\right) |S(v)|^2, \tag{2.3}$$

with,

$$S(v) = \alpha^2 \int_0^{\pi/2} [1 - \exp(-i\phi_{max} \sin\tau)] \times J_0(\alpha v \cos\tau) \sin\tau \cos\tau \, d, \tag{2.4}$$

where $r = (x^2 + y^2 + z^2)^{1/2}$, the equation of a sphere, and $v = \frac{1}{r}[(x^2/q) + (qy^2)]^{1/2}$, the equation of an ellipsoid with ellipticity $q = a/b$, where x, y and z describe a Cartesian coordinate system with origin at the center of the diffracting object, y-axis parallel with the direction of shear and the diffraction screen, x-axis perpendicular to the direction of the shear and parallel to the diffraction screen, and z-axis perpendicular to the direction of shear and the diffraction screen (aligned with the laser path), and where a, b, and c are the dimensions of the scattering ellipsoid aligned with the y, x, and z-axes respectively, was applied to the diffraction patterns produced by the ektacytometer at 30 Pa of fluid shear stress. Eq. (2.3) has been previously derived in detail and used to model ektacytometry diffraction patterns to find the average dimensions of shear deformed human RBCs (G. J. Streekstra, Hoekstra, Nijhof, & Heethaar, 1993). A custom MatLab

(MathWorks, Natick, MA, USA) script was written to extract necessary parameters from the diffraction images produced in this study and solve Eq. (2.3) to produce a 3-dimensional model of the average elliptical RBC from the stack of diffraction images. The size parameter

$$\alpha = kA = \left(\frac{2\pi n_{med}}{\lambda_0}\right) A, \tag{2.5}$$

where n_{med} is the refractive index of the suspending medium (1.345 for the PVP solution used in this study), λ_0 is the wavelength of the diffracted ektacytometer laser beam (670nm), and $A = \sqrt{ab}$ is the square root of the cross sectional area of the diffracting ellipsoid parallel to the plane of the diffraction screen over π. The parameter

$$\phi_{max} = 2kc|m - 1|, \tag{2.6}$$

where $m = n_{int}/n_{med}$, the ratio of the internal refractive index of the diffracting object ($n_{int} = 1.335 + 0.001823Hb + 8.6526 \times 10^{-6}Hb^2$) found experimentally to fit the second order polynomial function of hemoglobin concentration of the diffracting object Hb to the refractive index of the suspending medium (G. J. Streekstra et al., 1993). In this study average MCHC of each species (human = 34 g/dL; goat = 33 g/dL; llama = 44 g/dL; rooster = 31 g/dL) was used (Weiss & Wardrop, 2011). $J_0(u)$ denotes the zeroth-order Bessel function, numerically integrated in MatLab (MathWorks, Natick, MA, USA) using built-in global adaptive quadrature with default absolute error tolerance of 1×10^{-10} and relative error tolerance of 1×10^{-6}. The diffraction intensity amplitude function $S(v)$ for anomalous diffraction of an ellipsoidal particle is found in terms of variable τ similar

to the derivation of van de Hulst for spheres as in (G. J. Streekstra et al., 1993). I_0 is the intensity of the laser beam (estimated at 400 W/m^2).

I_A, the intensity of the scattered light of the diffraction pattern, is then generated for different values of α, until the model scattered intensity closely matches that of the experimental diffraction pattern intensity. The match of the model to the experimental results was evaluated by scaling both intensity patterns to have intensities ranging from 0 to 1 and manually guessing different values of α to attempt to minimize the L^2-norm (Euclidean distance) between the radial intensity plots, with particular attention to intensities at radial angles between 2° and the angle of the first local minimum of the model intensity, since that is where the elliptical anomalous diffraction model was found to most accurately predict experimental diffraction pattern results (G. J. Streekstra et al., 1993). For visualization of the fit, the relative difference was also calculated between each point in the model and experimental intensities, as the absolute value of the experimental intensity minus the model intensity, all divided by the experimental intensity. The radial intensity was calculated as the average pixel intensity at the circular ring formed at each angle in degrees between the center of the scattering object, or RBC, and the diffraction pattern projection screen. The value of α that produced the best match was used along with the ellipticity, q, of the experimental diffraction pattern to calculate dimensions a and b of the average scattering ellipse. The ellipticity was calculated from the experimental diffraction patterns by using the Lorrca ellipse fitting software generated values for length and width as a and b respectively, such that the dimensions used to calculate EI corresponded to those of the 3D model. Finally, the depth dimension, c, of the average scattering ellipsoid was found using

$$c = 3\pi V \left(\frac{n_{med}}{\lambda_0 \alpha}\right)^2, \tag{2.7}$$

where V is the average volume of the RBCs in the scattering path estimated as the literature average MCV (human = 90 fL; goat = 20 fL; llama = 26 fL; rooster = 120 fL) for each species (Weiss & Wardrop, 2011).

The model allowed qualification of EI in two ways. First, we evaluated the correctness of assuming the diffracting objects were elliptical and aligned as the Euclidean distance between model and experimental radial intensity plots. Next, we evaluated the amount of error contributed by sources other than assuming elliptical shape by inspecting the 3D RBC models implied by the calculated a, b and c dimensions of the elliptical model and comparing how realistic these 3D ellipsoid dimensions appeared in the context of the expected error produced by ellipse fitting.

2.4 Results

Ektacytometry EI measurements for RBCs from each species, taken at 9 logarithmically equidistant points between 0.3 and 30Pa of fluid shear stress, showed difficult to interpret results indicating rotation and misalignment (Fig. 2.2). Human RBCs show the previously found logarithmic relationship between fluid shear stress and EI, with EI at 30 Pa, the maximum fluid shear stress used in this study of 0.59 ± 0.02 (n = 5, mean ± standard deviation). Goat RBCs also display a logarithmic relationship, but with considerably lower 30 Pa EI (54% of human) than human RBCs at 0.32 ± 0.01, followed by rooster RBCs (4.4% of human) at 0.03 ± 0.05, and finally llama RBCs, which show a negative 30 Pa EI of -0.10 ± 0.02. Rooster RBC EI shows a nearly linear decrease with

respect to shear for fluid shear stress greater than 1.69 Pa, whereas llama RBC EI shows nearly exponential decay becoming negative at fluid shear stresses of 3 Pa and higher.

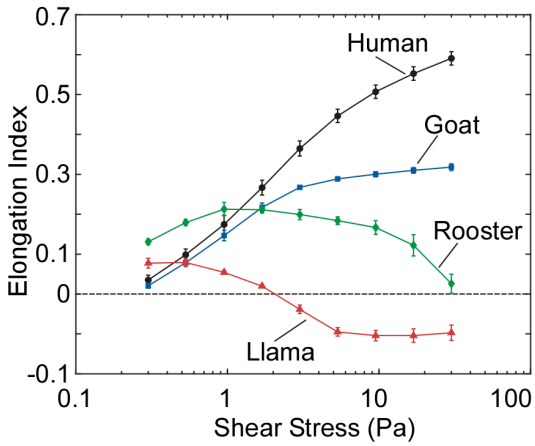

Figure 2.2: Lin-log plot of the elongation index (EI) of red blood cells (RBCs) of each species from 0.3-30 Pa shear stress.

Figure 2.3a shows the binary inverse of the photomask pattern used to produce the patterned AMVN wafer. The device mask schematic shows three identical capillary networks connecting three separate inlets to a common outlet. A microscopy image of the microvascular network shows microchannel widths ranging from 70 μm 'arterioles' down to 5 μm 'capillaries'; the depth of all channels was 10 μm throughout (Fig. 2.3b). Selected dimensions ranging from features with aspect ratios of 0.15 to 2.00, shown in the figure, were confirmed with a micrometer to remain consistent throughout different channels and devices. The green box indicates a large channel where shear flow in the channel (green arrows indicate approximate radial flow velocity) would resemble ektacytometer Couette flow on the scale of RBC dimensions, and the red box encloses a capillary with retro-flow (left), a misaligned bifurcation (center), and a capillary with forward-flow (right). Microscopy images of RBCs suspended at physiological HCT

flowing through the areas indicated by green and red boxes in Figure 2.3b show many colliding RBCs, and smaller RBCs fitting into capillary-sized channels with less bending deformation (Fig. 2.3c). The red arrows indicate the direction of constant negative pressure difference in the channel applied between the inlets and the outlet.

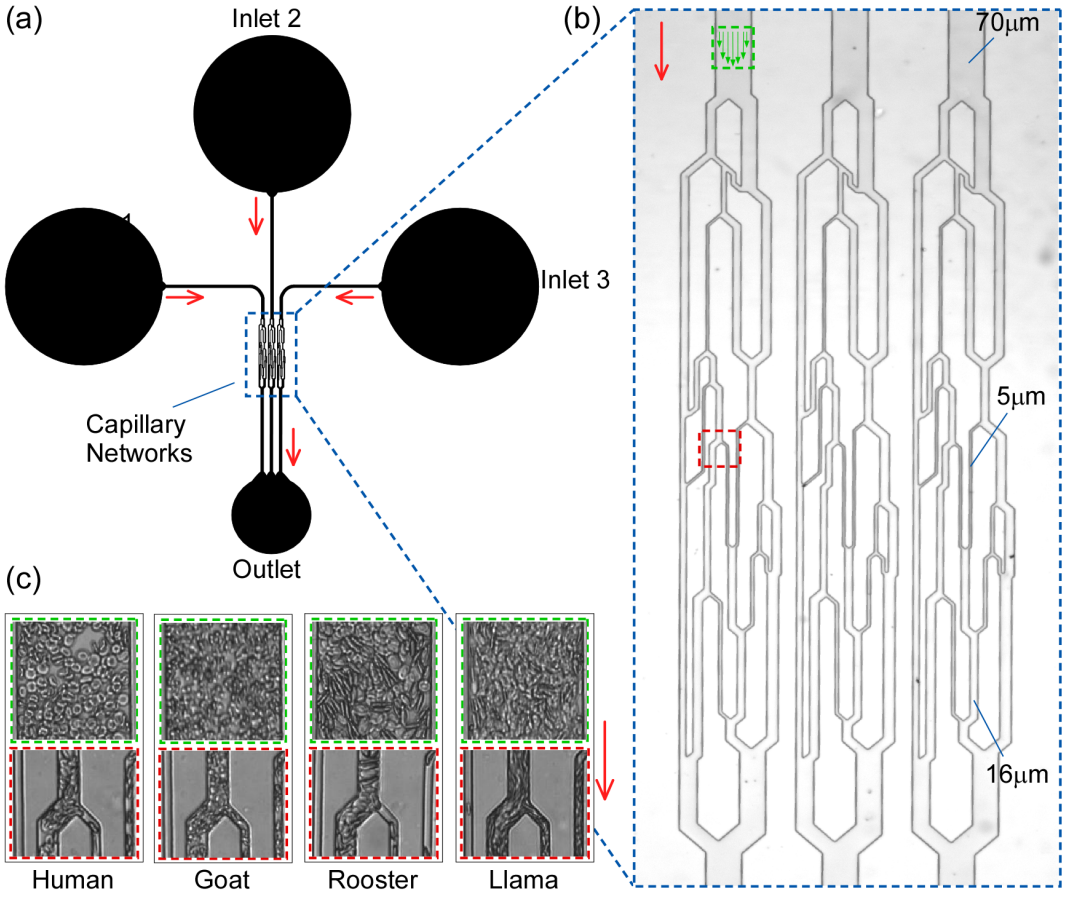

Figure 2.3: Overview of the artificial microvascular network device (AMVN) with areas of distinct flow dynamics.

Hematological parameters of the blood used to alter HCT of one set of samples prior to measurement in the AMVN, such that they were equal for all species, are reported in Table 2.1. Coulter counter (HIAC PODS+, Beckman Coulter, Indianapolis, IN, USA) mean corpuscular volume (MCV) and cell count data used to adjust HCT

between each species to prepare for AMVN measurement are shown. MCV and cell count are reported with coefficient of variation (CV) since their averages vary greatly between species, and HCT is calculated as MCV x cell count adjusted by a factor of 10 to give the percent volume of RBCs per volume of whole blood and reported with standard deviation (SD). Nucleated rooster RBCs were largest with an MCV of 126 fL ± 4.12% (n = 3) and had the lowest RBC count of 2.17×10^6/L ± 0.80 (n = 3). Rooster, llama and goat physiological samples had MCVs 140%, 31% and 27% and RBC counts of 51%, 250% and 290% of that of the human physiological samples (MCV = 90.9 fL ± 3.09%, RBC count = 4.23×10^6/L ± 2.63%; n = 3) respectively. There was a tradeoff between MCV and RBC count, which maintained physiological HCTs within a smaller range (16% CV across physiological samples from all species) than MCVs (73%) or RBC counts (66%). Before adjusting HCT, physiological sample HCTs had a standard deviation (SD) of 4.9 across samples, but the attempt to equalize HCT greatly reduced the SD across sample HCTs to 1.0. Notably, the MCVs of samples after adjusting HCT also varied less than those in the physiological samples before adjusting HCT ($p<.005$; paired t-test on MCV CVs), possibly because centrifuging burst the most fragile, volumetrically aberrant RBCs. This effect was least dramatic in llama RBCs, possibly because they are more rigid. The effect was likely not due to resuspending adjusted sample RBCs in isotonic GASP buffer, since all physiological and adjusted samples had to also be diluted in another isotonic solution before running them through the coulter counter.

Table 2.1: Human, goat, llama and rooster Coulter counter data for equalizing hematocrit (HCT)

Blood Type	Cell Count ± CV ($\times 10^{12}$/L)	MCV ± CV (fL)	HCT ± SD (%)
Human (physiological)	4.23 ± 0.11	90.9 ± 2.81	38.5 ± 2.22
Human (adjusted)	4.38 ± 0.31	92.3 ± 1.42	40.4 ± 2.61
Goat (physiological)	12.1 ± 0.03	24.7 ± 0.80	29.9 ± 1.00
Goat (adjusted)	14.9 ± 0.02	26.5 ± 0.36	39.5 ± 0.48
Llama (physiological)	10.4 ± 0.22	28.5 ± 1.06	29.7 ± 1.72
Llama (adjusted)	14.2 ± 0.11	28.5 ± 0.61	40.3 ± 1.12
Rooster (physiological)	2.17 ± 0.02	126 ± 5.20	27.4 ± 1.32
Rooster (adjusted)	2.92 ± 0.07	131 ± 2.84	38.3 ± 1.69

Figure 2.4 shows the AMVN perfusion rate (PR) of each species at sample physiological and average human HCTs. PR of human (black circles), goat (blue squares), rooster (green diamonds) and llama (red triangles) RBCs suspended in glucose, ATP, saline, phosphate (GASP) buffer at HCT adjusted to 40% (Fig. 2.4a), or sample's physiologic HCT (Fig. 2.4b) was measured under no pressure difference for the first 60 seconds and 10 cmH_2O for the following 180 seconds. Values shown are mean ± SD (n = 6 for human, n = 4 for each other species). Human samples flowed through the AMVN with the highest PR at both equalized-HCT (Fig. 2.4a) and at sample-specific HCT (Fig. 2.4b). At equalized-HCT, human RBCs flowed at PR = 0.335 ± 0.002 nL/s (n = 6; ± standard error), goat RBCs flowed at 94% the rate of human PR (n = 4; PR = 0.318 ± 0.003 nL/s), llama at 59% (n = 4; PR = 1.96 ± 0.002 nL/s) and rooster at 66% (n = 4; PR = 0.222 ± 0.002 nL/s) (Fig. 2.4a). At sample-specific HCT, human RBCs flowed at PR = 0.455 ± 0.001 nL/s (n = 6; ± standard error), llama RBCs flowed much more quickly than at equalized-HCT at 83% the rate of human PR (n = 4; PR = 0.378 ± 0.003 nL/s), followed by goat at 80% (n = 4; PR = 0.366 ± 0.009 nL/s) and rooster at 47% (n = 4; PR

= 0.214 ± 0.001 nL/s) (Fig. 2.4b). In summary, human RBC PR is faster than other species' RBCs in both cases, and human and llama RBC PRs are faster at physiological HCT, while goat and rooster RBC PRs are not very affected by the change to 40% HCT.

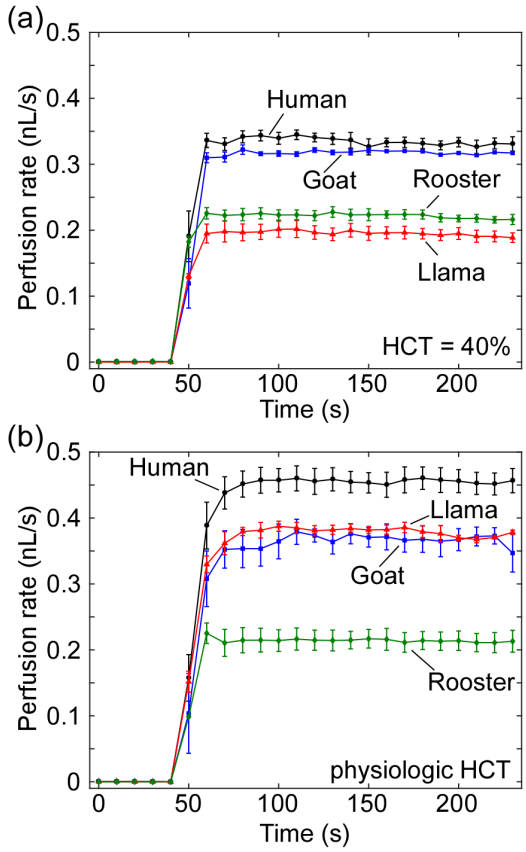

Figure 2.4: The artificial microvascular network (AMVN) perfusion rate (PR) of each species at sample physiological and average human hematocrits (HCTs).

MatLab's (MathWorks, Natick, MA, USA) built-in Farneback optical flow tracking algorithm was used to quantify the motion of RBCs as they flowed through the microcapillary area of the AMVN for samples at sample-specific HCT in order to enable calculation of the ratio of transverse flow to total flow experienced by each species' RBCs. Tracking between frames classified motion, with intuitive results showing the majority of flow along the direction of negative pressure in the network (human sample

results shown in (Fig. 2.5a) and squeezing around misaligned bifurcations (Fig. 2.3c) to flow faster in wider channels and along edges with lower curvature and greater flow angle (3.2 x magnification in Fig. 2.5a(i)). Average RBC flow over the entire time course displayed with a quiver plot confirmed motion through the capillary-network as expected, with more flux through larger channels (human sample results shown in Fig. 2.5b) and away from more acute flow angles caused by bifurcations (Fig. 2.5b(i)). Optical flow vector magnitudes from all frames, binned into one of 360 discreet angles corresponding with each vector's direction, showed a distinct polar histogram signature for each species, where goat RBCs (smallest MCV) experienced a greater portion of flow at angles misaligned with the negative pressure gradient and resulting fluidic shear stress in the channels, followed by the more directly aligned flow of human RBCs, llama RBCs and rooster RBCs (Fig. 2.5c). The transverse flow ratio showed that under identical flow conditions where samples were simultaneously running through different inlets of the same device, goat RBCs experienced 147% of the transverse motion experienced by human RBCs, llama RBCs experienced 90.0%, and rooster RBCs 68.1%. These transverse motion results do not correlate well with any single property of the sample RBCs whether MCV, RBC count, HCT, EI at 3Pa fluid shear or 30 Pa, or even AMVN PR, neither linearly as observed on a PCA biplot (Fig. 6a), nor by calculating squared Pearson Correlation Coefficient (r^2: 0.50, 0.57, 0.02, 0.11, 0.21, 0.53 respectively), nor when graphed to inspect for a common non-linear relationship.

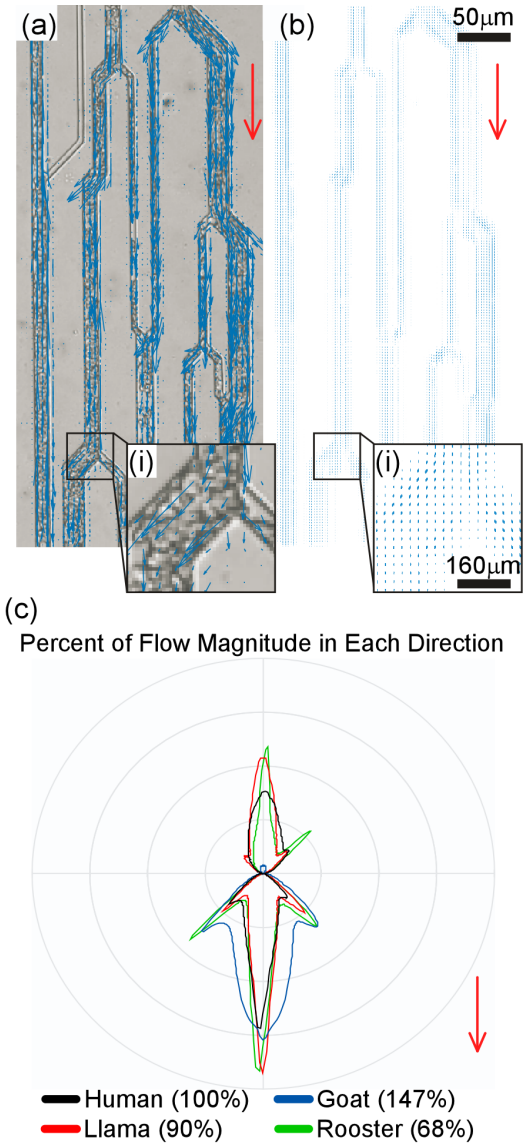

Figure 2.5: Optical flow mapping of red blood cells (RBCs) through the artificial microvascular network (AMVN) capillary sub-network.

Figure 2.6 shows principle component analysis (PCA) biplots of all variables (Fig. 2.6a) and just PR and EIs (Fig. 2.6b), where variable coefficients are shown as vectors and human (black circles), goat (blue squares), rooster (green diamonds) and llama (red triangles) observation scores as points scaled by the maximum coefficient magnitude. Variation in data is 99% explained by the first principal component

(horizontal axis), which is highly dependent on MCV, and 1% explained by the second principal component (vertical axis), which is highly dependent on HCT, so goat and llama points are relatively close together (Fig. 2.6a). Top left quadrant shows a 20x magnification centered on the origin where PR (blue), transverse ratio (TR, green), and EIs (red) going from EI at .3 Pa at ~270° to EI at 30 Pa at ~90° can be seen. After removing MCV, HCT, RBC count and TR, variation in data is 95% explained by the first principal component and 5% by the second (Fig. 2.6a). PR is most correlated with EI at 30 Pa. (c) Squared Pearson Correlation Coefficient (r^2) of PR as a function of EI measured by ektacytometry (LORRCA, RR Mechatronics, Zwaag, The Netherlands) for all animal species confirms that EIs at higher shear stresses more accurately predict the rate of perfusion through the AMVN. Though EI results became illogical at shear stresses above 1.69 Pa for more rigid rooster and llama RBCs (Fig. 2.2), r^2 correlation to AMVN results was below 0.63 until it reached 0.75 at 3 Pa and rose nearly logarithmically to a maximum of 0.93 at 30 Pa (Fig. 2.6c). At fluid shear stresses that most closely mimic the microvascular environment replicated in the AMVN (0.53 and 0.95 Pa) (Resnick et al., 2003), r^2 was at its lowest (0.11 and 0.15 respectively). Conducting PCA on all measured RBC attributes shows shear stresses below which rooster and llama RBCs did not misalign were inversely correlated with PR with respect to the first principal component (Fig. 2.6a) indicating a difference in the relationship between EI and other attributes before and after misalignment. Finally, though goat and llama samples were most similar when considering MCV and HCT (Table 2.1), their EI and PR alone were relatively poorly correlated (Fig. 2.6b) as observed via the distance between their scores on the biplots, which may suggest that deformability and morphology measurements cannot act

as effective substitutes for each other. Taken together, these findings indicate that PR and EI are not similar, especially at ektacytometer shear stresses that mimic those in the AMVN, and that none of the other measured attributes can effectively account for their difference.

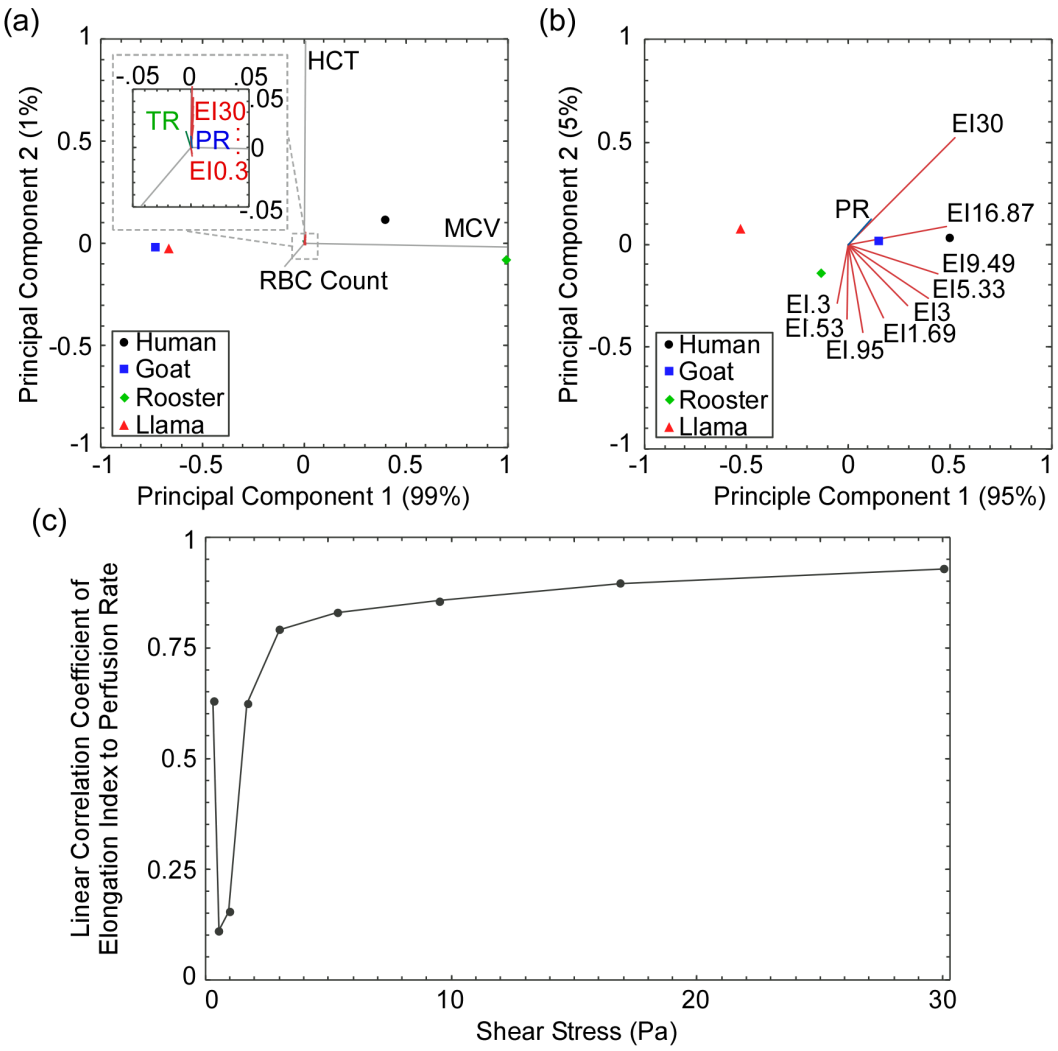

Figure 2.6: Linear relationships between red blood cell (RBC) attributes.

Ektacytometry diffraction patterns, analyzed via fitting to an anomalous diffraction model for elliptical scattering bodies, provided insight into shortcomings of the elliptical fitting procedure in calculating EI of small, rigid, or non-elliptical RBCs to

provide shear elongation information that allows comparison between RBC populations that differ in those attributes. The diffraction patterns produced by human RBCs at 30 Pa fluid shear stress (Fig. 2.7a, d, g, j) are well-defined and elliptical, whereas those of goat RBCs are noisy due to the aberrant morphology of goat RBCs and the increase in gain necessary for the small RBCs to produce a large enough diffraction pattern outside of the range of the masked central laser beam to be identified by the built-in ellipse fitting program (Fig. 2.7d(i,iii)). The cross-like diffraction patterns produced by rooster RBCs at 30 Pa (Fig. 2.7g(i,iii)) indicate a superposition of a non-deforming or misaligning rigid RBC population and a population of less rigid RBCs that are shear deforming into the expected ellipses, as they produce a pattern similar to those observed with human sickle cell RBC populations described to originate from the same varying intrapopulation rigidity effect (Bessis & Mohandas, 1978; Rabai et al., 2014; Renoux et al., 2016; G. Streekstra, Dobbe, & Hoekstra, 2010). This effect corroborates a limitation of the assumption in ellipse fitting thresholding and alignment when calculating EI that RBCs align with each other to produce isointensity curves in the diffraction pattern, for populations of RBCs with a wide range of rigidities. Given the assumption that a majority of RBCs align with the shear field in EI calculation, the majority of llama RBCs seem to be misaligned with the direction of fluidic shear stress as indicated by a diffraction pattern that is wider than it is long with respect to the direction of fluid flow (Fig. 2.7j(i,iii)).

When the model diffraction patterns generated by the anomalous diffraction equation for elliptical scattering objects aligned with the direction of fluid shear stress (Fig. 2.7a(ii), d(ii), g(ii), j(ii)) are fit to corresponding experimental diffraction patterns

for each species by manually minimizing Euclidean distance between the radial intensity of the experimental (Fig. 2.7b, e, h, k; blue lines) and model (orange lines) diffraction patterns, we find the error of assuming elliptical shape was 56.1% greater for goat, 72.8% greater for rooster and 109% greater for llama than it was for human RBCs. Inspecting the average 3-dimensional scattering ellipsoid found by using the optimally fit model to calculate dimensions of the ellipsoid (Fig. 2.7c, f, i, l) reveals unrealistically thin 3-dimensional models of average goat (Fig. 2.7f) and llama RBCs (Fig. 2.7l), indicating that the fitting did not produce realistic values for the size parameter α. Taken together, these findings suggest that neither goat, nor rooster, nor llama RBC EI can be estimated via ektacytometry using standard procedure and the built-in ellipse fitting software to quantify shear deformability.

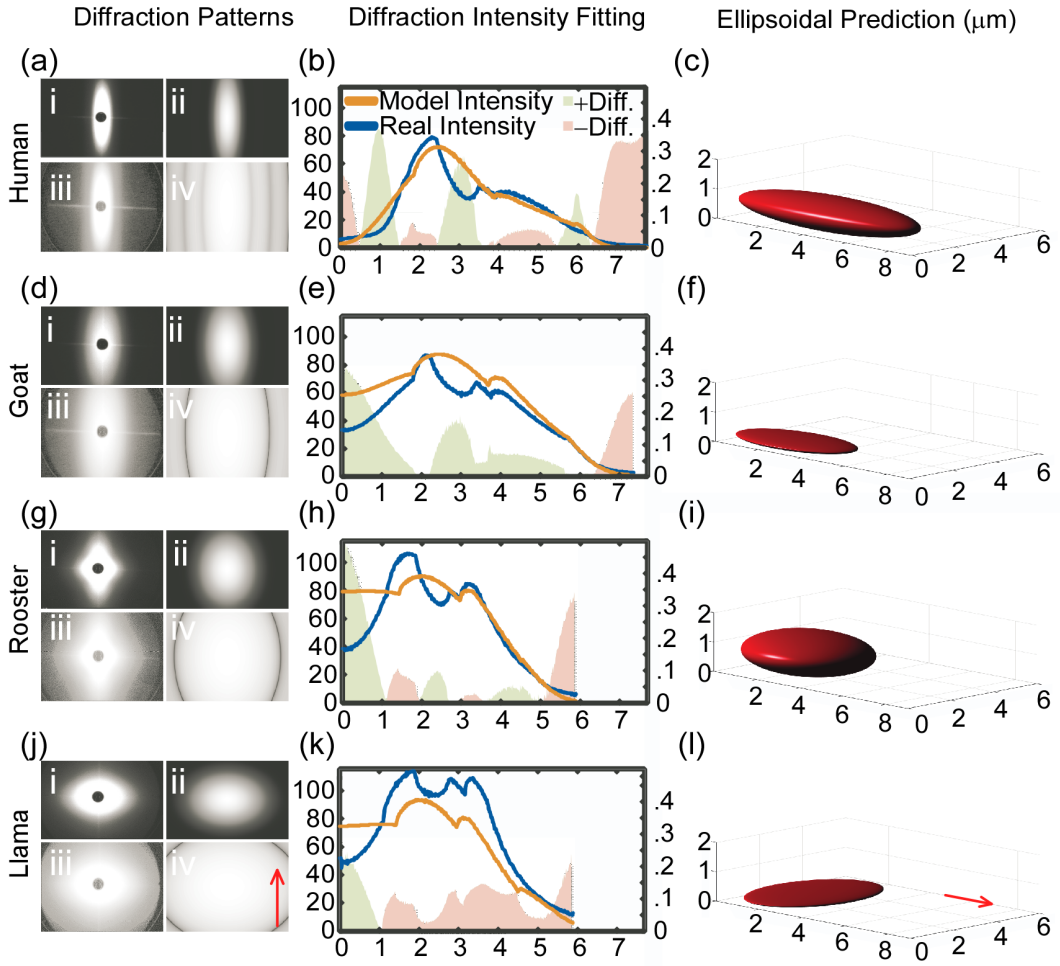

Figure 2.7: 3D ellipsoidal anomalous diffraction model of red blood cells (RBCs) from ektacytometry diffraction patterns.

2.5 Discussion

The relationship between AMVN perfusion and ektacytometry shear elongation measurement was tested with a morphologically and biophysically diverse set of human and non-human RBCs to demonstrate multiple challenges to diagnosing and treating pathological RBC populations using EI. Rooster and llama RBCs underwent rotation to misalign with the direction of shear (Figs. 2.2, 2.7), possibly exhibiting Jeffery orbits,

phenomena wherein rigid objects with ellipsoidal dimensions periodically spin in shear fields, theoretically in an effort to minimize energy (Hinch & Leal, 1979). Though the phenomenon can be predicted for objects of certain morphologies under certain rheological conditions, no model yet describes all observations of rotation in shear. As a result, the extent of spinning and alignment in the ektacytometer is difficult to predict, and there is little assurance that EI will depend only on shear elongation potential for tested fluid shear ranges, especially for RBC populations with some rigid or morphologically aberrant RBCs. By modeling anticipated RBC shape using the same ektacytometer outputs used to calculate EI, we confirm that EI measurements rely on false or poorly understood assumptions. Using the anomalous diffraction equation to build 3D models of the RBCs of each species from their diffraction patterns and the resulting aspect ratio estimated by the ektacytometer software to compute EI, produces insufficient fitting of experimental diffraction pattern intensity to that of the model, resulting in unrealistic 3D dimensions for goat, rooster and llama RBCs (Fig. 2.7).

In specific cases, miscalculation arising from rotation has been exploited using experimentation and diffraction modeling tailored to glean information about the fraction of rotating RBCs in a population (Bessis & Mohandas, 1978; Rabai et al., 2014; Renoux et al., 2016; G. Streekstra et al., 2010), however the problem remains to design a device that produces a measurement that can be compared within and across diverse pathological and healthy RBC populations in the clinic with RBCs of varying rigidities and morphologies. The unpredictable behavior of aberrant RBCs in the ektacytometer affects EI measurements in a way that as of yet has no clear physiological relevance. AMVN PR measurement circumvents this lack of physiological relationship by providing an

intuitive, functional measure of deformability that approximates conditions *in vivo*. However, since the AMVN combines many of the rheological effects observed *in vivo* into one measurement, it is not as directly related to a single biophysical parameter of RBCs as EI is to membrane shear modulus. Still, even under perfect conditions and no rotation, extensive modeling and adding steps to the EI protocol is required to estimate shear modulus from ektacytometry (Liu et al., 2007). Given the complexity of measuring deformability across a population of RBCs and our insufficient understanding of biophysical influences on hemorheology to isolate the effect of RBC deformability on physiologically relevant RBC flow, the AMVN can provide an alternative solution to producing clinically relevant measurements that quantify realistic influences of RBC deformability on blood perfusion dynamics.

The high correlation between PR and EI at higher than physiological fluid shear stress (Fig. 2.6c) may indicate that problems associated with rotation, misalignment and accurate aspect ratio calculation of rigid or morphologically aberrant RBCs may actually improve prediction of PR from EI. However, a previous study on glutaraldehyde treated RBCs showed better correlation in different shear ranges depending on the amount of glutaraldehyde used or also the percentage of glutaraldehyde-treated RBCs in the population (Sosa et al., 2014) . The same study also showed that while diamide treatment affected EI it did not affect PR or micropore filtration rate. The difference between these two treatments is biophysical in nature, as glutaraldehyde crosslinks structural proteins in the cytosol, cytoskeleton and transmembrane region of RBCs whereas diamide only crosslinks spectrin, the major cytoskeletal protein in RBCs. These findings underscore the different biophysical components that influence each type of deformation whether

shearing, bending or expanding, and hint at the different potential influence of each on perfusion through a microvascular network or elongation in an ektacytometer. As the cytoskeleton is the main biophysical component affecting shear deformation (Li, Lykotrafitis, Dao, & Suresh, 2007), one can hypothesize that EI would be more sensitive to diamide treatment than PR. However, PR may be a more sensitive biomarker for pathologies that cause changes in the RBC lipid membrane, known to be the major influencer of bending and expanding deformation (Mohandas & Evans, 1994), as observed in studies on RBC washing in human serum albumin (HSA) and after storage lesion (Khanal et al., 2018; Reinhart et al., 2015). Storage lesion, like glutaraldehyde treatment, is marked by multiple biophysical changes to RBCs, notably the shedding of the RBC lipid membrane by vesiculation (Tinmouth & Chin-Yee, 2001). HSA on the other hand has membrane-rescuing properties (Reinhart et al., 2015). Taken together, these findings suggest that PR and EI are affected differently by multiple modes of deformability with unique biophysical dependencies. Thus, the weak relationship between EI and PR is confirmed in this study for every ektacytometer shear rate, even at shear rates that mimic those in the AMVN (Fig. 2.6).

Other hematological metrics are also weakly correlated with both PR and EI (Fig. 2.6a,b). Non-deformability-based metrics capture most of the variability between the samples (Fig. 2.6a). Though HCT and MCV are related by RBC count because RBC count counteracts MCV to maintain HCT within a narrower range than MCV or RBC count between species (Table 2.1), PR at normalized HCT correlates more strongly with physiological HCT than with physiological MCV or RBC count (Fig. 2.6a), such that when HCT between species is forced within a narrower range by expanding the range of

RBC count, then PR is also forced within a narrower range (Fig. 2.4). Thus normalizing HCT between samples removes the effects of HCT on PR to best isolate the influence of biophysical deformability on PR. Controlling for HCT as opposed to RBC count was also supported by transverse ratio data that shows that RBCs with higher MCV generally experience less transverse motion at physiological HCT (Fig. 2.5), which is at least partially compensated for by the intuition that they also experience fewer collisions. This suggests that normalized-HCT PR would provide less convoluted standardized information about the effects of rigidity on PR than normalized-RBC-count PR which would not account for differences in cell-cell or cell-wall interaction strength. Resuspending RBCs in GASP to adjust HCT and control suspending medium however did narrow the range of MCV ($p<.001$, Table 2.1), possibly due to the most volumetrically aberrant RBCs bursting from shear or packing force in the centrifuge, as abnormal size may be an indication of membrane problems. Tellingly, the range of llama MCV decreased the least after HCT adjustment, potentially because their higher rigidity prevented bursting in the centrifuge. As a result, centrifugation rate must be minimized, instead increasing centrifugation time, when performing HCT adjustment and leukoreduction for fragile RBC samples. Given weak correlation between PR and hematological parameters other than HCT, and the ability to control for HCT in PR measurements, PR can isolate a realistic superposition of the effects of RBC single-cell biophysics on blood flow. Further, given that EI also does not correlate well with PR, potentially due to problems with comparable measurement for populations that have rotating RBCs or due to the fact that shear elongation only captures part of the biophysical attributes required for RBCs in blood flow, PR may be more useful in the

clinic for overcoming the lack of understanding of how RBC cellular biophysics contribute to hematological pathologies.

When considering the cost and ease-of-use of ektacytometry and other methods to measure RBC rigidity, the AMVN shows potential to provide realistic information about the influence of pathological RBCs on oxygen delivery potential in the clinic, at least until EI measurement is studied for populations with misaligning RBCs and a more direct relationship between EI measurements, cytoskeletal shear modulus and blood flow is generalized across pathological RBC populations. The AMVN device geometry would need to be standardized between studies so results can be directly compared, and PR measurement would benefit from a less labor-intensive method, ideally eliminating the need for a microscope to improve cost and efficiency as done for other microfluidic flow rate measurements (Lien & Vollmer, 2007). However, even with the requirement to re-suspend RBCs in GASP buffer to compare PRs, as in this study, the AMVN intuitively shows how RBC morphology and rigidity influence blood perfusion *in vivo*, providing a quantitative, functional measure of RBC quality for pathological RBC populations with potentially more efficiency and multi-scale physiological relevance than micropipette-, cantilever-, magnet-, rheometry-, dielectric-, thermal- or optical-based methods that probe RBC mechanical properties(Duprat & Shore, 2015).

In summary, we were able to compare PR measurements across four species with diverse RBC morphologies and biophysics to show that traditional hematological measurements and EI, the standard ektacytometry measure of shear cytoskeletal elasticity, correlate weakly with AMVN PR across these species. Additionally, by examining AMVN flow patterns and PR at multiple HCTs, we demonstrated that HCT

could be equalized prior to PR measurement to control for differences in oxygen carrying capacity between samples (assuming similar mean cellular hemoglobin concentration) and to isolate RBC cellular features that contribute to oxygen delivery capacity. Further, PR seems to produce intuitive results for a wide range of samples with pathological morphologies, rigidities and HCTs, as demonstrated by more rigid and less morphologically uniform llama RBCs that experienced a 48% decrease in PR whereas similarly-sized goat RBCs only experienced a 13% decrease in PR after similar increases in HCT (36% for llama, and 32% for goat) (Fig. 2.4). Finally, we used PCA, Pearson's Linear Correlation Coefficient and an anomalous diffraction model to examine at which fluid shear rates EI correlates best with PR and to quantify the degree of error in high shear EI measurements of rigid or small RBCs that correlate well with PR, showing that high shear EI measurements of misaligning RBC populations assume increasingly unrealistic aspect ratios of elongating RBCs and are prone to large and unpredictable error.

2.6 Conclusions

Taken together these results indicate that neither EI, nor MCV, nor RBC counts, nor HCT were able to reliably predict PR across a population of aberrant nonhuman RBCs. As the AMVN has been shown to mimic many aspects of the complex environment found in the microvasculature (Burns et al., 2012; Sosa et al., 2014), PR may be a better indication of hemorheology *in vivo* than the other RBC parameters used in this study for pathological RBC populations.

CHAPTER 3 EXPLOITING RBC FLOW DYNAMICS TO REMOVE WASTE AND LESS DEFORMABLE RBCs FROM STORED RBC UNITS FOR TRANSFUSION: A prototype of a simple RBC washing apparatus based on microscale sedimentation in normal gravity

3.1 Introduction

Observing the large dependence of flow dynamics on RBC morphology, we recognize the opportunity to enrich morphologically healthy RBCs in laminar flow from those that have suffered membrane damage. A scenario in which such a device would be essential, is for the removal of poorly-preserved RBCs in stored RBC units prior to transfusion. Such washing is currently conducted via costly centrifugation, wherein storage medium is removed from RBCs sedimented at ~1500 g for 15 min. In this chapter we describe initial prototyping and modeling of a passive RBC washing device which intermittently removes storage medium along with morphologically compromised RBCs that sediment slowly relative to those that are healthy.

3.2 Background

For decades now, the most frequent procedure performed in U.S. Hospitals has been blood transfusion (Pfuntner, Wier, & Stocks, 2006). Despite the recent, widespread adoption of restrictive transfusion practices and allogeneic blood salvage (Bennett-Guerrero et al., 2007; Carson, Kleinman, Silvergleid, & Tirnauer, 2018; Frank et al., 2013; Klein, Spahn, & Carson, 2007), transfusion rates continue to grow by approximately 30%/yr such that over 1% of the US population undergoes transfusion

yearly (Pfuntner et al., 2006). The numerous reasons for red blood cell (RBC) transfusion can be categorized into acute circumstances (ie major surgery, serious injury, severe infection, and acute liver conditions) and chronic conditions (drugs or therapies that cause anemia such as chemo and radiation in cancer, and heritable blood disorders including hemoglobinopathies and various red blood cell or bone marrow mutations); the reason for this dichotomization is that the quality of stored blood required as well as the blood product testing and preparation methods available share similar standards within each category. For example, patients requiring chronic transfusions often receive fresher and more thoroughly matched blood products since the risk for accumulation of storage byproducts (such as cell-free-iron) is higher, and the decreased urgency of the transfusion procedure allows for more comprehensive processing (such as saline washing and major-crossmatching) of their transfused RBC products, respectively.

RBC transfusion efficacy has been validated to produce general guidelines regarding use-cases for transfusion, therapeutic standards of care, and blood banking best practices. Today many of these guidelines are disconcertingly outdated, especially because transfusion is so ubiquitous. Yet, pending the empirical evidence that modern technology should have provided us long ago, decades-old practices are still followed, nevertheless, with significantly positive outcomes. Generally, RBC product transfusion follows the "10/30" rule (that is, doctors are recommended to maintain patient hemoglobin (Hb) concentration above 10g/dL and hematocrit (HCT) above 30%). A rough estimation shows that each packed red blood cell unit should increase [Hb] by 1g/dL and HCT by 3% in an average-sized human (Verhoeven, 2004). As mentioned above, independent studies, which have indicated that pruning of transfusion practices to

7g/dL in many disease-states preserves resources and leads to lower 30-day patient mortality, have led to widespread adoption of more restrictive transfusion practices (Bennett-Guerrero et al., 2007; Carson et al., 2018; Frank et al., 2013; Klein et al., 2007). The 7-10g/dL [Hb] guidelines are based off of at least four studies, spanning 1958 to 2014, that have shown that anemia increases 30day mortality in pre- and post-operative settings, thus leading to the belief that adequate tissue oxygenation is necessary for survival particularly when the body is under physical stress (Carson et al., 2018; Middelburg, van de Watering, Briët, & van der Bom, 2013). Stepping away from the clinic and into the blood bank, we see similar developments. U.S. blood banks have allowed blood to be stored for 42days under refrigeration at 4°C since the mid-20th century; the 42day threshold is based on the redness of the RBC storage solution as an indicator of hemolysis (J. Hess, 2014; Zimring, 2015). Other countries have comparable standards, with much of Europe adopting a 35day expiration policy; faster turnover increases the risk of blood shortages, but may improve the quality of transfused products and consequently the reduction of transfusion-related adverse events (for reference, the U.S. collects more than 14million units of blood a year and transfuses 99% of it into roughly 5million patients (Bennett-Guerrero et al., 2007; Bhaduri, Kandel, Brugnara, Tangella, & Popescu, 2014; Silva et al., 2012)). This tradeoff fuels our desire to know how long blood products can be stored without decreasing the clinical efficacy of their transfusion. Recent advances have also led to changes in blood banking procedures with regards to luekoreducing practically all RBC units and washing some RBC units in saline for specific cases (often involving chronic transfusion) (Flegel, Natanson, & Klein, 2014; J. R. Hess, 2010).

Given the prevalence of RBC transfusion, discussion of the topic throughout the research community has been staggering. With multiple journals dedicated solely to the investigation of the therapy, and roughly 150 review papers and 1500 original research papers published on the subject in the last 5 years found via meta-analysis of PubMed results, the rate of content is steadily increasing, further diluting the opportunity for definitive research or all-encompassing review articles to be published. One particular question has been of interest in recent years: as improvements in blood banking technology become tangible, which biomarkers in stored blood can act as reliable indicators of clinical outcomes? The significance of this question is reflected in the resounding industry response to research advances in the field: leukoreduction was widely adopted in blood banks over the course of just a few years after showing minor improvements in transfusion outcomes (Bessos & Seghatchian, 2005; Flegel et al., 2014; J. R. Hess, 2010; Van de Watering, 2011).

The cornerstone of the above question relies on relating the physiological changes that stored red blood cell products undergo over time (referred to as storage lesion) to the clinical outcomes of transfusing old red blood cell products into patients. This challenge has been approached not only by exploring biomarkers available in blood bags, but also by conducting massive clinical trials aimed at measuring a wide array of transfusion patient outcomes. Still many of these studies struggle to bridge the gap between well-controlled groups of storage lesion biomarkers to specific and significant clinical outcomes.

Given the breadth of review articles published on the relationship between storage lesion and clinical outcomes of transfusion – roughly 30 in the past 5 years – many

recommendations have been made to try and overcome this troublesome lack of progress in future experiments and trials. These include conducting small sample studies and running pretrial computer simulations to help adjust clinical patient enrollment and RBC product age delimitations to yield a desired statistical power (Pereira, 2013), controlling for the number of red blood cells or volume of suspending medium or hematocrit of RBC product transfused (depending on where the lesion biomarker in question is contained) (Zimring, 2015), controlling for blood banking protocols for suspension media or to leukoreduce, irradiate or otherwise process RBC units (Flegel et al., 2014; J. Hess, 2014; Radwanski et al., 2013), taking larger scale approaches either through meta-studies (Edgren et al., 2010) or through the measurement of most available biomarkers, or conversely by homing in on specific lesion and transfusion outcome biomarkers as they relate to individual disease pathologies (Glynn, 2010).

In the most comprehensive study of storage lesion as it relates to sickle cell disease to date, Fields et al. could not detect a significant increase in the number of acute chest syndrome (ACS) episodes in children with sickle cell disease transfused with old blood. As a result, however, they called for the urgent need for more studies on the topic in order to improve transfusion outcomes in this sensitive population (Fields et al., 2015).

A potential lesion and transfusion outcome biomarker for hemolytic pathologies is cell free hemoglobin (cf-Hb) (specifically due to its metabolism with nitric oxide (NO)). Excess cf-Hb scavenges NO, which prevents NO from performing its vasodilatory function, causing adverse clinical outcomes such as painful crises common in sickle cell disease. Thus many suggest the monitoring of cf-Hb in the blood bag, and also examining cf-Hb and/or NO in the patient to improve transfusion outcomes, especially in sickle cell

patients (Bennett-Guerrero et al., 2007; D'Alessandro, Liumbruno, Grazzini, & Zolla, 2010; Pavenski, Saidenberg, Lavoie, Tokessy, & Branch, 2012; Rinalducci & Zolla, 2015).

Additionally, Klein et al. shows the imminent danger of alloimmunization in these patients. Alloimmunization, causes symptoms of acute hemolysis similar to a severe febrile reaction, and occurs at about 1% per unit transfused, putting patients who receive chronic transfusions at high risk (Klein et al., 2007). Allomunization may increase with oxidative stress and leukocyte lysis during storage lesion (Klein et al., 2007).

Klein also underscores the necessity to monitor transfusion-related iron overload in chronic transfusion cases, especially in patients with thalassemia. Due to the body's difficulty with removing iron, chronic transfusion patients often add 5-8g of iron to their body stores yearly. Increased iron can lead to endocrine dysfunction, cardiac disease and increased risk of infection. Thus serum iron must be closely supervised and chelation therapy must be administered whenever necessary (Klein et al., 2007).

In this study, we attempt to circumnavigate the complexity of relating lesion biomarkers to adverse transfusion outcomes by prototyping a device that can affordably and efficiently wash RBC units in normal gravity at the bedside in-line as they are transfused. Such a device could obviate the need for selective washing of RBC units for the most sensitive patients only, given that current gold-standard industrial RBC washing centrifuges are expensive and cumbersome, and require coordination of hospitals with blood banks to avoid wasting units. In this preliminary work we focus on the design of the passive blood washing device by modeling RBC flow and sedimentation inside tubing to estimate some of its key specifications. We use a Poiseuille flow model and Stoke's

Law to estimate the maximum distance at which healthy RBCs will sediment in the tubing of the passive device, and produce a computer simulation of sedimentation (COMSOL Multiphysics, COMSOL Inc., Burlington, MA, USA) to visualize the shape of the sedimenting layer of RBCs and optimize the cross-sectional shape of the tubing to allow enrichment of the most well-preserved RBCs from storage medium and harmful lesion byproducts.

3.3 Materials and Methods

Our protype device was built by coiling plastic tubing (Tygon microbore, Cole Parmer, Vernon Hills, Illinois) (i.d. 1 mm) around a cardboard column, and inserting three bifurcations in the tubing that skim storage medium and lesion byproducts from the sedimenting RBC layer. The bifurcations were made by laying two segments of tubing (i.d. 1 mm and 0.22 mm medical grade micro-urethane, Scientific Commodities, Lake Havasu City, Arizona) in the desired shape on top of a layer of cured PDMS and pouring uncured PDMS on top to cover the tubing. When cured, the tube segments were removed, leaving a 2 cm^2 PDMS bifurcation joint that the device tubing was press-fit into. The diluted RBC unit was driven through the device at a constant flow rate with a syringe pump (NE-1000, New Era Pump Systems, Farmingdale, NY), and waste and washed RBC sediment were separated via three bifurcations placed along the tubing.

To estimate the sedimentation distance (the distance that an RBC will travel along the tubing in the flow of the suspending saline before it sediments from the top to the bottom of the tube), we calculated the projectile of a settling RBC in flow described by

the Navier-Stokes Equation for the incompressible fluid 10% HCT saline under the external syringe-pump pressure p as

$$\frac{\partial u}{\partial t}+(\vec{u}\cdot\nabla)\vec{u}=-\frac{1}{\varrho}\nabla p+\nu\nabla^2\vec{u}, \tag{3.1}$$

where $\vec{u}(r,\Theta,z,t)$ is the velocity field of the fluid in cylindrical coordinates, and ν is the kinematic viscosity ($\frac{\mu}{\varrho}$, the ratio of the viscosity to the density) of the 10% HCT saline.

Under the assumptions that the flow is steady (i.e., $\frac{\partial u}{\partial t}=0$), and unidirectional in the z-direction {(i.e., $u_r=u_\Theta=0$, no radial or swirl components) & (i.e., $(\vec{u}\cdot\nabla)\vec{u}=0$, the velocity is perpendicular to its gradient)}, the non-linear second-order PDE becomes a linear, second-order, PDE,

$$0=-\nabla p+\nu\nabla^2\vec{u}, \tag{3.2}$$

which in expanded notation using 3D cylindrical coordinates, is

$$0=-\frac{\partial p}{\partial z}+\nu\left[\frac{1}{r}\frac{\partial}{\partial r}\left(r\frac{\partial u_z}{\partial r}\right)+\frac{1}{r^2}\frac{\partial^2 u_z}{\partial \Theta^2}+\frac{\partial^2 u_z}{\partial z^2}\right]. \tag{3.3}$$

Further, assuming the flow is axisymmetric (i.e., $\frac{\partial u_z}{\partial \Theta}=0$) and fully developed (i.e., $\frac{\partial u_z}{\partial z}=0$), we get a linear, second-order, ODE,

$$0=-\frac{1}{\nu}\frac{\partial p}{\partial z}+\frac{1}{r}\frac{\partial}{\partial r}\left(r\frac{\partial u_z}{\partial r}\right), \tag{3.4}$$

with a discrete solution,

$$u_z=\frac{1}{4\nu}\frac{\partial p}{\partial z}r^2+c_1 ln(r)+c_2. \tag{3.5}$$

Solving with boundary conditions (a) that u_z is defined and finite at r=0 we get c_1=0, and (b) that u_z=0 at r=R, where R is the radius of the inner diameter of the tubing, indicating that there is no slip at wall of the tubing, we get $c_2 = -\frac{1}{4\nu}\frac{\partial p}{\partial z}R^2$, yielding the Hagen-Poiseuille flow equation,

$$u_z = -\frac{R^2}{4\nu}\frac{\partial p}{\partial z}\left(1-\left(\frac{r}{R}\right)^2\right), \tag{3.6}$$

for the velocity of the fluid in the z-direction with respect to the radial position.

To put this equation in terms of flow rate induced by a syringe pump, Q=ūA, where ū is the average velocity of the fluid in the z-direction, and $A=2\pi R^2$ is the cross-sectional area of the tube, we first find ū by integrating u_z over the entire cross-sectional area, and then dividing by the cross-sectional area to yield,

$$\bar{u} = \frac{1}{2\pi R^2}\int_{\Theta=0}^{2\pi}\int_{r=0}^{R} -\frac{R^2}{4\nu}\frac{\partial p}{\partial z}\left(1-\left(\frac{r}{R}\right)^2\right) r\,dr\,d\Theta, \tag{3.7}$$

in cylindrical coordinates.

The solution is $\bar{u} = \frac{-R^2}{8\nu}\frac{\partial p}{\partial z}$, thus $Q = \frac{-R^2}{8\nu}\frac{\partial p}{\partial z}A$ and the coefficient of u_z from (3.6), $-\frac{R^2}{4\nu}\frac{\partial p}{\partial z} = \frac{2Q}{A}$, yielding a u_z in terms of Q of

$$u_z = \frac{2Q}{\pi R^2}\left(1-\left(\frac{r}{R}\right)^2\right). \tag{3.8}$$

Next, considering the radial position of an RBC as a function of time, we find that $r(t)=vt$ where v is the velocity of the RBC in the radial direction, which is limited strictly

to the vertical axis due to gravitational forces of weight and buoyancy producing a net force downward of

$$F_g = \Delta\varrho g \frac{4}{3}\pi a^3, \tag{3.9}$$

assuming the RBCs are roughly spherical, and a viscous drag force upward

$$F_d = 6\pi\mu a v, \tag{3.10}$$

assuming the downward flow of the RBC in the 10% HCT saline is laminar (to be validated *a posteriori*), where $\Delta\varrho$ is the difference in density between RBC and 10% HCT saline, g is acceleration due to gravity, a is the radius of the RBC, μ is viscosity of the fluid, and v is vertical velocity of the RBC . Assuming terminal velocity is reached within a negligible time (i.e., the acceleration of the RBC to its settling velocity is reached quickly relative to the time it spends at its settling velocity, to also be validated *a posteriori*), we use Newton's Second Law with $a=0$ to equate F_g to F_d and solve for v to yield Stokes' Law,

$$v = \frac{2}{9}\frac{a^2 g \Delta\varrho}{\mu}, \tag{3.11}$$

assuming an RBC radius of $a=3.5E{-}6(m)$, a $\Delta\varrho = \varrho_{rbc} - \varrho_{fluid} = 1125 - 1070 = 108(\frac{kg}{m^3})$, and a $\mu = 2E{-}3(\frac{kg}{m \cdot s})$ we find $v = 1.4(\frac{\mu m}{s})$.

To validate our assumption of laminarity, we find the velocity of RBCs settling through 1mm in 10% saline to have Reynold's number $R_e = \frac{\varrho v L}{\mu}$, with $\varrho = 1017(\frac{kg}{m^3})$ and $\mu = 2E{-}3(\frac{kg}{m \cdot s})$ defined above as density and viscosity of the fluid, $v = 1.4E{-}6(\frac{m}{s})$ is the

vertical velocity of the RBCs unrelated to the fluid flow found above, and L=1E−3(m) is the characteristic length scale (the diameter of the tubing), to be equal to R_e=7E−4<<1, which is well within the regime dictating laminar flow. Next, to validate our assumption that terminal velocity is reached within a negligible time, we calculate the time to terminal velocity and compare the time it takes the RBC to sediment the entire diameter of the tubing at terminal velocity. Using Newton's 2nd Law F=ma to yield

$$a=\frac{dv}{dt}=\frac{F_d-F_g}{m}=\frac{6\pi\mu av-\Delta\varrho g\frac{4}{3}\pi a^3}{m}, \tag{3.12}$$

we can solve for

$$dt=\frac{m}{6\pi\mu av-\Delta\varrho g\frac{4}{3}\pi a^3}dv. \tag{3.13}$$

Integrating from rest (velocity of 0) to terminal velocity v_f we get

$$t=\frac{m}{6\pi\mu a}log(\frac{1+6\pi\mu av_t}{\Delta\varrho g\frac{4}{3}\pi a^3}), \tag{3.14}$$

which, using m=27E−12(g) and all other parameters defined above, is equal to t_{v_t}=2E-8(s) or is 2.8E-9% of the $\frac{2R}{v_t}$= 714(s) it takes for an RBC to settle across the diameter of the 1mm tube. Thus, our assumption of negligible time to terminal velocity holds.

With $r(t)$=vt we find that T=R/v where T is the time it takes the RBC to settle a distance of R, the radius of the tubing. Thus, the full equation describing the projectile motion of the RBC in the Hagen-Poiseuille flow is

$$z(t)=z(0)+\int_0^t u_z(r(t))dt\,, \tag{3.15}$$

where $z(0)=0$, $t=R/v$, and $u_z(r(t))$ is (3.8) with vt substituted for r, such that

$$z(T)=L=\int_0^{R/v}\frac{2Q}{\pi R^2}(1-(\frac{vt}{R})^2)dt=\frac{2Q}{\pi R^2}\frac{2R}{3v}\,, \tag{3.16}$$

where L is the sedimentation distance. Finally, substituting (3.11) into (3.16) and simplifying yields

$$L=\frac{6Q\mu}{\pi a^2 g\Delta\varrho R}\,, \tag{3.17}$$

with the flow rate from the syringe pump $Q=.5(\frac{ml}{min})=8.\bar{3}E{-}9(\frac{m^3}{s})$, the viscosity of 10% HCT saline $\mu=2E{-}3(\frac{kg}{m\cdot s})$, the radius of an RBC $a=3.5E{-}6(m)$, acceleration due to gravity $g=9.8(\frac{m}{s^2})$ the difference in density between RBCs and 10% HCT saline $\Delta\varrho=\varrho_{rbc}-\varrho_{fluid}=1125-1070=108(\frac{kg}{m^3})$, and the inner diameter of the tubing $R=5E{-}4(m)$, we find that the sedimentation distance of an RBC which sediments in flow from the center of the tube to the bottom (over a distance R) is $L=4.89(m)$. By symmetry, we can deduce that an RBC will travel approximately 9.78 m before it sediments from the top to the bottom of the tube. In order to validate this our model, we relate this distance to the observed sedimentation in a preliminary prototype of the device by analyzing a digital photograph of the tubing using standard image analysis techniques in MatLab (MathWorks, Natick, MA, USA). RBC units (CPD/AS-1, leukoreduced, storage duration

6 weeks) used for testing were obtained from the Gulf Coast Regional Blood Center (Houston, TX), diluted to 10% in normal saline, and washed in the device to produce (n = 6) images for analysis.

We then use the validated model assumptions to quickly computationally simulate sedimentation in tubing of non-cylindrical shapes. We built a multiscale model of spherical particles sedimenting in flow in different shaped channels using COMSOL flow and sedimentation packages (COMSOL Multiphysics, COMSOL Inc., Burlington, MA, USA). For the model to calculate reasonably quickly, we only used one layer of particles at 100% volume fraction (analog of HCT), and greatly decreased the length of tubing to decrease aspect ratio and thus increase mesh fineness, compensating by increasing the difference in density between particle and suspending media. The simulation results were used to improve design of the bifurcation and tubing cross-section shapes, and to allow us to visualize how our prototype device efficiency might change before ordering expensive custom-shaped tubing.

3.4 Results

Figure 3.1 shows an early prototype of the device reported in (Khanal et al., 2018), designed with a 20m length of cylindrical tubing with a y-shaped bifurcation 17m downstream of the inlet used to skim media off of the top of the tubing, followed 6cm downstream by an 8-shaped bifurcation used to skim the bottom-most layer of sedimented RBCs into a transfusion line, and finally another 8-shaped bifurcation 4.8m downstream of the first bifurcations to remove the remaining sedimented RBCs after resettling from disturbance caused while passing over the first bifurcations. Fig 3.1a,b is

compiled from (Khanal et al., 2018). Figure 3.1c shows a close up image of flow through a flipped y-shaped bifurcation showing no visually detectable disturbance of the laminar sedimented RBC layer across the bifurcation in the 1mm diameter tubing at a 0.5ml/min flow rate.

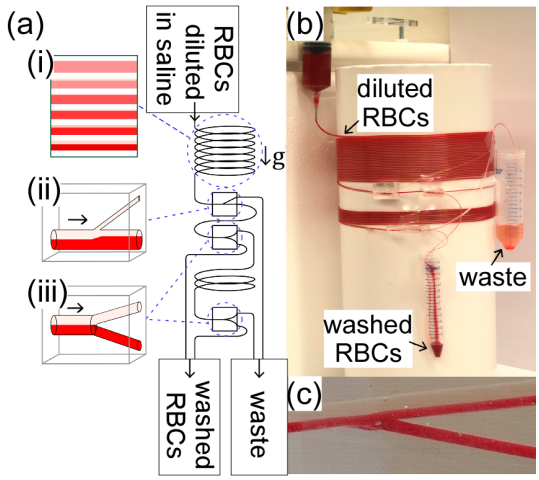

Figure 3.1: Gravity sedimentation blood washing device prototype.

Figure 3.2 shows the results of the methodology used to estimate experimental sedimentation distance, so that it could be compared to our model prediction. An example of a digital image taken from the side of the coiled tubing shows RBCs sedimenting into a thinner and darker layer at the bottom of the tubing as the diluted RBC unit winds downward (Fig 3.2a). Images like this (n = 6) were analyzed with a custom MatLab (MathWorks, Natick, MA, USA) script to calculate the height of the sedimented RBC layer in the tubing at each coil. This height was then converted to volume using the equation for a circular segment assuming a straight line across the cross section of the tubing at the interface between the sedimented and medium layer, and plotted as HCT along the length of the tubing ± 1 SD by scaling the volume to experimental device input and output HCTs measured via hematology analyzer (Medonic, Boule Medical AB,

Spånga, Sweden) (Fig 3.2b). The HCT plateaus at 9.8 m, agreeing well with our model prediction of 9.78 m, validating the model for use in a discreet computational simulation.

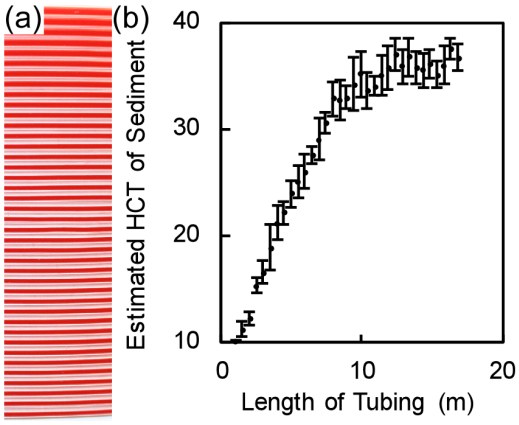

Figure 3.2: Experimental red blood cell (RBC) sedimentation distance analysis.

Figure 3.3 shows the results of multiphysics software (COMSOL Multiphysics, COMSOL Inc., Burlington, MA, USA) modeling used to improve the design of the prototype gravity washing device. Figure 3.3a displays multiphysics software visualization of particle sedimentation in Poiseuille flow showing particles in a short tube from 0 to 98% sedimentation in ~20% increments (top to bottom). Particle density and tube length were adjusted to show the shape of the sedimentation layer through its entire path in a high-resolution cartesian mesh within a reasonable simulation time. Figure 3.3b shows the results of a similar simulation with particle path tracing in tubes of various geometries, displaying different velocity profiles, maximum velocity (v_{max}), and sedimentation distance depending on tube geometry. Such models were used to visualize the inside of the tube to inform design of the 8-shaped bifurcation, though limitations including the assumptions that the particles are spherical and do not roll at the boundaries qualify the results.

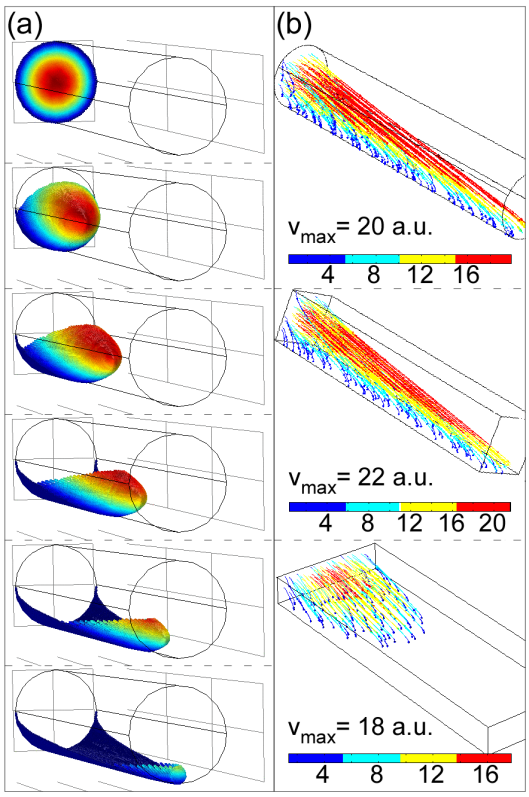

Figure 3.3: Multiphysics software modeling used to improve the design of the prototype gravity washing device.

3.5 Discussion

We conceived of a low-cost device that would wash packed-RBC (pRBC) units in normal saline at the bedside using simple dilution of pRBCs and re-concentration at original HCT in-line using simple sedimentation of RBCs due to gravity. The device would consist of a length of tubing, in which diluted RBCs would sediment to the bottom of the tubing while diluted storage media would be skimmed from the top portion. Design considerations involved selecting an optimal length, cross-sectional shape and cross-sectional area of tubing to increase sedimentation rate and device throughput, along with deciding the location and shape of bifurcations that would skim storage media and RBCs

sedimenting more slowly due to aberrant morphology, while not disturbing the high quality re-concentrated RBCs that are being transfused in-line.

We modelled the distance along the tubing where sedimentation will reach a maximum, by deriving the equation $L = \frac{6Q\mu}{\pi a^2 g \Delta\rho R}$, to find the sedimentation length, L, of a RBC which sediments subject to Stokes's Law in Poiseuille flow (Reynold's number $R_e = 7 \times 10^{-4}$, within the laminar regime). Solving with flow rate from the syringe pump $Q = 0.5\left(\frac{ml}{\min}\right)$, viscosity of 10%HCT in saline $\mu = 2 \times 10^{-3}\left(\frac{kg}{m} \cdot s\right)$, RBC radius $a = 3.5 \times 10^{-6}(m)$, acceleration due to gravity $g = 9.8\left(\frac{m}{s^2}\right)$, the difference in density between an average RBC and 10% HCT RBCs in saline $\Delta\rho = 108\left(\frac{kg}{m^3}\right)$, and the inner diameter of the tubing $R = 5 \times 10^{-4}(m)$, we find that $L = 4.89(m)$ for an RBC to sediment across the radius or 9.78m to sediment across the diameter, from the top of the tube to the bottom. This estimate agreed remarkably well with experimental results as the sedimented RBC layer seems to plateau at this distance (Fig. 3.2).

We were then able to use analogous models to simulate sedimentation in different shapes of tubing, allowing us to observe the shape of the sedimenting layer over the length of the tubing, and evaluate that the cost of using non-cylindrical tubing would not be outweighed by the benefit such tubing could provide in throughput.

3.6 Conclusions

Given the understanding of pathological RBC rheology gained from the analysis of sickle and nonhuman RBCs, we set out to design a device that would wash stored RBCs at the bedside to remove not only biochemical byproducts of storage lesion

suspended in the anticoagulant storage medium, but also morphologically abnormal RBCs that have deteriorated in storage. Previous findings of poor flow and sedimentation of RBCs with properties indicating damage due to storage, along with modeling of flow in simple geometries, inspired design of a washing device that produced a 90% reduction in free protein, 20% increase in AMVN PR, and 45% decrease in proportion of damaged RBCs (echinocytes 2/3, stomatocytes, and spherocytes) analyzed by counting in a hemacytometer, with a throughput of 0.5ml/min at 40%HCT, rivaling expensive and wasteful, though higher throughput, conventional centrifugation-based pRBC washing (Khanal et al., 2018). Improving throughput to 2ml/min at 60%HCT, typically used in transfusion, would make a gravity sedimentation-based device more practical for in-line bedside washing.

CHAPTER 4 MICROFLUIDIC PROCESSING OF WHOLE BLOOD INTO HIGH QUALITY COMPONENTS: The effects of a non-centrifugation-based blood component separation device on RBC, platelet, and plasma

4.1 Introduction

In recognizing the benefit of exploratory work on RBC rheology on designing a novel device for washing, we set out to operate on other components of blood as well, particularly to understand critical aspects of how the quality of platelets and plasma are assessed. A centrifuge-free blood component separation device was designed using RBC sedimentation principles previously described in this work, and particle flow principles described in detail in (Gifford, Spillane, Vignes, & Shevkoplyas, 2014).

4.2 Background

Over 100-million blood component units are transfused worldwide each year, and most of them are prepared from donated whole blood (WB) using costly and inefficient multi-step centrifugation, or bedside apheresis (Organization, 2017). These methods are required to separate WB into its component red blood cell (RBC), platelet, and plasma components soon after donation due to large variation in optimal storage conditions for each component: platelets are stored on an agitator platform for ~6 days kept warm at 20°C, RBCs are stored for ~6 weeks refrigerated at 4°C, and plasma is stored for ~1 year frozen at -18°C (Gifford et al., 2018). As a result, transfusion is limited to settings where financial and logistical resources can accommodate transportation of WB to and from locations with access to dedicated separation devices.

Previous attempts to address this challenge with alternative filtration technologies or manually operated devices, have been unable to produce components at high throughput, and have struggled to preserve any platelets (Brune et al., 2007; Hornsey, McColl, Drummond, & Prowse, 2005; LaLonde, Romero-Creel, Saucedo-Espinosa, & Lapizco-Encinas, 2015; A. P. Wong, Gupta, Shevkoplyas, & Whitesides, 2008). In this work, we present a portable, affordable, highly automated passive separation technology that does not require electricity, and compare the quality of the components it produces with that of components produced by conventional multi-step centrifugation. This device, which separates RBCs from platelet rich plasma (PRP) via sedimentation in normal gravity and then concentrates the platelets in PRP with a high throughput microfluidic device to produce platelet and plasma components, can improve access to transfusion products during natural disasters and events causing an influx of trauma patients, and in chronically resource limited settings.

4.3 Materials and Methods

WB donations (500 ml) were collected from healthy consenting volunteers at the MD Anderson Cancer Center Blood Donor Building (Houston, TX) into bags with 70 ml citrate phosphate dextrose (CPD) anticoagulant (Fenwal, Lake Zurich, IL). Donated bags were then divided into two smaller bags, one passively separated into RBC, platelet and plasma components via the new separation device, and the other by conventional centrifugation-based separation.

Centrifugation-based separation followed standard blood banking procedure, consisting of a soft spin of the WB at 1780 g for 310 s to separate PRP from RBCs, and a

hard spin of the PRP at 4200 g for 350 s to separate platelets from plasma (Allegra X-15R; Beckman Coulter Inc., Brea, CA). RBCs were then mixed with 55 ml of AS-3 solution (Haemonetics Corporation, Braintree, MA) and white blood cells and remaining platelets were removed through a leukoreduction filter. Blood components were stored in heat sealed (TCD B40; Genesis BPS, Ramsey, NJ) bags, disconnected from the blood separation module.

The new separation device pictured in Figure 4.1, consists of a custom expressor, a microfluidic platelet concentrator (MPC), and the components of a standard blood processing kit (123–94; Haemonetics Corporation, Braintree, MA) including tubing, bags, and an RBC leukoreduction filter. The custom expressor includes an aluminum ring (o.d. 8 inches) that holds two aluminum compression plates parallel to each other under a rubber air spring (1B5-500; Goodyear, Akron, OH). The ring is placed on a circular aluminum stand (i.d. 5 inches) allowing adjustment of the angle of the bag to enable both the sedimentation of RBCs in normal gravity and the compression of the bag through the quasi-constant pressure regime of the air spring throughout the PRP expression process as the bag thickness decreases by 50%. The MPC was fabricated using standard soft lithography techniques, to contain 10 controlled incremental filtration (CIF) devices described in detail in (Gifford et al., 2014). The CIF devices were redesigned with an "f_{gap}," or filtered particle size threshold, of 1.04E-4 to concentrate platelet-sized particles ~3x with high throughput, and were sandwiched between a polydimethylsiloxane (PDMS) device that distributed and collected flow into and out of the 10 devices situated in 2 layers, and a flat base (Fig. 4.1c). The photomasks for the 2 CIF layers and the top distribution layer were designed in CAD and printed as chrome on glass (Photo Sciences,

Inc., Torrance, CA). The masks were used to imprint the devices into SU-8 (Microchem, Westborough, MA) spin coated onto 4-inch diameter silicon wafers (University Wafer, South Boston, MA), producing master molds from which devices were cast in PDMS (SylGard 184, Dow Corning Corp, Midland, MI). The depth of the CIF devices was 150μm ±5μm; the width of the central channel was 125μm and the final width of the side channels was 140μm such that the ratio of total flow into the side channel collection port was ~2.5x that into the central collection port (Fig. 4.1d). The layers were bonded by plasma oxidation (Plasmalab 80 Plus, Oxford Instruments, Abingdon, United Kingdom), and appropriate inlet and outlet ports for connecting the tubing and the CIF devices to the distribution layer were bored with biopsy punches (Acuderm, Fort Lauderdale, FL). Tubing was inserted with barbed connectors and heat sealed, and the entire module was incubated first with 1% (w/v) mPEG (MW 5000, Laysan Bio Inc, Arab, AL) in deionized water, and then 1% human serum albumin in PBS, before it was UV (TC312E, Spectroline, Westbury, NY) and heat sterilized. RBCs were allowed to sediment in normal gravity to allow PRP to be expressed into a tube at the top of the bag (Fig. 4.1b). After the PRP was expressed, the MPC module was replaced by a leukoreduction filter connected to a third bag so RBCs could be expressed. The entire procedure consisted of a 150 min RBC sedimentation period, after which PRP was expressed through the MPC device under 10 Psi for ~180 min, and finally RBCs were mixed with AS-3 solution and expressed through the leukoreduction filter in the same manner as in centrifugation-based methods. Figure 4.1 is assembled with permission from (Gifford et al., 2014; Gifford et al., 2018).

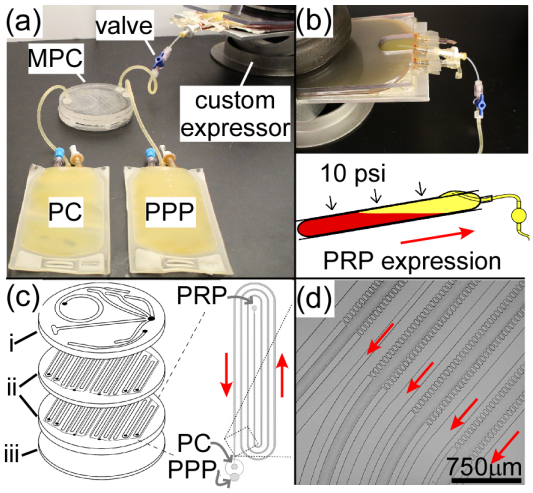

Figure 4.1: Controlled incremental filtration (CIF) -based device for enriching the platelets from platelet-rich plasma (PRP) into transfusion products i.e., platelet concentrate (PC), platelet poor plasma (PPP), and packed red blood cell (pRBC) fractions.

We then assessed the separated RBC quality with ektacytometry, platelet quality with platelet aggregometry, a turbidity-based method similar to bulk RBC aggregometry described earlier, and plasma quality with biochemical assays to ensure no loss of critical proteins and clotting factors in the plasma, as high shear flows can cause protein aggregation and precipitation. Ektacytometry (LORRCA, RR Mechatronics, Zwaag, The Netherlands) was conducted as described in Chapter 1 to measure elongation index (EI) at 3 and 30 Pa. Platelet aggregation was measured for two physiologically-relevant strong agonists (thrombin receptor agonist peptide, TRAP, and adenosine diphosphate, ADP) over 1 minute, and a weak agonist (collagen, which activates platelet clotting via activation of the thromboxane (Roberts, McNicol, & Bose, 2004)) over 5 minutes. Platelet aggregometry in this study was measured by a clinical platelet aggregometer device (PAP-8E, Bio/Data Corp., Horsham, PA, USA), which works in much the same way as the RBC aggregometer (MA1, Myrenne, Roentgen, Germany) described in chapter 1, via measuring an increase in transmittance over time of a turbid solution of

suspended cells as they aggregate and sequester themselves from scattering the light path. Before measurement, concentration of platelets was equalized to a number below expected concentration from either method by adding platelet poor plasma (PPP). Since blood components were prepared from WB collected in CPD anticoagulant as is often the case in practice, calcium in the WB was chelated by citrate. However, since platelet aggregation relies on calcium, we modified the Pap-8e protocol to add $CaCl_2$ before aggregometry, in order to quench citrate calcium chelation. Particularly in the case of collagen activation, no platelet coagulation was observed until calcium was added. $CaCl_2$ was added to produce a final concentration of 1 mmol in the platelet rich plasma (PRP) just before addition of each agonist according to standard operating procedure of the aggregometer. Plasma total protein concentration was tested with the Pierce 660 nm Assay (Fisher Scientific, Pittsburg, PA), and clotting factor concentration was tested with sandwich enzyme linked immunosorbent assay (ELISA) kits (Affinity Biologicals, Hamilton, Ontario, Canada). Absorbance measurements were made using a plate reader (SpectraMax M5; Molecular Devices, Sunnyvale, CA). As standard blood banking procedure dictates, platelet units were stored for a week in a platelet agitator (Helmer Scientific, Noblesville, IN), and platelet aggregation was tracked every other day over 7 days, though almost no aggregation was observed past day 3 for any PRP unit using the methods in this study. pRBC was stored at 4°C for 6 weeks and EI, tested weekly, showed equal change over time for both centrifugation and passively separated RBCs. Plasma was frozen for storage and thawed to be assessed for protein concentrations using standard biochemical assays every 3 months for 6 months, but showed no change over time. As a result, time course data was not shown, and instead Table 4.1 shows values at

day 0 for each of these metrics, showing no significant difference in any of them between portions of WB units separated with centrifugation and corresponding units separated with the passive separation device.

4.4 Results

The flow through the MPC was ~3.2 ml/min under quasi constant pressure monitored by a pressure gauge, and produced a platelet concentrate of ~3x the concentration in the initial PRP supernatant resulting in a concentration of 873 ± 146 ($10^3/\mu L$) for a total of 87.5 ± 4.3% recovery of total platelets. Concentration of the platelets could be visualized in successive legs of the CIF device (Fig. 4.1d). When compared to the centrifugation-based method (96.2 ± 2.7% platelet recovery), a significantly lower percentage of platelets were recovered (t-test, $p = .002$), however average volume of the platelets retained by the MPC was larger than that of platelets in the initial WB and from centrifugation, indicating that the fraction of platelets missed by the MPC were likely to be cleared from circulation soon after transfusion anyways. Further, platelet activation as measured by P-selectin activation in flow cytometry (FACS Aria II; BD Biosciences, Franklin Lakes, NJ) was significantly lower in the passively separated platelet concentrate ($p = .005$), indicating that passively separated platelet quality was higher than that of platelets separated by high shear, high pressure centrifugation (Gifford et al., 2018). The total processing time was ~ 6 hours including the 2.5 hours of RBC sedimentation time that did not require monitoring.

All other RBC, platelet and plasma metrics showed no significant difference between the quality of components produced by either separation method. Table 4.1

summarizes EI at 3 and 30 Pa of the RBCs, primary and secondary aggregation of platelets due to TRAP, ADP and collagen agonists, and plasma protein and Factor VIII and Factor XI concentrations. Values are mean ± standard deviation (n = 6, † indicates n = 5 due to data acquisition failure).

Table 4.1: Selected measurements of red blood cell (RBC), platelet, and plasma quality after separation via conventional centrifugation vs. the passive microfluidic device

	Whole blood	Centrifugation	Passive separation
RBCs / pRBC unit			
Elongation Index [3 Pa]	0.38 ± 0.02	0.39 ± 0.01	0.39 ± 0.01
Elongation Index [30 Pa]	0.61 ± 0.01	0.61 ± 0.01	0.61 ± 0.01
Platelets / PC unit			
TRAP† (AUC)	-	17618 ± 615	18711 ± 1248
ADP† (AUC)	-	16477 ± 817	16853 ± 904
Collagen† (AUC)	-	68291 ± 3206	72083 ± 3577
Plasma / PPP unit			
Total Protein† [mg/mL]	-	48.84 ± 8.4	52.11 ± 13.6
Factor VIII [IU/mL]	-	1.36 ± 0.4	1.27 ± 0.4
Factor XI [IU/mL]	-	0.87 ± 0.2	0.87 ± 0.2

4.5 Discussion

We described a portable passive blood separation device made with affordable materials that performs as well as industrial centrifuge washing in terms of throughput and component quality, without requiring electricity. The driving pressure of the system, 10 Psi, can be easily attained by pressurizing the air spring to 40Psi with a hand pump, and was shown to remain at constant throughout the expression of the PRP through the MPC.

The results of this study not only validated the use of a more inexpensive, potentially electricity-free device for blood separation, but also demonstrated a common failure mode associated with platelet aggregometry, and the resulting difficulty of comparing results between studies given the wide range of anticoagulants used in blood collection. Reducing cost and increasing robustness of methods to quantify platelet aggregation could enable evaluation of platelet quality before discarding or transfusing this delicate product. Nevertheless, the passive separation device was shown to enrich larger, less activated platelets, with less free [Hb] and WBCs in the units, providing the potential of reducing adverse events associated with platelet transfusion.

4.6 Conclusions

The design of the device described in this study improves upon the three design constraints of desirability, viability, and feasibility over current technologies. The improved platelet component quality adds an aspect of desirability, whereas the simple, electricity-free, and affordable nature of the device promises to improve access through feasibility of blood banking technology to resource-limited setings. Finally, the customizable nature of the MPC CIF technology to enable enrichment of particles across a range of sizes and for a range of throughputs ensures viability of such a system, as it has also been used to extract lymphocytes from WB for improved T-cell expansion in cellular therapy, and less damaging leukoreduction of platelet units (Strachan, Xia, VÖRÖS, Gifford, & Shevkoplyas, 2019; Xia, Strachan, Gifford, & Shevkoplyas, 2016). These multiple modes of innovation indicate a well-designed product, and can improve access to vital medical technology.

CHAPTER 5 DEVELOPING AN ACCESSIBLE SCD DIAGNOSTIC ASSAY: A stable, distributable, low-cost, paper-based assay for SCD

5.1 Introduction

Sickle cell anemia (SCA) is genetic blood disorder that is particularly lethal in early childhood. Universal newborn screening programs and subsequent early treatment are known to drastically reduce under-5 SCA mortality such that they are cost effective to implement in regions with relatively high incidence of HbS inheritance (McGann et al., 2015). However, in resource-limited settings, cost and infrastructure constraints limit the effectiveness of laboratory-based SCA screening programs. To address this need our laboratory previously developed a low-cost, equipment-free, point-of-care, paper-based SCA test. Here, we improved the stability and performance of the test by replacing sodium hydrosulfite (HS), a key reducing agent in the hemoglobin solubility buffer which is not shelf stable, with sodium metabisulfite (MS). Additionally, the more stable formulation of the assay enabled the production of a test kit that could be affordably distributed, and stimulated the creation of open-source automated screening software for regulation and standardization of screening.

The MS formulation of the test was compared to the HS formulation in a laboratory setting by inexperienced users (n=3), to determine visual limit of detection (LOD), readout time, diagnostic accuracy, inter- and intra-observer agreement, and shelf life. The MS test was found to have a 10% sickle hemoglobin (HbS) LOD, 21 minute readout time, 97.3% sensitivity and 99.5% specificity for SCA, almost perfect inter- and intra-observer agreement, at least 24 weeks shelf stability at room temperature, and could

be packaged into a self-contained, distributable test kit comprised of off-the-shelf disposable components and food-grade reagents with a total cost of only $0.21 (USD), and included open source screening software with the ability to employ linear regression to improve automated diagnostic accuracy over time.

5.2 Background

As outlined in Chapter 1, sickle cell disease (SCD) is associated with significant lifelong morbidities and premature mortality (Modell & Darlison, 2008; Stuart & Nagel, 2004). This mutated β-globin allele results in the production of sickle hemoglobin (HbS), a form of hemoglobin (Hb) that polymerizes when deoxygenated, unlike normal adult hemoglobin (HbA). The polymerization of deoxy-HbS molecules into comparatively long, rigid fibers deforms the red blood cell (RBC) membrane and causes the characteristic 'sickled' shape of affected sickle RBCs. Sickle RBCs are markedly less deformable and more fragile than normal, healthy RBCs, which causes them to occlude blood vessels, cause chronic ischemia-reperfusion injury, and lyse frequently resulting in severe anemia, chronic painful episodes and predisposition to infection (Powars, Chan, Hiti, Ramicone, & Johnson, 2005; Rees et al., 2010).

When the allele coding for HbS is inherited heterozygously with the allele coding for HbA (i.e., genotype *HbAS*) it causes what is known as sickle cell trait (SCT) where both forms of Hb are produced and individuals are typically healthy, do not need medical intervention related to HbS and may have improved resistance to parasites such as *Plasmodium falciparum* (Powars et al., 2005; Rees et al., 2010). In Angola for example, the HbS allele is present in over 20% of the population, with about 98% of those carriers

having the allele heterozygously (McGann et al., 2013; Ware, 2013). However, when the HbS allele is inherited homozygously (i.e., genotype *HbSS*), it causes sickle cell anemia (SCA), a condition in which 40-100% of all Hb produced is HbS and individuals experience some of the most severe symptoms associated with SCD. Homozygous inheritance of the HbS allele and an allele coding for another non-HbS, aberrant form of Hb results in other, less common forms of SCD which have varying degrees of clinical severity (Piel, Hay, Gupta, Weatherall, & Williams, 2013; Weatherall, 2010). For the purposes of this study, we will focus mainly on the differentiation of SCA – the most common form of SCD – from SCT and normal, healthy individuals (i.e., genotype *HbAA*).

The mortality rate for SCA is the highest in the first five years of a child's life, as young children are prone to acute infections and anemic sequestration crises (Vichinsky, Hurst, Earles, Kleman, & Lubin, 1989). Improvements in survival rates for SCA over the last few decades have largely been due to earlier diagnosis and initiation of simple, inexpensive prophylaxis such as penicillin to combat opportunistic infections. Almost all children born in the United States and many other resource-rich countries are screened for SCA at birth as part of universal newborn screening programs that test for diseases and conditions where early initiation of treatment is crucial for survival and healthy, normal development (Platt et al., 1994). However due to cost and infrastructure limitations, this type of universal screening is oftentimes not feasible in the resource-limited settings where the incidence of HbS is highest – such as in sub-Saharan Africa, where approximately 80% of global individuals with SCA are born (Makani et al., 2011; Modell & Darlison, 2008; Rees et al., 2010). Nearly all children with SCA who are

diagnosed soon after birth and promptly given treatment survive into adulthood, while the mortality rates for undiagnosed (and therefore untreated) children in sub-Saharan Africa are estimated to be as high as 50-90% by the age of 5 years (Makani et al., 2011; Modell & Darlison, 2008).

The implementation of wide-spread screening and follow-up care for individuals with SCA has been predicted to potentially save the lives of up to 10 million children by year 2050 in the countries most affected by the disease (e.g., Nigeria, Angola, Democratic Republic of the Congo, India) (Piel et al., 2013). Though highly successful, most of the pilot screening programs in these settings have used conventional diagnostic methods such as high-performance liquid chromatography (HPLC) or isoelectric focusing electrophoresis (IEF) to identify SCA, both of which are relatively high-cost, technically complex and dependent on stable infrastructure (Head, Conroy, Jarvis, Phelan, & Bain, 2004; Jenkins & Ratnaike, 1999). The requirements and limitations of these conventional diagnostic methods (e.g., stable infrastructure, specialized equipment, trained personnel) result in screening being limited to those born in major health centers and prevent life-saving screening efforts from reaching more remote, less well-equipped community health outposts and those born out-of-hospital, thereby preventing screening programs from being truly universal (Cronin, Normand, Henthorn, Hickman, & Davies, 1998; Diallo & Tchernia, 2002; Jenkins & Ratnaike, 1999; Montagu, Yamey, Visconti, Harding, & Yoong, 2011).

In order to address these limitations, our research group recently developed a simple, equipment- and electricity free, paper-based test capable of differentiating normal (*HbAA*), SCT (*HbAS*) and SCA (*HbSS*) blood samples (N. Z. Piety et al., 2016; Piety,

Yang, Lezzar, George, & Shevkoplyas, 2015). The paper-based test was previously shown to be accurate (93% sensitivity, 94% specificity for differentiating SCA), low-cost ($0.07 in material and reagent costs), robust and easy to use (Angolan health workers proficient in performing test after one demonstration), and rapid (less than 30 minutes from start to readout) (N. Z. Piety et al., 2016).(N. Z. Piety et al., 2016) However, the previously developed version of the paper-based SCA screening test required the use of a reducing agent – sodium hydrosulfite (HS) – which quickly becomes oxidized in aqueous solutions (especially when exposed to oxygen) (Piety, George, et al., 2017; Piety et al., 2015) . The relative instability and volatility of HS made shipping and long-term storage of the previous version of the test impractical (Piety, George, et al., 2017; N. Z. Piety et al., 2016). Here we describe how replacing HS with a higher concentration of sodium metabisulfite (MS), addressed the limitations of the previously developed test without negatively impacting test performance. The principal conclusions of this study were that, compared to the previous test, the novel MS formulation of the paper-based SCA screening test had a superior limit of detection (LOD; 10% HbS vs. 20% HbS), faster readout time (21 minutes vs. 30 minutes), better diagnostic performance (97.3% sensitivity, 99.5% specificity for differentiating SCA), high intra- and inter-observer agreement ($\kappa = 0.93$, $\kappa = 0.87$ respectively), longer shelf stability at room temperature (at least 24 weeks vs. 1 week for aqueous storage conditions), and could be packaged into a self-contained, distributable test kit with a total cost of only $0.21 (USD).

5.3 Materials and Methods

The study protocol was approved by University of Houston and Baylor College of Medicine institutional review boards. Venous whole blood samples were obtained with written informed consent in 4mL Vacutainer tubes (K_2EDTA, BD, Franklin Lakes, NJ) from healthy, normal volunteers and patients of the Texas Children's Hematology Centers (Houston, TX). Blood samples were stored at 4°C and used within 2 months following collection. The sickle hemoglobin (HbS) content of blood samples from individuals with sickle cell trait (SCT) or sickle cell anemia (SCA) was quantified with high-performance liquid chromatography (HPLC; Primus Ultra Variant, Trinity Biotech, Wicklow, Ireland). Healthy volunteers were assumed to have 0% HbS. Hematocrit (Hct) and hemoglobin concentration ([Hb]) were measured with an automated hematology analyzer (Medonic, Boule Medical AB, Spånga, Sweden), and ABO-RhD blood type was determined using blood type test kits (EldonCard, Eldon Biologicals, Gentofte, Denmark).

Artificially reconstituted blood samples with specific Hct (22% – a physiological Hct for sickle cell anemia) and HbS concentrations (0, 10, 20, 40 and 80% HbS) were made by combining blood samples from normal (*HbAA*) and SCT or SCA (*HbSS*) individuals. Sample Hct was adjusted via centrifugation at 500×g for 10 minutes (Beckman Microfuge 22R, Beckman Coulter, Brea, CA) and reconstitution of red blood cell (RBC) sediment in autologous plasma. The type-matched and Hct-matched *HbAA* with *HbSS* blood were then combined at various ratios according to the following equation:

$$\%\boldsymbol{HbS} = \frac{([\boldsymbol{Hb}]_{\boldsymbol{HbSS}})(\boldsymbol{V}_{\boldsymbol{HbSS}})(\%\boldsymbol{HbS}_{\boldsymbol{HbSS}})}{([\boldsymbol{Hb}]_{\boldsymbol{HbSS}})(\boldsymbol{V}_{\boldsymbol{HbSS}}) + ([\boldsymbol{Hb}]_{\boldsymbol{HbAA}})(\boldsymbol{V}_{\boldsymbol{HbAA}})}, \quad (5.1)$$

where V is volume, subscripted *HbSS* refers to samples from patients with SCT or SCA, and the subscripted *HbAA* refers to samples from healthy, normal volunteers.

For this study, venous blood samples were collected as described above. For the self-contained SCA screening test kit, capillary blood can be collected via finger or heel prick. Capillary and venous blood have both been shown to produce comparable diagnostic results for the assay. (Piety, George, et al., 2017; N. Z. Piety et al., 2016; Piety et al., 2015) Additionally, the HS version of the paper-based SCA screening test has been previously shown to be insensitive to variations in Hct and associated variations in [Hb] within the physiological range (N. Z. Piety et al., 2016; Piety et al., 2015). Physiological concentrations of fetal hemoglobin (HbF) amongst infants, adults and hydroxyurea patients were also shown to not impact test performance (N. Z. Piety et al., 2016; Piety et al., 2015).(N. Z. Piety et al., 2016; Piety et al., 2015) Blood samples used to perform the study of test kit stability were replaced with new samples – with the same Hcts and HbS concentrations – after 20 days of storage at 4°C in order to counteract any potential effects due to storage-based RBC and/or Hb deterioration (i.e., storage lesion).

The hemoglobin solubility buffers compared in this study each consisted of three components: saponin (Sigma-Aldrich, St. Louis, MO), a reducing agent, and a concentrated phosphate buffer (Piety, George, et al., 2017; N. Z. Piety et al., 2016; Piety et al., 2015; Yang et al., 2013). Potassium phosphate buffer at 2.49M was made by dissolving solid 1.24M (169 g/L) monobasic and 1.25M (217 g/L) dibasic potassium phosphate (Sigma-Aldrich, St. Louis, MO) in deionized water. Saponin (4g/L) was added to irreversibly lyse RBCs by creating holes in the lipid bilayer through sequestration of cholesterol, thereby releasing hemoglobin into the buffer (N. Z. Piety et al., 2016). The

reducing agent – either HS (30g/L; 3% w/v) or MS (100, 150 or 200 g/L; 10, 15, 20% w/v) – then converts the released Hb into deoxy-Hb, which is either soluble (e.g., deoxy-HbA, deoxy-HbF, deoxy-HbC) or insoluble (deoxy-HbS) in the phosphate buffer (Piety, George, et al., 2017; N. Z. Piety et al., 2016; Piety et al., 2015; Yang et al., 2013). Additionally, buffer consisting of food-grade MS (Duda Energy LLC, Decatur, AL) and food-grade saponin (Ingredion, Westchester, IL) was made using the same concentrations as above.

The stability of the MS and HS solubility buffers was compared under two storage conditions: 'wet' and 'dry'. Dry refers to the saponin and MS or HS being stored in dry powdered form and mixed with concentrated phosphate buffer on the day of the experiment, while wet refers to dry reagents premixed with concentrated phosphate buffer and stored until the day of the experiment. Individual sets of reagents were stored within heat-sealed polyethylene-lined 2mm thick foil pouches (Xin Jiu Technology, Taoyuan, Taiwan). The reagents were stored and tested at room temperature (18-26ºC, 30-50% relative humidity). The buffers were stored between 1 and 166 days before use. Results from test performed using stored buffers were compared against those for reagents prepared on the same day of the experiment from dry powdered ingredients stored in their original containers.

The design and operation of the paper-based SCA screening test have been described in detail previously (Piety, George, et al., 2017; N. Z. Piety et al., 2016; Piety et al., 2015; Yang et al., 2013). Figure 5.1a shows a photograph of the test kit with all components necessary to perform the assay: (i) patterned chromatography paper; (ii) reagent tube containing reagents; (iii) reagent dropper; (iv) blood dropper; and (v) foil

pouch. Briefly, 20 µl of whole blood is collected and mixed with Hb solubility buffer by inversion, the blood and buffer mixture is allowed to incubate at room temperature for 10 minutes, 20 µL of blood is then dropped onto chromatography paper (Whatman Chr 1, Sigma-Aldrich, St. Louis, MO) and allowed to dry for up to 25 minutes (Fig. 5.1b). Insoluble deoxy-HbS polymers, if present, become entangled in the paper substrate and form a dark red spot in the center of the stain, while soluble forms of Hb wick laterally through the paper pores and produce a more diffuse pink ring (Fig. 5.1c). A limit of detection (LOD) is evident due to the contrast between the center circle and the outer ring, and is used to distinguish samples by HbS concentration: typical HbS concentration ranges for adults and children older than six months of age with different genotypes (healthy—*HbAA*; sickle cell trait (SCT)—*HbAS*; SCA—*HbSS*) are marked below the stains.

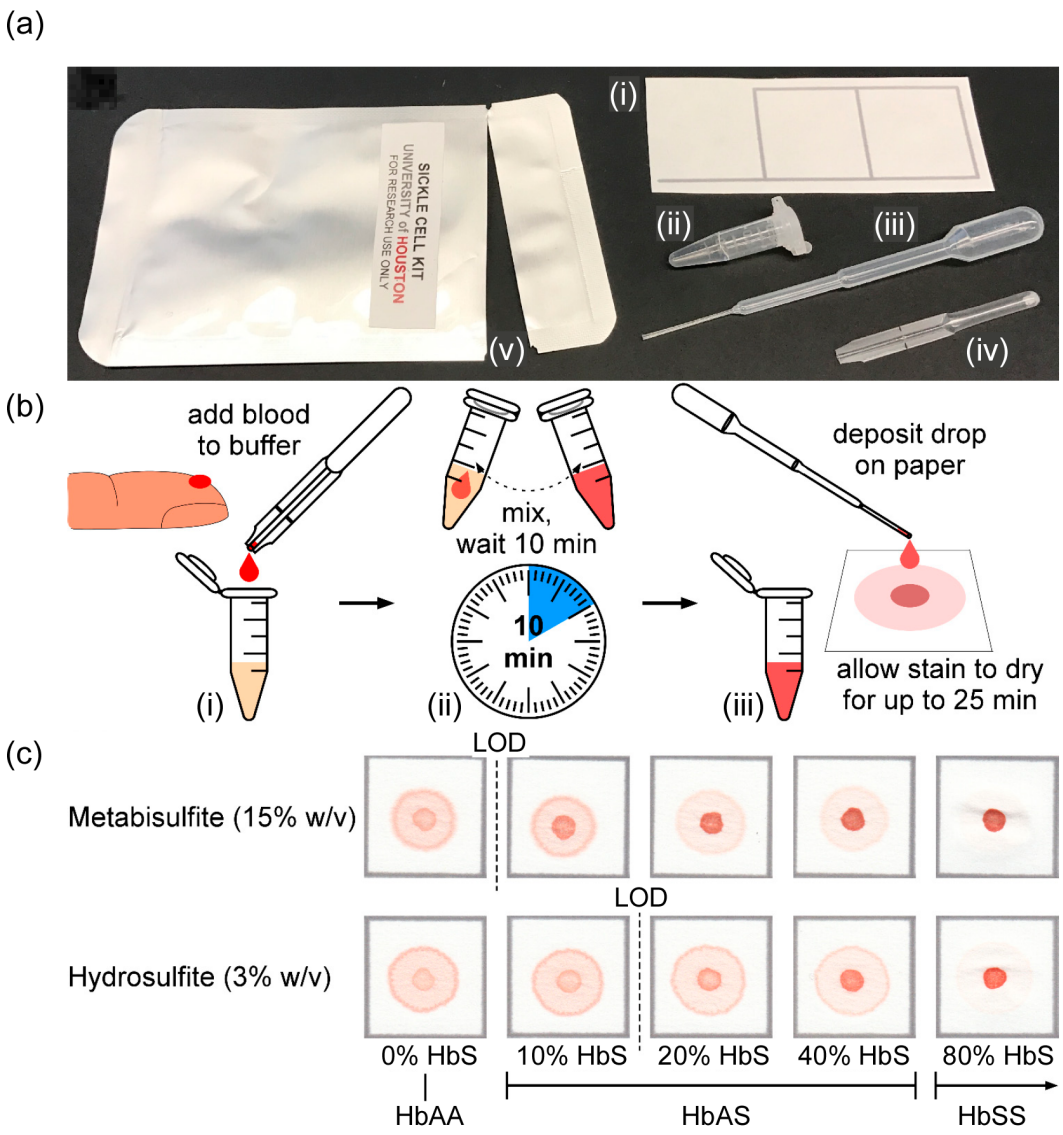

Figure 5.1: Overview of the distributable paper-based sickle cell anemia (SCA) diagnostic test kit.

Blood stain patterns were interpreted visually by eye and/or digitized using a portable scanner (CanoScan LiDE110, Canon USA, Lake Success, NY) and quantified using a custom image analysis algorithm implemented in MATLAB (The Math Works, Natick, MA). Inexperienced users (n = 3) with little to no past experience performing and interpreting the paper-based test were provided with a set of representative images of blood stain patterns resulting from both the MS and HS versions of the test performed

using normal, SCT and SCA blood samples (using Hb solubility buffer prepared on the same day of the experiment from dry powdered ingredients stored in their original containers). The previously described 'S-index' – defined as the quotient of the mean red color intensity of pixels in the center spot area of the blood stain and the mean red color intensity of pixels in the ring area of the blood stain (red color intensity = 255-B, where B is the Blue channel of the RGB values for the digitized image) – was used to quantify the differences between blood stain patterns produced by different formulations of the test (Piety et al., 2015).

Test performance metrics were calculated as: Sensitivity = TP / (TP + FN); specificity = TN / (FP + TN); positive predictive value (PPV) = TP / (TP + FP); negative predictive value (NPV) = TN / (TN + FN); and accuracy = (TP + TN) / (TP + FP + TN + FN), where TP = true positive, FP = false positive, TN = true negative and FN = false negative. Fleiss' kappa statistic was used to assess intra- and inter-operator agreement for visual scoring of blood stains (Fleiss, 1971; Roila et al., 1991). Mean, standard deviation, p-values, and confusion matrices were calculated using built-in functions in MATLAB (The Math Works, Natick, MA).

5.4 Results

We hypothesized that we could improve the stability and performance of our previously developed paper-based screening test for SCA by replacing a key component of the Hb solubility buffer, sodium hydrosulfite (HS), with sodium metabisulfite (MS), a chemically stable food additive. The design and operation of the HS version of the test has previously been described in detail (Piety, George, et al., 2017; N. Z. Piety et al.,

2016; Piety et al., 2015; Yang et al., 2013). The concentration of MS used to replace HS was determined by comparing the previously described S-index – defined as the quotient of the red color intensities of the center area (proportional to amount of HbS) and the ring area (proportional to other forms of Hb) of the blood stain – for buffer formulations with 10, 15 and 20% MS (w/v) to the S-index for the previously developed buffer formulation with 3% HS (w/v) for a set of samples with HbS concentrations from 0 to 40% HbS (Piety et al., 2015). 15% MS (w/v) was chosen as the final formulation for the Hb solubility buffer because it produced the greatest difference in S-Index between 0 and 20% HbS and the most gradual change in S-Index over the range of 20-40% HbS (data not shown). The Hb solubility buffer containing 15% MS (w/v) was used to perform all experiments described in this study.

The limit of detection (LOD) for this test is defined as the lowest HbS concentration in a sample that will produce a blood stain in paper which is visually distinguishable from characteristic blood stains for samples without any HbS. The previously developed HS test is capable of identifying SCA in adults and children older than 6 months of age and has a reported LOD of ~15% HbS (N. Z. Piety et al., 2016).(N. Z. Piety et al., 2016) To determine the LOD of the MS version of the test, inexperienced users (n = 3) were asked to visually score a set of images of blood stains in paper (n = 370) produced by the MS formulation of the test as either HbS-negative (HbS = 0%) or HbS-positive (HbS > 0%). The inexperienced users were able to correctly score 820 of the 888 blood stain images with ≥10% HbS (92.3%) as having some HbS and 220 of the 222 blood stain images with <10% HbS (99.1%) as having no HbS. These results suggest

that, when evaluated visually by an inexperienced user, the LOD of the MS formulation of the paper-based SCA screening test was ~10% HbS.

After the mixture of blood and Hb solubility buffer is deposited on chromatography paper, it takes approximately 25 minutes for the blood stain to become completely dry. However, accurate visual diagnoses can be made from blood stain patterns before they are completely dry. Inexperienced users (n = 3) were asked to visually score blood stains for unknown samples every minute for 25 minutes as the stains dried following deposition of the mixture onto paper. Samples with 0% HbS (normal) were correctly scored by all three users after 7 minutes of drying time, samples with HbS levels characteristic of SCT (10-40% HbS) were correctly scored by all users after 11 minutes, and samples with HbS levels characteristic of SCA (>40% HbS) could be scored correctly after 1 minute. These results suggest that the paper-based SCA screening test can be performed and interpreted within 21 minutes (10 minutes preparation and incubation + 11 minutes drying before readout).

To determine the performance of the MS version of the test, inexperienced users (n = 3) were asked to visually score a set of images of blood stains in paper (n = 185) produced by the MS version of the test as either normal (*HbAA*; characteristic HbS = 0%), SCT (*HbAS*; characteristic HbS = 10-40%) or SCA (*HbSS*; characteristic HbS >40%). Figure 5.2a,b shows the aggregate confusion matrices of the visual diagnoses made by the three inexperienced users with both the MS and HS versions of the paper-based test. Using the MS formulation inexperienced users could visually distinguish between blood samples with no HbS and blood samples with ≥10% HbS (i.e., *HbAA* vs. *HbAS* and *HbSS*) with 92.8% sensitivity, 100% specificity, 100% positive predictive

value (PPV), 77.6% negative predictive value (NPV) and 94.2% overall diagnostic accuracy (Fig. 2a). Users could also distinguish between blood samples with ≥80% HbS (characteristic of SCA) from blood samples with <80% HbS (characteristic of normal and SCT) (i.e., *HbSS* vs. *HbAA* and *HbAS*) with 97.3% sensitivity, 99.5% specificity, 98.2% PPV, 99.3% NPV and 99.1% overall diagnostic accuracy (Fig. 5.2a).

When the same three inexperienced users were asked to score blood stains in paper produced by the previously developed HS formulation of the test (n = 143), they could visually distinguish between blood samples with no HbS and blood samples with ≥20% HbS (i.e., *HbAA* vs. *HbAS* and *HbSS*) with 61.2% sensitivity, 100% specificity, 100% PPV, 49.2% NPV and 71.8% overall diagnostic accuracy (Fig. 5.2b). Users could also distinguish between blood samples with ≥80% HbS (characteristic of SCA) from blood samples with <80% HbS (characteristic of normal and SCT) (i.e., *HbSS* vs. *HbAA* and *HbAS*) with 76.9% sensitivity, 100% specificity, 100% PPV, 95.1% NPV and 95.8% overall diagnostic accuracy (Fig. 5.2b).

Scores from HS (n = 125) and MS (n = 185) tests from one user were also tabulated to produce an ROC curve (Figure 5.2c). The LOD for the HS and MS tests was determined by changing the threshold %HbS at which we expected detection (scored as *HbAS* or *HbSS*, as opposed to *HbAA*), and integrating under the resulting ROC curve to select the %HbS that produced the largest AUC. Highest AUCs for HS were at 20%HbS, with AUCs for discriminating *HbAA* from *HbAS*/*HbSS* samples of 0.986 (square) and *HbAA*/*HbAS* from *HbSS* of 0.987 (triangle), and highest AUCs for MS were at 10%HbS, with higher AUCs for discriminating *HbAA* from *HbAS*/*HbSS* of 0.989 (diamond), and *HbAA*/*HbAS* from *HbSS* of 0.996 (circle).

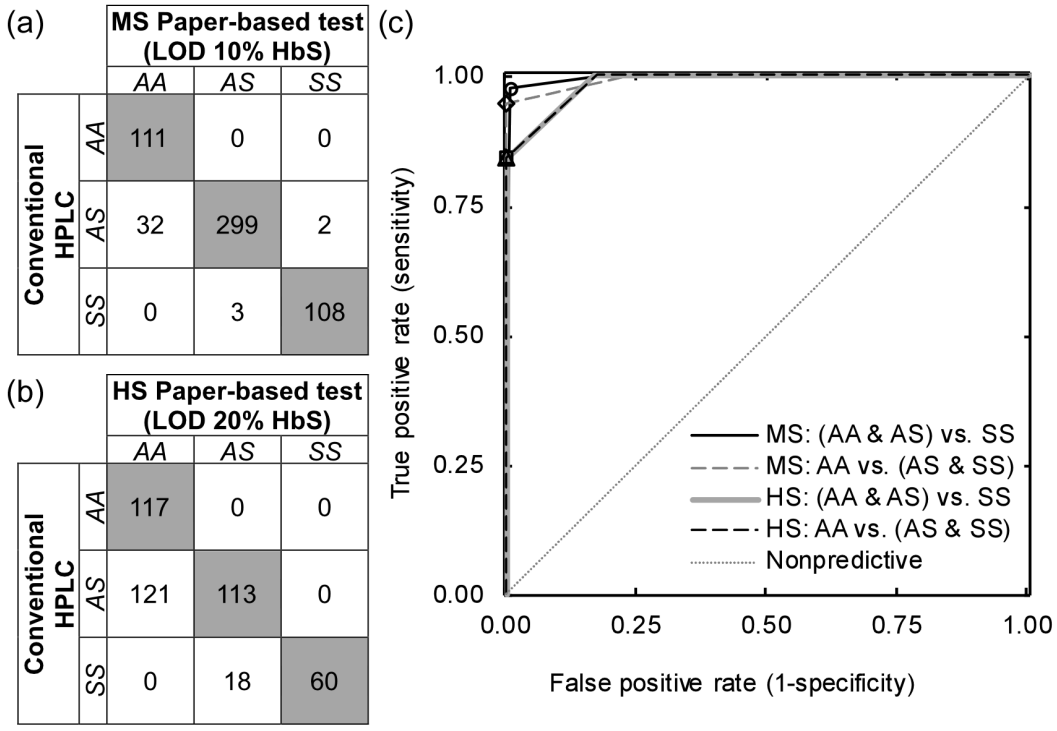

Figure 5.2: Diagnostic accuracy of the paper-based sickle cell anemia (SCA) screening test kit.

The Fleiss' kappa statistical measure (κ) for assessing intra-observer agreement of the scoring of blood stains in paper (n = 370) produced by the MS version of the test was $\kappa = 0.93 \pm 0.04$ (individual scores: 0.88, 0.93 and 0.97), which suggests that there was almost perfect self-consistency for each of the three inexperienced test users. The Fleiss' kappa statistical measure for assessing inter-observer agreement for the MS version of the test was $\kappa = 0.87$, which suggests that there was almost perfect agreement between the three inexperienced test users. When the same three inexperienced users were asked to score blood stains in paper (n = 286) produced by the previously developed HS formulation of the test, $\kappa = 0.85 \pm 0.09$ (individual scores: 0.72, 0.88 and 0.94) for intra-observer agreement and $\kappa = 0.75$ for inter-observer agreement. These results suggest that there is a very high level of intra- and inter-observer agreement for the HS version of the

test, and that both intra- and inter-observer agreement are comparable for the MS version of the test.

Figure 5.3 shows the stability of the reagents comprising the Hb solubility buffer for the MS and HS formulations of the paper-based test when stored under dry (MS powder stored separately from aqueous buffer components) or wet (MS powder mixed with aqueous buffer components before storage) conditions over the course of 24 weeks. Reagents were considered to be stable as long as the difference in S-index – defined as quotient of the red color intensities of the center area and ring area of the blood stain – between samples with 0% HbS and samples with HbS concentrations greater than or equal to the LOD of tests performed using fresh reagents (i.e., ≥10% HbS for MS and ≥20% HbS for HS) remained statistically significant ($p < 0.05$).

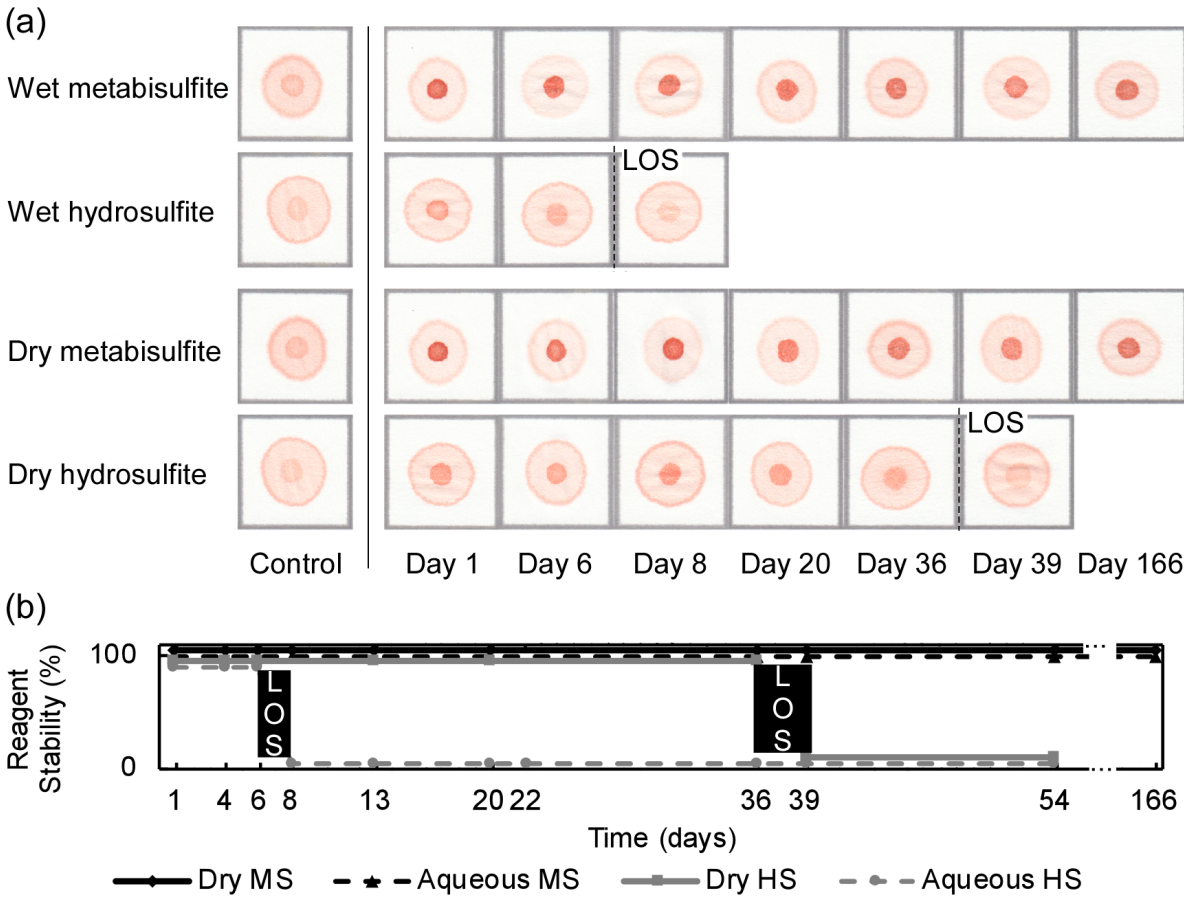

Figure 5.3: Stability of the paper-based sickle cell anemia (SCA) screening kit reagents under wet (sodium metabilsuflite (MS) or hydrosulfite (HS) dissolved in aqueous buffer before storage) or dry (sodium MS or HS stored separately from aqueous buffer) storage.

The MS formulation maintained stability over the course of all 24 weeks studied regardless of whether MS was stored under dry or wet conditions. The difference between blood stain patterns for samples with 0% HbS and ≥10% HbS was still visually obvious and statistically significant ($p < 0.05$) at the end of the >24-week study period (Fig. 5.3). When stored under dry conditions the HS formulation remained 100% stable until day 36 (~5 weeks) of the study period, after which it lost all activity – i.e., the difference in blood stain patterns for samples with 0% HbS and ≥20% HbS was not visually obvious or statistically significant ($p > 0.05$). When stored under wet conditions

the HS formulation remained 100% stable until day 6 (~1 week) of the study period, after which it lost all activity (Fig. 5.3). These results suggest that, regardless of whether MS is stored in dry or wet form, the MS version of the test has a shelf life which is (at the least) ~5 times as long as the shelf life for a dry HS version of the test and ~24 times as long as the shelf life for a wet HS version of the test. Additional testing showed that when stored under wet conditions the MS formulation remained 100% stable for >1 week when stored at 62ºC (an upper bound on hot temperatures reached in desert climates (Hickcox, 1986)).

Despite high inter- and intra-observer agreement scores, given the design of this assay for resource limited settings, to improve the likelihood of expanding quantification capability of the assay for monitoring %HbS, for example in response to treatment, an open-source classification application was written in Python (Appendix B) roughly based on a previous quantification algorithm written in MatLab (The Math Works, Natick, MA) (Piety et al., 2015). Functionality and performance of the application is described in Figure 5.4, showing a schematic of centroid identification, performed automatically with binary image processing in the Python program, and calculation of signal intensity over the stain (Fig. 5.4a, reprinted with permission from (Piety et al., 2015)), signals generated from the 8 processed stain scans (Fig 5.4b), and the 100% classification accuracy of 8 different stains using thresholds generated from analysis of the signals of the 25 training stains (Fig. 5.4c). The signals shown in Figure 5.4b plotted the 'S-Index' as the radius of the center circle grew to meet the edge of the scan. The peak in this signal was the point at which the center lined up with the experimental center ring of the stain (R_{center}), which was correlated to the percent HbS measured by high performance liquid chromatography (HPLC; Primus Ultra Variant, Trinity Biotech, Wicklow, Ireland) of 8 test samples for

confirming diagnosis (Fig. 5.4c). Such an application can easily be expanded to collect epidemiological information, use learning algorithms to improve as more data comes in, or even assist in remote medicine programs.

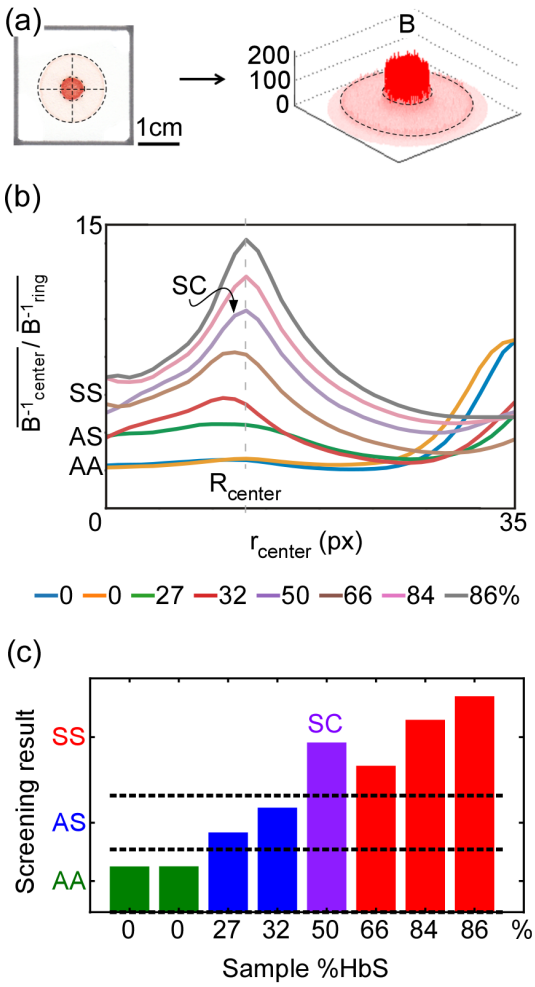

Figure 5.4: Software classification of scanned (CanoScan LiDE110, Canon USA, Lake Success, NY, USA) images from the metabisulfite (MS) version of the test.

As was shown with the HS formulation of the assay (Piety et al., 2015), the stain color contrast, calculated as the ratio of the mean of the inverse of the blue channel pixel intensity (255 minus blue channel intensity was used as a surrogate for oversaturated red channel intensity) of the inner circle to that of the outer ring of the MS formulation of the

assay, showed positive correlation with the %HbS as measured by HPLC (Figure 5.5a) even with varying HCTs or amounts of HbC or HbF in the sample (Figure 5.5b). Squared Pearson Correlation Coefficients for the HS and MS test were nearly identical. Bland-Altman comparison for paired and replicated data from the HS and MS assays showed similar accuracy of the MS test to the HS test for predicting %HbS calculated by HPLC (Fig. 5.6a,b for reconstituted and real samples using the MS test, and Fig. 5.6c,d for the HS test), and an ~20% HbS range containing 95% of predictions by the HS test of the MS test %HbS and vice-versa (Fig. 5.5c,d). The difference between %HbS calculated by either test was centered around ~0% HbS, but both tests display proportional bias, with the difference diverging more from 0 for higher %HbS samples.

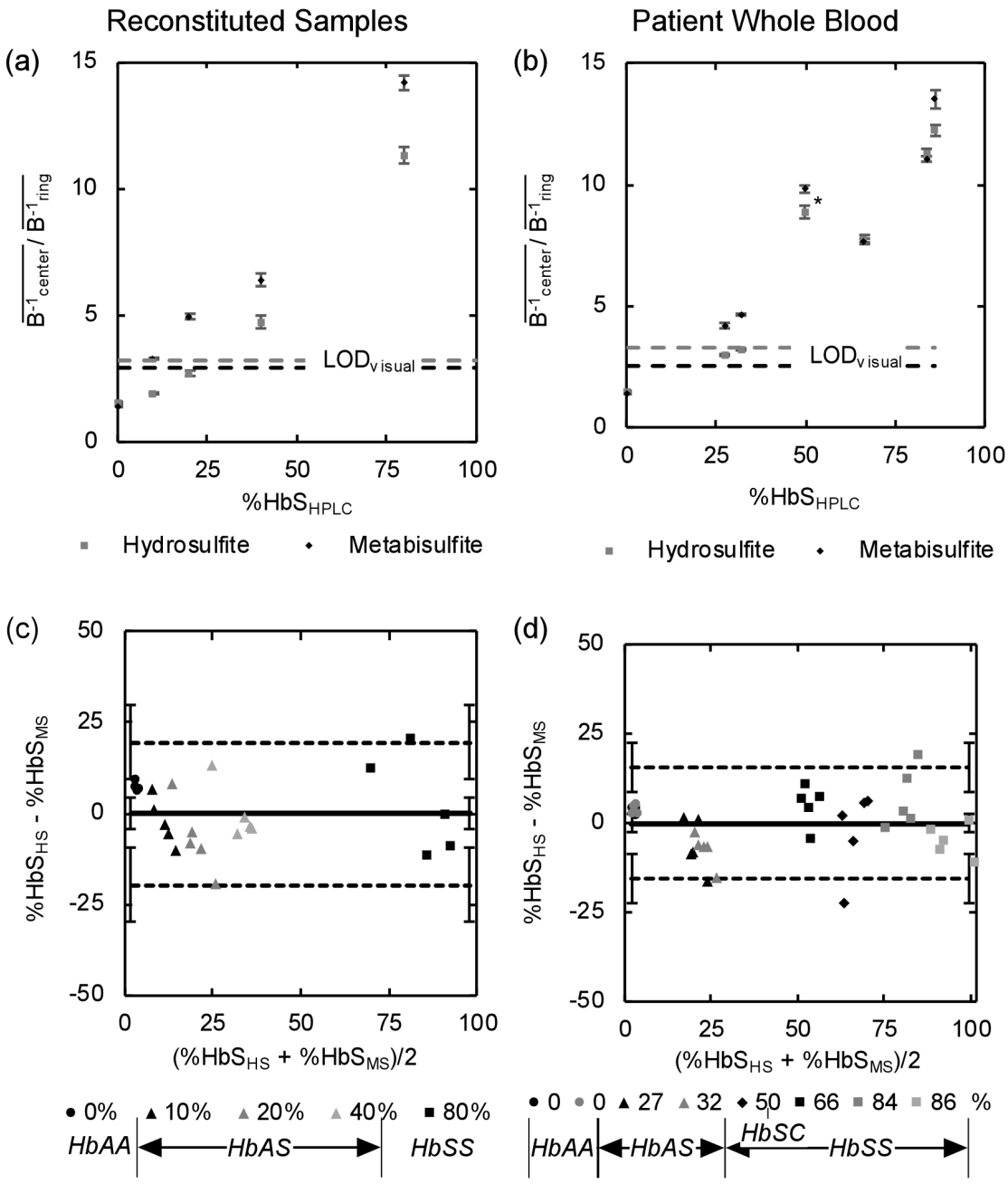

Figure 5.5: Comparison of hysdrosulfite (HS) and metabisulfite (MS) -based tests at quantifying %HbS of reconstituted samples used for training and real patient samples used for testing.

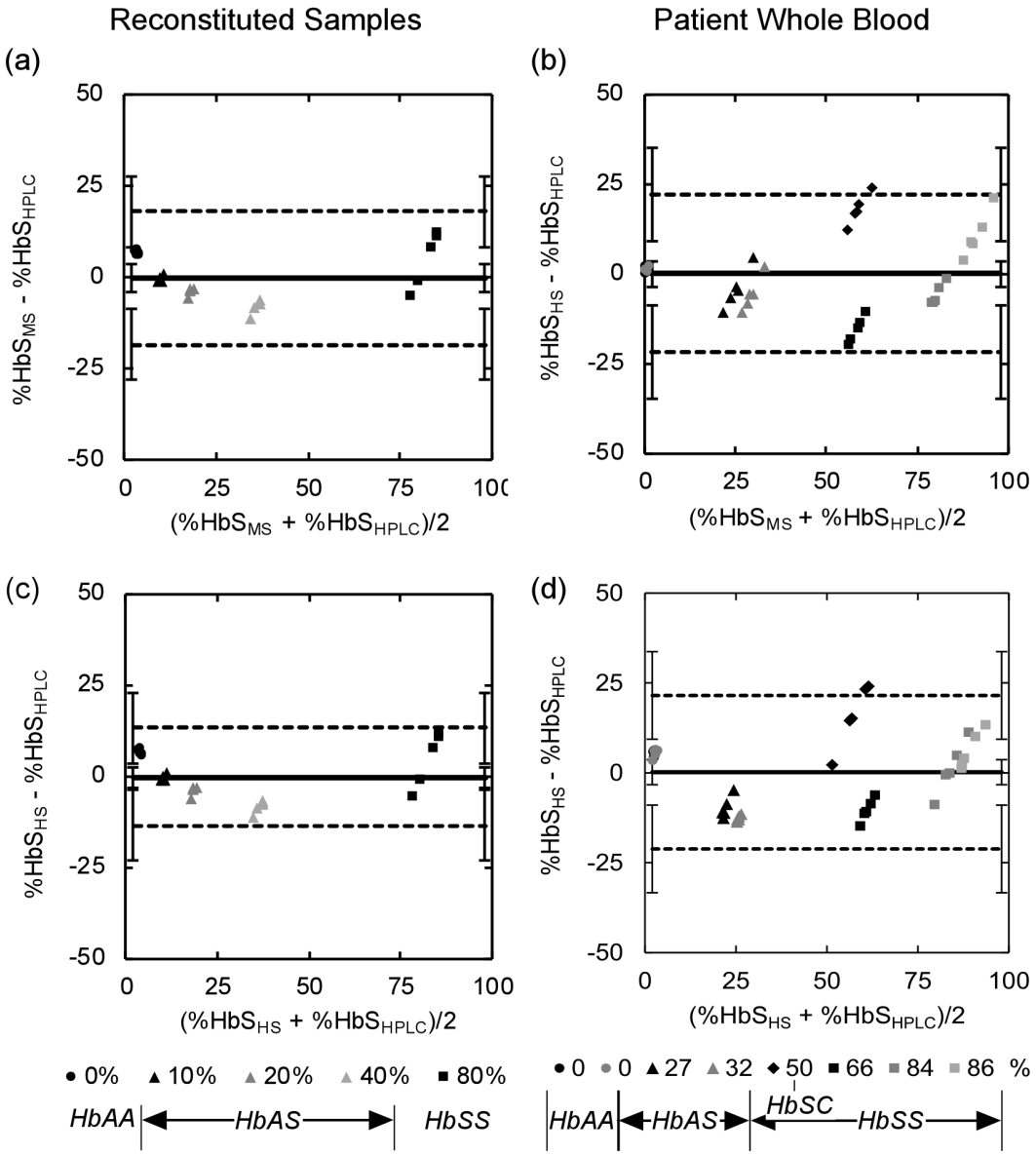

Figure 5.6: Results of Bland-Altman analysis comparing (a,b) the metabisulfite (MS) and (b,c) the hydrosulfite (HS) -based test with gold-standard data from high performance liquid chromatography (HPLC; Primus Ultra Variant, Trinity Biotech, Wicklow, Ireland).

A self-contained, distributable kit containing all reagents and materials necessary to perform the paper-based SCA screening test as described above was assembled using the following commercially available, off-the-shelf components: blood dropper (Microsafe 20 µL, Safe-Tec, Ivyland, PA), reagent tube (0.5 mL microcentrifuge tube,

Sigma-Aldrich, St. Louis, MO), reagent dropper (Disposable Graduated Transfer Pipet, VWR, Radnor, PA), chromatography paper (Whatman Chr 1, Sigma-Aldrich, St. Louis, MO), and foil polyethylene-lined pouch (Xin Jiu Technology, Taoyuan, Taiwan) (Fig. 5.1a). The key reagents used in this test kit were food-grade: sodium metabisulfite (Duda Energy, Decatur, AL) and saponin (Ingredion, Westchester, IL). Table 5.1 shows a cost breakdown for the reagents and materials comprising the self-contained, distributable paper-based SCA screening test kit. The total cost of all materials, reagents and packaging necessary to perform the paper-based SCA screening test using this kit was $0.21 (USD).

Table 5.1: Detailed cost breakdown of the paper-based sickle cell anemia (SCA) screening test kit with off-the-shelf components

Component	Cost per test (USD)
Foil Pouch	$0.02
Reagent dropper	$0.05
Blood dropper	$0.08
Chromatography paper	$0.01
Reagent tube	$0.03
Food grade reagents	$0.02
Total	$0.21

5.5 Discussion

Universal screening for SCA using laboratory-based methods (e.g., IEF, HPLC) is currently unfeasible in many resource-limited countries because of the prohibitively the high cost and lack of access to the technical infrastructure required to support such conventional testing. The advent of a simple, stable, equipment-free, visually interpreted and inexpensive screening test for SCA could greatly improve the survival rate of the

hundreds of thousands born with the disease each year, by enabling earlier initiation of simple and effective prophylactic care. The point-of-care screening technology described in this study has the potential to significantly decrease the cost and technical complexity of implementing universal screening programs in resource-limited regions where SCA has the highest incidence (Piel et al., 2013).

Recently multiple research groups have developed screening tests for sickle cell disease intended for use in resource-limited settings (Knowlton et al., 2015; Kumar, Chunda-Liyoka, et al., 2014a; McGann, Schaefer, Paniagua, Howard, & Ware, 2016). Some of the most promising emerging technologies include an antibody-based lateral flow assay that can detect HbS, HbA and HbC and an aqueous multiphase system used to separate dense sickle RBCs from healthy RBC populations with lower density (Kumar, Chunda-Liyoka, et al., 2014a; McGann et al., 2016). However, none of the current or developing tests adequately address all of the unique design requirements necessary to create a test which can be distributed, stored, performed and interpreted in resource-limited settings. For example, antibody-based tests are notoriously prone to stability and reproducibility issues when taken outside the laboratory, since antibodies generally denature above 37°C (mammalian body temperature) and are rarely specific (nonspecific antibodies may bind unintended antigens to produce a false positive signal) (McGann et al., 2016). However, the antibody-based SCD assay is simple to use, has shown >98% sensitivity and specificity in a laboratory setting for identifying *HbSS* blood, can accurately determine the presence of HbC (100% sensitivity and specificity), has operated successfully in high temperature settings (~30°C), has detected the low levels of HbS present in neonates (reported LOD of 2% HbS), and has potential to be very

effective at identifying other non-HbS hemoglobin variants. (McGann et al., 2016; Nguyen-Khoa et al., 2018; Segbena et al., 2018) As a result, the antibody-based SCD assay is most appropriate for situations where high genotypic resolution (i.e., the ability to specifically identify different SCD genotypes) is needed, but may be constrained from a cost and long-term stability perspective. The density based test, on the other hand, is highly sensitive to changes in reagent properties (e.g., change in density due to evaporation) and is not equipment- and electricity-free (i.e., requires car-battery powered centrifuge) (Kumar, Chunda-Liyoka, et al., 2014a).(Kumar, Chunda-Liyoka, et al., 2014b) The complexity of the density based test, and its sensitivity to comorbidities and other factors that influence RBC density, such as high amounts of HbF in newborns, resulted in lower sensitivity (86%) and specificity (60%) for identifying *HbSS* blood in resource-limited settings in Zambia (Kumar, Chunda-Liyoka, et al., 2014a). Furthermore, the density-based test has not been able to distinguish *HbAS* from *HbAA* (Kumar, Chunda-Liyoka, et al., 2014a; Kumar, Patton, et al., 2014). As such, none of the technologies currently on the market or in public development fully address the unmet need for a truly simple, stable and low-cost SCA screening test.

Our research laboratory has previously attempted to meet this need by developing and validating a paper-based SCA screening test capable of sensitive and specific differentiation of SCA from SCT and normal individuals in adults and children older than 6 months of age (N. Z. Piety et al., 2016; Yang et al., 2013). However, the Hb solubility buffer on which the previously developed test is based utilized a reducing agent – sodium hydrosulfite (HS) – which is expensive to ship and difficult to store due to its combustibility as a solid (Hazmat Class 4.2 – spontaneously combustible) and fast

oxidation in aqueous solutions ($t_{1/2}$ < 1 day at 25°C) (Luo, Ren, Shen, Liang, & Zhang, 2017). Here we presented the development and characterization of an alternative formulation of the Hb solubility buffer that eliminates the need for HS via substitution of an optimized concentration of sodium metabisulfite (MS) – a common preservative used in the food, textile and photography industries. MS is approximately half the price of sodium hydrosulfite when purchased commercially, is not a regulated substance (i.e., does not need to be shipped as hazardous goods), and is stable for up to a year as a solid at room temperature and at least ~6 months in solution with exposure to oxygen (Malanchuk, 1971).

The MS formulation of the paper-based SCA screening test described here successfully addresses many of the technical and logistical problems of the conventional approaches described above as well as the limitations of the previously developed HS formulation. Firstly, the use of MS instead of HS increased the shelf-life of the aqueous Hb solubility buffer by up to ~24x (Fig. 5.3), thus allowing for the packaging of a distributable kit containing premade buffer with a reasonably long shelf-life. The MS formulation maintained stability over the course of a 24 week period regardless of storage under dry or wet conditions – i.e., the difference in blood stain pattern between samples with 0% HbS and ≥10% (the LOD for MS tests performed using fresh reagents) HbS was still visually obvious and statistically significant ($p < 0.05$) at the end of the study period (Fig. 5.3). In contrast, the HS formulation only remained stable for ~5 weeks under dry conditions and ~1 week under wet conditions (Fig. 5.3). Additional experiments showed that the MS formulation of the test remained stable for at least one week when stored under wet conditions at 62ºC (an upper bound on hot temperatures reached in desert

climates on Earth (Hickcox, 1986)). The improved stability and storage capability of the sodium metabisulfite-based assay will be crucial for the expansion of SCA screening programs in regions without established supply chains and clinical facilities.

Secondly, in addition to improving the stability of the paper-based SCA test, the substitution of MS for HS improved the LOD of the assay by 2-fold, allowing for the detection of as little as 10% HbS in a blood sample, compared to 15% HbS with HS. Inexperienced users were able to visually differentiate SCA from normal or SCT samples with 97.3% sensitivity, 99.5% specificity and almost perfect agreement between scorers (Fig. 5.2a). In comparison, when using the HS test, users were only able to visually differentiate SCA with 76.9% sensitivity and 100% specificity (Fig. 5.2b). Given the higher concentration of metabisulfite used to achieve blood stain color intensities similar to the HS test, this improvement in LOD could be due to the increase in Hb solubility buffer osmolality, which causes more insoluble HbS to precipitate out of the solution and form a darker stain center spot on the paper (Piety et al., 2015). An alternate explanation for the improvement in LOD could be that MS deoxygenates HbS more slowly than HS, potentially allowing the formation of larger HbS polymers which increase clogging of HbS aggregates within the chromatography paper to form a darker stain center spot (Horiuchi, Ballas, & Asakura, 1988). This improvement in signal detection is an important development for screening young children, who produce less HbS (due to increased fetal Hb production) than is observed in typical adult Hb profiles.

Additionally, the MS formulation of the test can be performed and interpreted more rapidly than the HS formulation. Inexperienced users were able to make accurate visual diagnoses from blood stain patterns within 11 minutes of deposition onto

chromatography paper (i.e., before the blood stains in paper were fully dry) which corresponds to 21 minutes from the start of the test. This is an improvement over the reported readout time of 30 minutes for the HS test. The more rapid availability of test results could permit immediate clinical intervention at the point-of-care and could potentially enable counseling of families with SCA newborns before postpartum discharge. The ability to deliver results during the first visit to a health clinic is vital because in regions which lack established communication infrastructure, re-contact and follow-up rates for affected newborns have been reported to be as low as 50% (McGann et al., 2013).

Finally, utilizing MS allowed for the design of a self-contained, low-cost test kit comprised of easily accessible, food-grade reagents (not an option for HS) and off-the-shelf disposable plastic components with a total cost of $0.21 (USD) (Table 5.1). The test kit consists of a blood dropper, reagent dropper, reagent tube, food grade reagents, chromatography paper and a foil pouch (Fig. 5.1a), with >66% of the total cost being accounted for by the disposable plastic droppers. Switching from HS to MS also decreased the amortized cost of the test significantly (primarily due to shipping restrictions on sodium hydrosulfite). The transportation, storage, and material cost savings of this MS-based test, as well as the wide availability of food-grade sodium metabisulfite, make the SCA screening test a tangible reality in even the most resource-limited settings.

The MS formulation of the paper-based test described in this study has two important limitations. First, when visually interpreted, the test cannot differentiate between SCA and other heterozygous forms of SCD (e.g., *HbSC*). This is because the

blood stain pattern produced in paper is determined by the concentration of HbS in the blood sample being tested and is unaffected by the relative proportions of other soluble forms of Hb making up the rest of the sample. As such, the paper-based test would have the highest clinical utility in regions with low SCD genotypic variation (e.g., Angola where the majority of SCD cases are SCA (McGann et al., 2013)) and lowest utility in regions where other forms of SCD are present (e.g., Burkina Faso and Central West Africa where *HbSC* is prevalent (R. L. Nagel, M. E. Fabry, & M. H. Steinberg, 2003; Kate Ryan et al., 2010)). Importantly however, we have previously shown that automated image analysis of scanned blood stain patterns can be used to differentiate *HbAS* from *HbSC* (sensitivity of 100%, specificity of 59%) despite human scorers being unable to differentiate the patterns by eye (N. Z. Piety et al., 2016). Second, while the LOD of the MS formulation of the test has been improved to 10% HbS, this LOD may still be insufficient for detecting SCT or SCA in newborns less than 6 months of age. This is because at birth the cord blood of SCT newborns contains 9.5 ± 4.2% HbA and 6.5 ± 2.8% HbS, and the blood of newborns with SCA contains 10.2 ± 3.9% HbS, meaning that newborns with HbS concentrations near the low end of this physiological range may produce false negative results (Dominic Edoh, Charles Antwi-Bosaiko, & Dominic Amuzu, 2006; Kate Ryan et al., 2010).(D. Edoh, C. Antwi-Bosaiko, & D. Amuzu, 2006; K. Ryan et al., 2010) To address this limitation we have previously developed and validated a separate HS-based test which employs a disposable filter to further improve the LOD of the test, however this version of the test is currently incapable of differentiating SCT from SCA (Piety, George, et al., 2017).

In summary, we have improved and characterized the performance of our previously developed paper-based test for rapid, low-cost, and equipment-free diagnosis of SCA in resource-limited settings. We have demonstrated that the test, compared to previous the version, had a superior limit of detection, faster readout time, better diagnostic performance, longer shelf stability at room temperature, and could be packaged into a self-contained, distributable test kit with a total cost of only $0.21 (USD). A point-of-care test with these qualities represents a significant step towards enabling population-wide screening in resource-limited settings, which, in combination with prompt initiation of prophylactic treatment, could have a transformative impact on the health and well-being of the hundreds of thousands of individuals with SCA born in developing countries each year.

5.6 Conclusions

We continue to use principles learned from the rheological assessment of RBCs to inform device design and validate novel techniques for purification of abberant blood components, in this case by translating a previously described paper-based laboratory assay for screening sickle cell anemia (SCA) for use in the field (N. Z. Piety et al., 2016). The failure-mode of this assay, conceived for use in resource limited settings due to its potential for low cost, centered on instability of the central reagent used in the assay during storage. The assay functions by lysing RBCs in a 20μL drop of blood to release Hb into 200μL of concentrated phosphate solution. Aside from containing the lysing agent saponin (4g/L), and the concentrated phosphate buffer (1.25M dibasic and 1.24 molar monobasic potassium phosphate), it contains a strong reducing agent sodium

hydrosulfite (HS) (30g/L) (3%w/v). This reducing agent deoxygenates HbS causing it to polymerize. Given the significantly lower solubility of deoxygenated HbS than oxygenated HbA, HbS and deoxygenated HbA in concentrated phosphate solution the HbS polymers precipitate out of solution within 10 minutes. Upon dropping this mixture onto chromatography paper, deoxygenated HbS polymers get trapped and produce a dark red circle due to the iron in the Hb. Other soluble forms of Hb present in the solution spread through the chromatography paper to produce a diffuse pink circle. The intensity of the small red circle compared to that of the diffuse pink circle indicates the ratio of HbS to other forms of Hb in the blood drop.

However, HS's sensitivity to oxygen causes it to be highly combustible and unstable, making it impractical to ship and store. As part of the effort to package the assay in a distributable format we proposed substituting HS with a higher concentration of a less reactive, more stable, reducing agent. Sodium metabisulfite (MS), an ingredient often found in wine to preserve freshness, substituted at 5-times the concentration of HS (150g/L, 15%w/v) produced best results. In fact, upon visual inspection of the circular stains, it was able to distinguish 10% HbS in a blood sample, whereas the HS formulation of the assay was only able to distinguish 20% HbS.

Results from this study demonstrate the potential of the assay to reach a wide population of people to screen for HbS, or even diagnose *HbAS* and *HbSS* in the resource-limited settings where these hemoglobinopathies are most prevalent.

CONCLUSIONS

By first understanding the difficulty in reliably measuring RBC properties in pathological RBC populations, and drawing inspiration from biochemical assays used to evaluate the quality of other blood components, we were able to design and validate devices for the separation of various blood components for therapeutic and diagnostic purposes. In chapter 1, while characterizing the lack of efficacy of HU for improving the shear deformability of RBCs from *HbSC* patients, we find that ektacytometry EI can be misleading for populations of morphologically abnormal RBCs due to their periodic rotation in the high shear flow. We then use this lesson to explore novel methodology for measuring deformability and aggregation of SCD RBCs in a study to evaluate the potential of plasmapheresis to treat certain SCD pathologies. Then in chapter 2 we continue this exploration by using the assumption made by ektacytometer of generating ellipsoidal sheared RBCs in flow to produce 3D models of the estimated ellipsoidal RBC according to an anomalous diffraction model of the images it produces. We find that it estimates unrealistic shapes for the RBCs of animals with unique RBC morphologies, particularly for small or rigid RBC populations relative to healthy human RBCs. We propose a more biomimetic method to produce a metric of deformability, using an AMVN cast in PDMS, and characterizing unique flow differences in images of the RBCs flowing through the device.

Recognizing that RBC flow is highly dependent on morphology, we design three microfluidic devices that exploit different aspects of morphology to improve access to blood banking and diagnostic technology. First, in chapter 3 we model RBC flow and sedimentation in a simple device to wash RBC units in normal gravity in-line at the

bedside. We show that this device can wash blood on par with industrial centrifugation washers, to reduce the harmful byproducts of long-term storage that can cause sensitization and adverse outcomes in transfusion patients. Our model allows us to quickly protype variations of our device specifications via computer simulation, and informs multiple aspects of the design of this affordable, portable prototype of an alternative to the wasteful centrifuge washing process. Then in chapter 4 we describe the fabrication of a portable device that can passively separate WB into its RBC, platelet concentrate, and plasma components affordably and with high throughput, obviating the wasteful process whereby blood donation centers have to coordinate availability of industrial centrifuge blood component separators. We show that this device produces RBCs with EIs, platelets with aggregation, and plasma with protein concentrations equal to or better than separation by centrifugation. Finally, in chapter 5 we describe the reformulation of a paper-based diagnostic for SCA that operates by trapping HbS polymers into a distinguishable pattern that can be analyzed to roughly quantify %HbS, in order to make it shelf stable enough to distribute to the areas where SCA is most common without degradation. We then assemble a kit with off the shelf components and accompanying open source quantification software for <$0.25 USD. Each of these devices provides significant improvement in desirability, viability, or feasibility with respect to competing technologies, and improves global access to vital biomedical instrumentation.

Additionally, many of the technologies described in this work have continued to evolve and improve. For example, with the addition of a membrane hydrogen composite RBC concentration module downstream of the gravity based washing system, it has

increased throughput tenfold, and can deplete IgA to levels suitable for transfusion into recipients with the most common immunodeficiency disorder in the world, IgA deficiency (Vörös et al., 2018). Notably, the LORRCA ektacytometer has also been updated to include a deoxygenation module, and the SCYTHE clinical trial has been terminated without enough evidence to support the efficacy of HU in treating *HbSC*. The paper-based SCD test is in active development to reduce LOD to a point suitable for screening neonates, and additional CIF applications mentioned at the end of chapter 4 are continuing to develop. Ultimately, the central focus of this work, to encourage design of microfluidic devices inspired by RBC morphology in flow for global health applications has proven to be fruitful.

REFERENCES

Aarts, P., Heethaar, R. M., & Sixma, J. J. (1984). Red blood cell deformability influences platelets--vessel wall interaction in flowing blood. *Blood,* 64(6), 1228-33.

Abkarian, M., Loiseau, E., & Massiera, G. (2011). Continuous droplet interface crossing encapsulation (cDICE) for high throughput monodisperse vesicle design. *Soft Matter, 7*(10), 4610-4614.

Antonelou, M. H., Kriebardis, A. G., Velentzas, A. D., Kokkalis, A. C., Georgakopoulou, S.-C., & Papassideri, I. S. (2011). Oxidative stress-associated shape transformation and membrane proteome remodeling in erythrocytes of end stage renal disease patients on hemodialysis. *Journal of proteomics, 74*(11), 2441-2452.

Ballas, S. K., Dover, G. J., & Charache, S. (1989). Effect of hydroxyurea on the rheological properties of sickle erythrocytes in vivo. *American journal of hematology, 32*(2), 104-111.

Baskurt, O., Neu, B., & Meiselman, H. J. (2011). *Red blood cell aggregation*: CRC Press.

Baskurt, O. K., Hardeman, M. R., & Rampling, M. W. (2007). *Handbook of hemorheology and hemodynamics* (Vol. 69): IOS press.

Bennett-Guerrero, E., Veldman, T. H., Doctor, A., Telen, M. J., Ortel, T. L., Reid, T. S., Mulherin, M.S., Zhu, H., Buck, R.D., Califf, R. M. (2007). Evolution of adverse changes in stored RBCs. *Proceedings of the National Academy of Sciences, 104*(43), 17063-17068.

Bessis, M., & Mohandas, N. (1978). Laser diffraction patterns of sickle cells in fluid shear fields. In *Red Cell Rheology* (pp. 225-235): Springer.

Bessos, H., & Seghatchian, J. (2005). Red cell storage lesion: the potential impact of storage-induced CD47 decline on immunomodulation and the survival of leucofiltered red cells. *Transfusion and Apheresis Science, 32*(2), 227-232.

Bhaduri, B., Kandel, M., Brugnara, C., Tangella, K., & Popescu, G. (2014). Optical assay of erythrocyte function in banked blood. *Scientific reports, 4*, 6211.

Boga, C., Kozanoglu, I., Ozdogu, H., & Ozyurek, E. (2007). Plasma exchange in critically ill patients with sickle cell disease. *Transfusion and Apheresis Science, 37*(1), 17-22.

Brune, T., Fill, S., Heim, G., Rabsilber, A., Wohlfarth, K., & Garritsen, H. S. (2007). Quality and stability of red cells derived from gravity-separated placental blood with a hollow-fiber system. *Transfusion, 47*(12), 2271-2275.

Bruus, H. (2014). Governing equations in microfluidics.

Burns, J. M., Yang, X., Forouzan, O., Sosa, J. M., & Shevkoplyas, S. S. (2012). Artificial microvascular network: a new tool for measuring rheologic properties of stored red blood cells. *Transfusion, 52*(5), 1010-1023.

Burrin, D., Ferrell, C. L., Eisemann, J., Britton, R., & Nienaber, J. (1989). Effect of level of nutrition on splanchnic blood flow and oxygen consumption in sheep. *British Journal of Nutrition, 62*(1), 23-34.

Canham, P. B. (1970). The minimum energy of bending as a possible explanation of the biconcave shape of the human red blood cell. *Journal of theoretical biology, 26*(1), 61-81.

Carson, J. L., Kleinman, S., Silvergleid, A. J., & Tirnauer, J. S. (2018). "Indications and hemoglobin thresholds for red blood cell transfusion in the adult." *UpToDate*

Chaudhuri, O., Parekh, S. H., Lam, W. A., & Fletcher, D. A. (2009). Combined atomic force microscopy and side-view optical imaging for mechanical studies of cells. *Nature methods, 6*(5), 383.

Chien, S. (1987). Red cell deformability and its relevance to blood flow. *Annual review of physiology, 49*(1), 177-192.

Cines, D. B., Lebedeva, T., Nagaswami, C., Hayes, V., Massefski, W., Litvinov, R. I., Rauova, L., Lowery, T. J., Weisel, J. W. (2014). Clot contraction: compression of erythrocytes into tightly packed polyhedra and redistribution of platelets and fibrin. *Blood, The Journal of the American Society of Hematology, 123*(10), 1596-1603.

Cronin, E., Normand, C., Henthorn, J., Hickman, M., & Davies, S. (1998). Costing model for neonatal screening and diagnosis of haemoglobinopathies. *Archives of Disease in Childhood-Fetal and Neonatal Edition, 79*(3), F161-F167.

D'Alessandro, A., Liumbruno, G., Grazzini, G., & Zolla, L. (2010). Red blood cell storage: the story so far. *Blood Transfusion, 8*(2), 82.

Diallo, D., & Tchernia, G. (2002). Sickle cell disease in Africa. *Current opinion in hematology, 9*(2), 111-116.

Diez-Silva, M., Dao, M., Han, J., Lim, C.-T., & Suresh, S. (2010). Shape and biomechanical characteristics of human red blood cells in health and disease. *MRS bulletin, 35*(5), 382-388.

Dill, D. B., & Costill, D. L. (1974). Calculation of percentage changes in volumes of blood, plasma, and red cells in dehydration. *Journal of applied physiology, 37*(2), 247-248.

Dimitrakopoulos, P. (2012). Analysis of the variation in the determination of the shear modulus of the erythrocyte membrane: effects of the constitutive law and membrane modeling. *Physical Review E, 85*(4), 041917.

Duprat, C., & Shore, H. A. (2015). *Fluid-Structure Interactions in Low-Reynolds-Number Flows*: Royal Society of Chemistry.

Edgren, G., Kamper-Jørgensen, M., Eloranta, S., Rostgaard, K., Custer, B., Ullum, H., Murphy, E. L., Busch, M. P., Reilly, M., Melbye, M. (2010). Duration of red blood cell storage and survival of transfused patients (CME). *Transfusion, 50*(6), 1185-1195.

Edoh, D., Antwi-Bosaiko, C., & Amuzu, D. (2006). Fetal hemoglobin during infancy and in sickle cell adults. *Afr Health Sci, 6*(1), 51-54. doi:10.5555/afhs.2006.6.1.51

Edoh, D., Antwi-Bosaiko, C., & Amuzu, D. (2006). Fetal hemoglobin during infancy and in sickle cell adults. *African health sciences, 6*(1), 51-54.

Evans, E. A. (1980). Minimum energy analysis of membrane deformation applied to pipet aspiration and surface adhesion of red blood cells. *Biophysical journal, 30*(2), 265-284.

Fahraeus, R., & Lindqvist, T. (1931). The viscosity of the blood in narrow capillary tubes. *American Journal of Physiology-Legacy Content, 96*(3), 562-568.

Fields, M. E., Hulbert, M. L., Chen, L., Berlin, A. N., Jackups, R., & Spinella, P. C. (2015). Red blood cell storage duration is not associated with clinical outcomes for acute chest syndrome in children with sickle cell disease. *Transfusion, 55*(11), 2714-2721.

Fischer, T., Haest, C., Stöhr-Liesen, M., Schmid-Schönbein, H., & Skalak, R. (1981). The stress-free shape of the red blood cell membrane. *Biophysical journal, 34*(3), 409.

Flegel, W. A., Natanson, C., & Klein, H. G. (2014). Does prolonged storage of red blood cells cause harm? *British journal of haematology, 165*(1), 3-16.

Fleiss, J. L. (1971). Measuring nominal scale agreement among many raters. *Psychological bulletin, 76*(5), 378.

Flormann, D., Aouane, O., Kaestner, L., Ruloff, C., Misbah, C., Podgorski, T., & Wagner, C. (2017). The buckling instability of aggregating red blood cells. *Scientific reports, 7*(1), 7928.

Frank, S. M., Abazyan, B., Ono, M., Hogue, C. W., Cohen, D. B., Berkowitz, D. E., . . . Barodka, V. M. (2013). Decreased erythrocyte deformability after transfusion and the effects of erythrocyte storage duration. *Anesthesia and analgesia, 116*(5), 975.

Gifford, S. C., Spillane, A. M., Vignes, S. M., & Shevkoplyas, S. S. (2014). Controlled incremental filtration: a simplified approach to design and fabrication of high-throughput microfluidic devices for selective enrichment of particles. *Lab on a chip, 14*(23), 4496-4505.

Gifford, S. C., Strachan, B. C., Xia, H., Vörös, E., Torabian, K., Tomasino, T. A., Griffin, G. D., Lichtiger, B., Aung, F. M., Shevkoplyas, S. S. (2018). A portable system for processing donated whole blood into high quality components without centrifugation. *PloS one, 13*(1), e0190827.

Glynn, S. A. (2010). The red blood cell storage lesion: a method to the madness. *Transfusion, 50*(6), 1164-1169.

Guevorkian, K., Colbert, M.-J., Durth, M., Dufour, S., & Brochard-Wyart, F. (2010). Aspiration of biological viscoelastic drops. *Physical review letters, 104*(21), 218101.

Hardeman, M., Goedhart, P., Dobbe, J., & Lettinga, K. (1994). Laser-assisted optical rotational cell analyser (LORCA); I. A new instrument for measurement of various structural hemorheological parameters. *Clinical hemorheology and microcirculation, 14*(4), 605-618.

Head, C., Conroy, M., Jarvis, M., Phelan, L., & Bain, B. (2004). Some observations on the measurement of haemoglobin A2 and S percentages by high performance liquid chromatography in the presence and absence of α thalassaemia. *Journal of clinical pathology, 57*(3), 276-280.

Hess, J. (2014). Measures of stored red blood cell quality. *Vox sanguinis, 107*(1), 1-9.

Hess, J. R. (2010). Conventional blood banking and blood component storage regulation: opportunities for improvement. *Blood Transfusion, 8*(Suppl 3), s9.

Hickcox, D. H. (1986). 1985 temperature extremes: the hottest and the coldest. *Weatherwise, 39*(1), 21-23.

Hinch, E., & Leal, L. (1979). Rotation of small non-axisymmetric particles in a simple shear flow. *Journal of Fluid Mechanics, 92*(3), 591-607.

Horiuchi, K., Ballas, S. K., & Asakura, T. (1988). The effect of deoxygenation rate on the formation of irreversibly sickled cells.

Hornsey, V., McColl, K., Drummond, O., & Prowse, C. (2005). Separation of whole blood into plasma and red cells by using a hollow-fibre filtration system. *Vox sanguinis, 89*(2), 81-85.

Itano, H. A. (1953). Solubilities of naturally occurring mixtures of human hemoglobin. *Archives of biochemistry and biophysics, 47*(1), 148-159.

Jain, N., Kono, C., Myers, A., & Bottomly, K. (1980). Fusiform erythrocytes resembling sickle cells in Angora goats: observations on osmotic and mechanical fragilities and reversal of cell shape during anaemia. *Research in veterinary science, 28*(1), 25-35.

Jenkins, M. A., & Ratnaike, S. (1999). Capillary isoelectric focusing of haemoglobin variants in the clinical laboratory. *Clinica chimica acta, 289*(1-2), 121-132.

Khanal, G., Huynh, R. A., Torabian, K., Xia, H., Vörös, E., & Shevkoplyas, S. S. (2018). Towards bedside washing of stored red blood cells: a prototype of a simple apparatus based on microscale sedimentation in normal gravity. *Vox sanguinis, 113*(1), 31-39.

Klein, H. G., Spahn, D. R., & Carson, J. L. (2007). Red blood cell transfusion in clinical practice. *The Lancet, 370*(9585), 415-426.

Knowlton, S., Sencan, I., Aytar, Y., Khoory, J., Heeney, M., Ghiran, I., & Tasoglu, S. (2015). Sickle cell detection using a smartphone. *Scientific reports, 5*, 15022.

Kumar, A. A., Chunda-Liyoka, C., Hennek, J. W., Mantina, H., Lee, S. R., Patton, M. R., . . . Chintu, C. (2014a). Evaluation of a density-based rapid diagnostic test for sickle cell disease in a clinical setting in Zambia. *PloS one, 9*(12).

Kumar, A. A., Chunda-Liyoka, C., Hennek, J. W., Mantina, H., Lee, S. R., Patton, M. R., Sambo, P., Sinyangwe, S., Kankasa, C., Chintu, C. (2014b). Evaluation of a density-based rapid diagnostic test for sickle cell disease in a clinical setting in Zambia. *PloS one, 9*(12), e114540.

Kumar, A. A., Patton, M. R., Hennek, J. W., Lee, S. Y. R., D'Alesio-Spina, G., Yang, X., Kanter, J., Shevkoplyas, S., Brugnara, C., Whitesides, G. M. (2014). Density-based separation in multiphase systems provides a simple method to identify sickle cell disease. *Proceedings of the National Academy of Sciences, 111*(41), 14864-14869.

LaLonde, A., Romero-Creel, M. F., Saucedo-Espinosa, M. A., & Lapizco-Encinas, B. H. (2015). Isolation and enrichment of low abundant particles with insulator-based dielectrophoresis. *Biomicrofluidics, 9*(6), 064113.

Lassen, N. A. (1959). Cerebral blood flow and oxygen consumption in man. *Physiological reviews, 39*(2), 183-238.

Li, J., Lykotrafitis, G., Dao, M., & Suresh, S. (2007). Cytoskeletal dynamics of human erythrocyte. *Proceedings of the National Academy of Sciences, 104*(12), 4937-4942.

Lien, V., & Vollmer, F. (2007). Microfluidic flow rate detection based on integrated optical fiber cantilever. *Lab on a chip, 7*(10), 1352-1356.

Liu, X., Tang, Z.-y., Zeng, Z., Chen, X., Yao, W.-j., Yan, Z.-y., Shi, Y., Shan, H.-x., Sun, D.-g., He, D.-q. (2007). The measurement of shear modulus and membrane surface viscosity of RBC membrane with Ektacytometry: A new technique. *Mathematical biosciences, 209*(1), 190-204.

Loiseau, E., Massiera, G., Mendez, S., Martinez, P. A., & Abkarian, M. (2015). Microfluidic study of enhanced deposition of sickle cells at acute corners. *Biophysical journal, 108*(11), 2623-2632.

Luo, Q., Ren, T., Shen, H., Liang, D., & Zhang, J. (2017). Comparison of thermal hazards of sodium dithionite and thiourea dioxide from thermal analysis (DSC-TG), small-scale self-heating experiments and FTIR smoke gas analysis. *Fire Safety Journal, 92*, 91-97.

Makani, J., Cox, S. E., Soka, D., Komba, A. N., Oruo, J., Mwamtemi, H., Magesa, P., Rwezaula, S., Meda, E., Mgaya, J. (2011). Mortality in sickle cell anemia in Africa: a prospective cohort study in Tanzania. *PloS one, 6*(2).

Malanchuk, M. (1971). Thermal analysis of sodium metabisulfite. *Analytica chimica acta, 56*(3), 377-384.

McGann, P. T., Ferris, M. G., Ramamurthy, U., Santos, B., de Oliveira, V., Bernardino, L., & Ware, R. E. (2013). A prospective newborn screening and treatment program for sickle cell anemia in Luanda, Angola. *American journal of hematology, 88*(12), 984-989.

McGann, P. T., Grosse, S. D., Santos, B., de Oliveira, V., Bernardino, L., Kassebaum, N. J., Ware, R. E., Airewele, G. E. (2015). A cost-effectiveness analysis of a pilot neonatal screening program for sickle cell anemia in the Republic of Angola. *The Journal of pediatrics, 167*(6), 1314-1319.

McGann, P. T., Schaefer, B. A., Paniagua, M., Howard, T. A., & Ware, R. E. (2016). Characteristics of a rapid, point-of-care lateral flow immunoassay for the diagnosis of sickle cell disease. *American journal of hematology, 91*(2), 205-210.

Mgharbel, A., Delanoë-Ayari, H., & Rieu, J. P. (2009). Measuring accurately liquid and tissue surface tension with a compression plate tensiometer. *HFSP journal, 3*(3), 213-221.

Middelburg, R. A., van de Watering, L. M., Briët, E., & van der Bom, J. G. (2013). Storage time of red blood cells and mortality of transfusion recipients. *Transfusion Medicine Reviews, 27*(1), 36-43.

Modell, B., & Darlison, M. (2008). Global epidemiology of haemoglobin disorders and derived service indicators. *Bulletin of the World Health Organization, 86*, 480-487.

Mohandas, N., & Evans, E. (1994). Mechanical properties of the red cell membrane in relation to molecular structure and genetic defects. *Annual review of biophysics and biomolecular structure, 23*(1), 787-818.

Montagu, D., Yamey, G., Visconti, A., Harding, A., & Yoong, J. (2011). Where do poor women in developing countries give birth? A multi-country analysis of demographic and health survey data. *PloS one, 6*(2), e17155.

Nagel, R. L., Fabry, M. E., & Steinberg, M. H. (2003). The paradox of hemoglobin SC disease. *Blood Rev, 17*(3), 167-178. Retrieved from http://www.ncbi.nlm.nih.gov/pubmed/12818227

Nagel, R. L., Fabry, M. E., & Steinberg, M. H. (2003). The paradox of hemoglobin SC disease. *Blood reviews, 17*(3), 167-178.

Nguyen-Khoa, T., Mine, L., Allaf, B., Ribeil, J.-A., Remus, C., Stanislas, A., Gauthereua, V., Enouz, S., Kim, J. S., Yang, X. (2018). *Sickle SCAN™(BioMedomics) fulfills analytical conditions for neonatal screening of sickle cell disease.* Paper presented at the Annales de biologie clinique.

Organization, W. H. (2017). The 2016 global status report on blood safety and availability.

Pavenski, K., Saidenberg, E., Lavoie, M., Tokessy, M., & Branch, D. R. (2012). Red blood cell storage lesions and related transfusion issues: a Canadian Blood Services research and development symposium. *Transfusion Medicine Reviews, 26*(1), 68-84.

Pereira, A. (2013). Will clinical studies elucidate the connection between the length of storage of transfused red blood cells and clinical outcomes? An analysis based on the simulation of randomized controlled trials. *Transfusion, 53*(1), 34-40.

Pfuntner, A., Wier, L., & Stocks, C. (2006). "Most frequent procedures performed in US hospitals, 2011: statistical brief# 165."

Piel, F. B., Hay, S. I., Gupta, S., Weatherall, D. J., & Williams, T. N. (2013). Global burden of sickle cell anaemia in children under five, 2010–2050: modelling based on demographics, excess mortality, and interventions. *PLoS medicine, 10*(7).

Piety, N. Z., George, A., Serrano, S., Lanzi, M. R., Patel, P. R., Noli, M. P., Kahan, S., Nirenberg, D., Camanda, J. F., Airewele, G. (2017). A paper-based test for screening newborns for sickle cell disease. *Scientific reports, 7*(1), 1-8.

Piety, N. Z., Reinhart, W. H., Pourreau, P. H., Abidi, R., & Shevkoplyas, S. S. (2016). Shape matters: the effect of red blood cell shape on perfusion of an artificial microvascular network. *Transfusion, 56*(4), 844-851.

Piety, N. Z., Reinhart, W. H., Stutz, J., & Shevkoplyas, S. S. (2017). Optimal hematocrit in an artificial microvascular network. *Transfusion, 57*(9), 2257-2266.

Piety, N. Z., Yang, X., Kanter, J., Vignes, S. M., George, A., & Shevkoplyas, S. S. (2016). Validation of a Low-Cost Paper-Based Screening Test for Sickle Cell Anemia. *PloS one, 11*(1), e0144901. doi:10.1371/journal.pone.0144901

Piety, N. Z., Yang, X., Lezzar, D., George, A., & Shevkoplyas, S. S. (2015). A rapid paper-based test for quantifying sickle hemoglobin in blood samples from patients with sickle cell disease. *American journal of hematology, 90*(6), 478-482.

Platt, O. S., Brambilla, D. J., Rosse, W. F., Milner, P. F., Castro, O., Steinberg, M. H., & Klug, P. P. (1994). Mortality in sickle cell disease--life expectancy and risk factors for early death. *New England Journal of Medicine, 330*(23), 1639-1644.

Powars, D. R., Chan, L. S., Hiti, A., Ramicone, E., & Johnson, C. (2005). Outcome of sickle cell anemia: a 4-decade observational study of 1056 patients. *Medicine, 84*(6), 363-376.

Rabai, M., Detterich, J. A., Wenby, R. B., Hernandez, T. M., Toth, K., Meiselman, H. J., & Wood, J. C. (2014). Deformability analysis of sickle blood using ektacytometry. *Biorheology, 51*(2-3), 159-170.

Radwanski, K., Garraud, O., Cognasse, F., Hamzeh-Cognasse, H., Payrat, J. M., & Min, K. (2013). The effects of red blood cell preparation method on in vitro markers of red blood cell aging and inflammatory response. *Transfusion, 53*(12), 3128-3138.

Rees, D. C., Williams, T. N., & Gladwin, M. T. (2010). Sickle-cell disease. *The Lancet, 376*(9757), 2018-2031.

Reinhart, W. H., Piety, N. Z., Deuel, J. W., Makhro, A., Schulzki, T., Bogdanov, N., . . . Shevkoplyas, S. S. (2015). Washing stored red blood cells in an albumin solution improves their morphologic and hemorheologic properties. *Transfusion, 55*(8), 1872-1881.

Renoux, C., Parrow, N., Faes, C., Joly, P., Hardeman, M., Tisdale, J., Levine, M., Garnier, N., Betrand, Y., Kebaili, K. (2016). Importance of methodological

standardization for the ektacytometric measures of red blood cell deformability in sickle cell anemia. *Clinical hemorheology and microcirculation, 62*(2), 173-179.

Resnick, N., Yahav, H., Shay-Salit, A., Shushy, M., Schubert, S., Zilberman, L. C. M., & Wofovitz, E. (2003). Fluid shear stress and the vascular endothelium: for better and for worse. *Progress in biophysics and molecular biology, 81*(3), 177-199.

Rinalducci, S., & Zolla, L. (2015). Biochemistry of storage lesions of red cell and platelet concentrates: a continuous fight implying oxidative/nitrosative/phosphorylative stress and signaling. *Transfusion and Apheresis Science, 52*(3), 262-269.

Roberts, D. E., McNicol, A., & Bose, R. (2004). Mechanism of collagen activation in human platelets. *Journal of Biological Chemistry, 279*(19), 19421-19430.

Roila, F., Lupattelli, M., Sassi, M., Basurto, C., Bracarda, S., Picciafuoco, M., Boschetti, E., Milella, G., Ballatori, E., Tonato, M. (1991). Intra and interobserver variability in cancer patients' performance status assessed according to Karnofsky and ECOG scales. *Annals of Oncology, 2*(6), 437-439.

Ryan, K., Bain, B. J., Worthington, D., James, J., Plews, D., Mason, A., Roper, D., Rees, D. C., De La Salle, B., Streetly, A. (2010). Significant haemoglobinopathies: guidelines for screening and diagnosis. *British journal of haematology, 149*(1), 35-49.

Salomao, M., An, X., Guo, X., Gratzer, W. B., Mohandas, N., & Baines, A. J. (2006). Mammalian αI-spectrin is a neofunctionalized polypeptide adapted to small highly deformable erythrocytes. *Proceedings of the National Academy of Sciences, 103*(3), 643-648.

Sarma, P. R. (1990). Red cell indices. In *Clinical Methods: The History, Physical, and Laboratory Examinations. 3rd edition*: Butterworths.

Segbena, A. Y., Guindo, A., Buono, R., Kueviakoe, I., Diallo, D. A., Guernec, G., Yerima, M., Guindo, P., Lauressergus, E., Mondeilh, A. (2018). Diagnostic accuracy in field conditions of the sickle SCAN® rapid test for sickle cell disease among children and adults in two West African settings: the DREPATEST study. *BMC hematology, 18*(1), 26.

Shiga, T., Maeda, N., & Kon, K. (1990). Erythrocyte rheology. *Critical Reviews in Oncology/Hematology, 10*(1), 9-48.

Shin, S., Hou, J., Suh, J., & Singh, M. (2007). Validation and application of a microfluidic ektacytometer (RheoScan-D) in measuring erythrocyte deformability. *Clinical hemorheology and microcirculation, 37*(4), 319-328.

Shin, S., Hou, J. X., Suh, J. S., & Singh, M. (2007). Validation and application of a microfluidic ektacytometer (RheoScan-D) in measuring erythrocyte deformability. *Clin Hemorheol Microcirc, 37*(4), 319-328.

Sia, S. K., & Whitesides, G. M. (2003). Microfluidic devices fabricated in poly (dimethylsiloxane) for biological studies. *Electrophoresis, 24*(21), 3563-3576.

Silva, D. C., Jovino, C. N., Silva, C. A., Fernandes, H. P., M Filho, M., Lucena, S. C., Costa, A. M., Cesar, C. L., Barjas-Castro, M. L., Santos, B. S. (2012). Optical tweezers as a new biomedical tool to measure zeta potential of stored red blood cells. *PloS one, 7*(2).

Skalak, R., & Branemark, P. (1969). Deformation of red blood cells in capillaries. *Science, 164*(3880), 717-719.

Smith, J. E., Mohandas, N., & Shohet, S. B. (1979). Variability in erythrocyte deformability among various mammals. *American Journal of Physiology-Heart and Circulatory Physiology, 236*(5), H725-H730.

Sosa, J. M., Nielsen, N. D., Vignes, S. M., Chen, T. G., & Shevkoplyas, S. S. (2014). The relationship between red blood cell deformability metrics and perfusion of an artificial microvascular network. *Clinical hemorheology and microcirculation, 57*(3), 275-289.

Strachan, B. C., Xia, H., VÖRÖS, E., Gifford, S. C., & Shevkoplyas, S. S. (2019). Improved expansion of T cells in culture when isolated with an equipment-free, high-throughput, flow-through microfluidic module versus traditional density gradient centrifugation. *Cytotherapy, 21*(2), 234-245.

Streekstra, G., Dobbe, J., & Hoekstra, A. (2010). Quantification of the fraction poorly deformable red blood cells using ektacytometry. *Optics express, 18*(13), 14173-14182.

Streekstra, G. J., Hoekstra, A. G., Nijhof, E.-J., & Heethaar, R. M. (1993). Light scattering by red blood cells in ektacytometry: Fraunhofer versus anomalous diffraction. *Applied Optics, 32*(13), 2266-2272.

Stuart, M. J., & Nagel, R. L. (2004). Sickle-cell disease. *The Lancet, 364*(9442), 1343-1360.

Suresh, S. (2006). Mechanical response of human red blood cells in health and disease: Some structure-property-function relationships. *Journal of materials research, 21*(8), 1871-1877.

Tinmouth, A., & Chin-Yee, I. (2001). The clinical consequences of the red cell storage lesion. *Transfusion Medicine Reviews, 15*(2), 91-107.

Torabian, K., Lezzar, D., Piety, N. Z., George, A., & Shevkoplyas, S. S. (2017). Substituting sodium hydrosulfite with sodium metabisulfite Improves long-term stability of a distributable paper-based test kit for point-of-care screening for sickle cell anemia. *Biosensors, 7*(3), 39.

Van de Watering, L. (2011). Red cell storage and prognosis. *Vox sanguinis, 100*(1), 36-45.

Verhoeven, A. (2004). Quality determinants of erythrocyte destined for transfusion. *Cellular and molecular biology (Noisy-le-Grand, France), 50*(2), 187-195.

Vichinsky, E., Hurst, D., Earles, A., Kleman, K., & Lubin, B. (1989). Newborn screening for sickle cell disease: effect on mortality. *Pediatrics, 83*(5), 834-834.

Vörös, E., Piety, N. Z., Strachan, B. C., Lu, M., & Shevkoplyas, S. S. (2018). Centrifugation-free washing: A novel approach for removing immunoglobulin A from stored red blood cells. *American journal of hematology, 93*(4), 518-526.

Ware, R. E. (2013). Is sickle cell anemia a neglected tropical disease? *PLoS neglected tropical diseases, 7*(5).

Wasserman, L. R., & Gilbert, H. S. (1963). Surgery in polycythemia vera. *New England Journal of Medicine, 269*(23), 1226-1230.

Weatherall, D. (2010). The inherited diseases of hemoglobin are an emerging global health burden. *Blood, 115*(22), 4331-4336.

Weed, R. I., LaCelle, P. L., & Merrill, E. W. (1969). Metabolic dependence of red cell deformability. *The Journal of clinical investigation, 48*(5), 795-809.

Weiss, D. J., & Wardrop, K. J. (2011). *Schalm's veterinary hematology*: John Wiley & Sons.

Whitesides, G. M., Ostuni, E., Takayama, S., Jiang, X., & Ingber, D. E. (2001). Soft lithography in biology and biochemistry. *Annual review of biomedical engineering, 3*(1), 335-373.

Whittaker, S., & Winton, F. (1933). The apparent viscosity of blood flowing in the isolated hindlimb of the dog, and its variation with corpuscular concentration. *The Journal of physiology, 78*(4), 339-369.

Wong, A. P., Gupta, M., Shevkoplyas, S. S., & Whitesides, G. M. (2008). Egg beater as centrifuge: isolating human blood plasma from whole blood in resource-poor settings. *Lab on a chip, 8*(12), 2032-2037.

Wong, P. (2006). The behavior of the human erythrocyte as an imperfect osmometer: a hypothesis. *Journal of theoretical biology, 238*(1), 167-171.

Xia, H., Strachan, B. C., Gifford, S. C., & Shevkoplyas, S. S. (2016). A high-throughput microfluidic approach for 1000-fold leukocyte reduction of platelet-rich plasma. *Scientific reports, 6*, 35943.

Yang, X., Kanter, J., Piety, N. Z., Benton, M. S., Vignes, S. M., & Shevkoplyas, S. S. (2013). A simple, rapid, low-cost diagnostic test for sickle cell disease. *Lab on a chip, 13*(8), 1464-1467.

Zimring, J. C. (2015). Established and theoretical factors to consider in assessing the red cell storage lesion. *Blood, The Journal of the American Society of Hematology, 125*(14), 2185-2190.

FINANCIAL SUPPORT

This work was supported in part by the 2012 NIH Director's Transformative Research Award (R01HL117329, PI: Shevkoplyas), and the 2017 STEM Chateaubriand Fellowship of the Office for Science & Technology of the Embassy of France in the United States (PI: Torabian).

APPENDICES

A Vita

Kian Torabian

818-224-8628 | ktorabian@gmail.com | Los Angeles, CA

Doctor of Philosophy, Biomedical Engineering *Anticipated* May 2020

University of Houston, Houston, Texas

Advisor: Dr. Sergey S. Shevkoplyas

Dissertation: Microfluidic Devices for the Diagnosis, Monitoring, and Filtration of Morphologically Aberrant Red Blood Cells

GPA: 3.9/4.0

Research Interests: Microfabrication, micromanipulation, and biochemical applications in blood flow, cell deformability, and cell-cell interactions

Bachelor of Science, Bioengineering with a minor in Computer Science June 2013

Stanford University, Stanford, California

GPA: 3.2/4.0

Research Interests: Computational microbiology and synthetic biology to study and manipulate bacterial cell growth under high thermodynamic and kinetic stress

---

PUBLICATIONS

1. Torabian K, Lezzar D, Piety NZ, George A, Shevkoplyas SS. *Substituting Sodium Hydrosulfite with Sodium Metabisulfite Improves Long-Term Stability of a Distributable Paper-Based Test Kit for Point-of-Care Screening for Sickle Cell Anemia*. Biosensors (Basel). 2017;7(3)
2. Khanal G, Huynh RA, Torabian K, Xia H, Vörös E, Shevkoplyas SS. *Towards bedside washing of stored red blood cells: a prototype of a simple apparatus based on microscale sedimentation in normal gravity*. Vox Sang. 2018;113(1):31-39.
3. Gifford SC, Strachan BC, Xia H, et al. *A portable system for processing donated whole blood into high quality components without centrifugation*. PLoS ONE. 2018;13(1):e0190827.

ACADEMIC HONORS

2016 STEM Chateaubriand Fellowship, Fellow, 6 month travel and research stipend
Project: *The Effect of Plasma on Red Blood Cell Deformability and Aggregation in HbSS and HbSC Diseases Evaluated with Micropipetting, Microfluidics, Ektacytometry, and Bulk Aggregation*
K. Torabian, M. Abkarian, S. Shevkoplyas, P. Connes
University of Houston, Université de Lyon, Université de Montpellier

2016 NSF 15th International Summer School on Biocomplexity, Biodesign and Bioinnovation, Fellow, travel and conference expenses stipend
Talk: *Low-Cost Methods for Washing Red Blood Cells to Improve Transfusion Outcomes*
K. Torabian, G. Khanal, R. Huynh, S. Shevkoplyas
University of Houston

2015 University of Houston Graduate Travel Award, Biomedical Engineering Society (BMES) General Meeting
Talk: *A Distributable Paper-based Diagnostic Kit for Point-of-Care Screening for Sickle Cell Disease*
K. Torabian, D. Lezzar, N. Piety, A. George, S. Shevkoplyas
University of Houston, Baylor College of Medicine

2012 Stanford Summer Research Experience for Undergraduates (REU), Fellow, summer research stipend
Project: *Cell Division in Flattened Cells: Min Protein Regulation, and Growth Rate in E. coli*
K. Torabian, E. Rojas, M. Goulian, KC Huang
Stanford University, University of Pennsylvania

TALKS AND POSTERS

Biomedical Engineering Society (BMES) General Meeting 10/8/2016 (Talk) Minneapolis, MN
Comparative Deformability and Microfluidic Perfusion of Human and Nonhuman Red Blood Cells
P. Murugan, K. Torabian, N. Piety, S. Shevkoplyas
University of Houston

Biomedical Engineering Society (BMES) General Meeting 10/6/2016 (Session Keynote) Minneapolis, MN
A Distributable Paper-based Diagnostic Kit for Point-of-Care Screening for Sickle Cell Disease
K. Torabian, D. Lezzar, N. Piety, A. George, S. Shevkoplyas
University of Houston, Baylor College of Medicine

NSF 15th International Summer School on Biocomplexity, Biodesign and Bioinnovation 06/27/2016 (Talk) Izmir, Turkey
Low-Cost Methods for Washing Red Blood Cells to Improve Transfusion Outcomes
K. Torabian, G. Khanal, R. Huynh, S. Shevkoplyas
University of Houston

Biomedical Engineering Society (BMES) General Meeting 10/8/2015 (Talk) Tampa, FL
Bedside Washing of Stored Red Blood Cells: A Simple Apparatus Based on Microscale Sedimentation in Normal Gravity
G. Khanal, R. Huynh, K. Torabian, S. Gifford, S. Shevkoplyas
University of Houston

Graduate Research and Scholarship Projects (GRASP) Day 10/30/2015 (Poster), University of Houston, Houston, TX
Deformability of Red Blood Cells in Sickle Cell Disease; comparison of transfusion and hydroxyurea therapy for patients with HbSS or HbSC disease
K. Torabian, C. Summarell, N. Piety, V. Sheehan, S. Shevkoplyas
University of Houston, Baylor College of Medicine

American Society of Microbiology (ASM) General Meeting 06/01/2012 (Poster), San Francisco, CA
Cell Division in Flattened Cells: Comparison of Growth of E. coli and B. subtilis Under a Flattening Force
K. Torabian, E. Rojas, M. Goulian, KC Huang
Stanford University, University of Pennsylvania

TRAINING

Biology Lab Technique: soft-lithography microfluidics, lateral flow diagnostics, ektacytometry, micropipette manipulation, optical tweezers, hematology, molecular biology (PCR/primer design, gel electrophoresis, bacterial

transformation, ELISA, chromatography, microarray analysis, synthetic DNA and marker selection), MatLab/Octave (signal processing, pattern recognition, sequence alignment/analysis, image processing, laser diffraction modeling, stochastic modeling, machine learning and Arduino control), Comsol (non-linear fluid dynamics), SolidWorks (CAD prototyping and 3D printing), fluorescence and phase microscopy and image informatics (ImageJ, deconvolution, segmentation, lossless transformation/optimization), cell culture, bandsaw, drill press, silicone prototyping, simple breadboard circuit design.

Programming Project Experience: paradigms (pointers, references, object oriented design, classes, inheritance, dynamic memory allocation, many data structures, hashers, function pointers, iterators), systems (client-server design, virtual memory, processes, threads, networking, performance), languages (Cpp, C, Java, Python, Perl, Assembly).

Technical Coursework: computational microbiology and molecular biology, systems biology, biology (physiology, genetics, immunology, biochemistry, cell biology, molecular biology), chemistry (inorganic, organic), math (multivariable calculus, ODEs, PDEs, probability, statistics, algorithm and numerical analysis, set theory, automata theory, signal processing), physics (mechanics, electromagnetism, optics, thermodynamics, fluid mechanics, materials)

RESEARCH

Shevkoplyas Lab, University of Houston

PhD Candidate, Department of Biomedical Engineering, July 2014 – May 2020

Responsible for clinical coordination, kit development, assay improvement, microfluidic device design, and companion cell phone application development for sickle cell diagnosis and monitoring; lead on fluid dynamics modeling and device design of transfusion blood washing device; responsible for biochemical analysis of platelet and plasma quality to evaluate a centrifugation-free device for processing whole blood into transfusion components; lead on high school mentorship project to compare flow dynamics of red blood cells from different animal species

Huang Laboratory of Cellular Organization, Stanford University

Microbiology Researcher, October 2011 – November 2012

Led independent project to record and analyze fluorescent microscopy data and suggest future experiments for the study of bacterial growth and division beneath a cell-flattening membrane force for cell morphology research; presented at the ASM (American Society for Microbiology) international meeting and the Stanford REU Poster Fair

Nolan Lab, Stanford University

Tissue Engineering Research Assistant, October 2010 – February 2011

Helped create 4D simulations of fibroblast motility in different matrices for drug development using imaging informatics and design computation in Processing for Erica Savig (graduate student)

UNPUBLISHED WORK

1. Torabian K, Murugan P, Piety N, Shevkoplyas SS. *Relating the Effects of Nonhuman Red Blood Cell Parameters on Perfusion through an Artificial Microvascular Network and Ektacytometry Shear Elongation Measurements*. Front Physiol. Submission in Progress
2. Summarell C, Torabian K, Sheehan V, Shevkoplyas SS. *Effects of Hydroxyurea on Red Blood Cell Deformability in Patients with Hemoglobin SC Disease*. Baylor College of Medicine Clinical Study 2016.
3. Torabian K, Connes P, Abkarian M, Shevkoplyas SS. T*he Effect of Plasma on Red Blood Cell Deformability and Aggregation in Sickle Cell Disease*. Chateaubriand Fellowship in STEM 2017.

EMPLOYMENT

Kythera Biopharmaceuticals (acquired by Allergan), Calabasas, CA

Marketing and Research Intern Focusing on Technical Writing for Investor Outreach, June to August 2009, 2011

FDA compliance and technical research expert for marketing and physician education outreach

---

REFERENCES

Dr. Sergey Shevkoplyas | Professor, University of Houston | PhD Advisor
+1 (713) 743-5696 | sshevkop@central.uh.edu

Dr. Sean Gifford | Chief Science Officer, Halcyon Biomedical Inc. | Project Leader and Laboratory Supervisor
+1 (617) 459-3915 | scgifford@gmail.com

Dr. Vivien Sheehan M.D. | Assistant Professor, Baylor College of Medicine | Collaboration Supervisor
+1 (832) 822-4362 | vxsheeha@txch.org

B Python Program for Analysis of Paper SCD Diagnostic Stain Scans

```
1.  #Note on python modules used:
2.  #  -
     In order to run this script, you must have the Pillow image processing module (
    https://pypi.python.org/pypi/Pillow/ ). To install it, I typed the command 'pyth
    on -m pip install --
    user pillow' into the terminal. Additional, OS specific installation instruction
    s can be found at http://pillow.readthedocs.io/en/3.4.x/installation.html and ge
    neral information for installing python modules can be found at https://packagin
    g.python.org/installing/ . Feel free to email ktorabian@gmail.com with additiona
    l questions.
3.  #  -
     Other modules may need to be updated. For example, I updated matplotlib by typi
    ng 'python -m pip install --user --upgrade matplotlib' into the terminal.
4.
5.  import numpy as np
6.  import sys as sy
7.  import os as os
8.  import PIL.Image as improc
9.  import PIL.ImageFilter as imfilt
10. import PIL.ImageOps as imops
11. import matplotlib.pyplot as plt
12.
13. #Requests the directory and the name of the image, attempts to load the image as
     a Pillow image object, and returns the image
14. def loadImage(i, imnames, imdir):
15.     #change directory to the 'Images' directory, within the original project dir
    ectory
16.     ordir = os.getcwd()
17.     os.chdir(imdir)
18.     imname = imnames[i]
19.     try:
20.         im = improc.open(imname)
21.     except:
22.         sy.exit("Unable to find/read image file. Make sure image path and name a
    re correct:\npath\: "+imdir+"\nfilename: "+imnames[i])
23.     #Change directory back to original project directory
24.     os.chdir(ordir)
25.     ##Option to print image information
26.     #print "Your image is a "+im.format + ", with dimensions " + str(im.size) +
    ", encoded in " + im.mode + "."
27.     return im
28.
29. #Takes a 1 channel image and returns a 1D list of pixel values/flattened-
    locations and a 2D numpy array with values/location corresponding to each pixel
    of the image.
30. def getImData(inIm):
31.     (numcols, numrows) = inIm.size
32.     pixlist = list(inIm.getdata())
33.     pixarr = np.array(pixlist)
34.     pixarr = pixarr.reshape((numrows, numcols))
35.     return [pixlist, pixarr]
36.
37. #Takes a binary array and calculates the centroid of the 1s (the object made up
    of white pixels)
38. def getCentroid(bwImArr):
39.     (numrows, numcols) = bwImArr.shape
```

```
        centroidx = 0;
        centroidy = 0;
        size = 0;
        for col in range(numcols):
            for row in range(numrows):
                if bwImArr[row,col] != 0:
                    size += 1
                    centroidx += col
                    centroidy += row
        centroidx = int(centroidx/size)
        centroidy = int(centroidy/size)
        centroid = (centroidx, centroidy)
        return centroid

    #Returns a black a white image thresholded around the mean pixel intensity of th
    e input image data pixel list
    def meanThreshIm(pixList):
        meanThresh = np.mean(pixList)

        #internal function used in the eval line below to set all pixel values above
         the threshold to zero and everything else to 1
        def thresh(pint):
            if pint>meanThresh:
                return 0
            return 1

        bwIm = improc.eval(g, thresh)
        #set the black and white image to black and white mode
        bwIm.mode = "1";
        return [meanThresh, bwIm]


    #show centroid as a back x in the bw image (this will permanently change the inp
    ut binary image since it is passed by reference)
    def dispCentroid(bwIm, centroid):
        bwIm.putpixel((centroid[0], centroid[1]), 0)
        bwIm.putpixel((centroid[0]+1, centroid[1]+1), 0)
        bwIm.putpixel((centroid[0]+1, centroid[1]-1), 0)
        bwIm.putpixel((centroid[0]-1, centroid[1]+1), 0)
        bwIm.putpixel((centroid[0]-1, centroid[1]-1), 0)
        bwIm.show()

    #takes a 1 channel image with a single circular object, and the centroid of the
    single circular object, and grows the radius of the circle from 0 to the smaller
     image dimension, calculating the mean intensity of the pixels inside the circle
     to the mean intensity of the pixels outside the circle, and storing their quoti
    ent (inner/outer) in a vector (list). Plotting the vector along with the radius
    values allows you to visualize circular rings concentric with the object.
    def innerVsOuterCirc(pixArr, centroid):
        (numrows, numcols) = pixArr.shape
        #grow the radius to span the smaller of the 2 diamters of the image (this as
    sumes that the circular stain is roughly centered and completely contained in th
    e rectangular image). Other methods would have to know the diameter of the outer
    most ring of the stain, but that is difficult to make reliable from a software s
    tandpoint because the outermost ring is virtually invisible for stains with 100%
    HbS. Hardware can be used to normalize the volume of the fluid that makes each s
    tain, and the distance from which the photo is captured.
        if numrows <= numcols:
            maxr = int(np.floor(numrows/2))
        else:
```

```
            maxr = int(np.floor(numcols/2))
        inOutVec = []
        for r in range(maxr):
            innermean = 0.0;
            outermean = 0.0;
            innercount = 0;
            outercount = 0;
            #print "Analysis " + str(float(r)/maxr*100) + "% complete:"
            for row in range(numrows):
                for col in range(numcols):
                    dfromcentroid = np.abs(np.sqrt((col-centroid[0])**2+(row-
centroid[1])**2))
                    if dfromcentroid<=r:
                        innermean += pixArr[row, col]
                        innercount += 1
                    else:
                        outermean += pixArr[row,col]
                        outercount +=1
            innermean = innermean/innercount
            outermean = outermean/outercount
            inOutVec.append(innermean/outermean)
        return [range(maxr), inOutVec]

#prints a diagnosis given an image name and image score and the range for each s
core and returns a value of 0 for healthy, 1 for trait, and 2 for disease
def diagnose(score, imageName, ASrange):
    diagnosis = ''
    if score < ASrange[0]:
        diagnosis = 'Healthy -- confirmatory testing not needed'
        d = 0
    elif score < ASrange[1]:
        diagnosis = 'Trait -- recommend for confirmatory testing'
        d = 1
    else:
        diagnosis = 'Sickle Cell Disease --
 strongly recommend for confirmatory testing'
        d = 2
    print("Stain " + imageName + " is diagnosed as " + diagnosis + ".")
    return d

##################################### HELPER FUNCTIONS ABOVE ##################
###################
# #Shortcut directory or image loading for developer
# imdir = 'Images/Real'
# imagenames = ['00HbS_35HCT.jpg', '00HbS_36HCT.jpg','27HbS_25HCT.jpg','32HbS_29
HCT.jpg','50HbS_28HCT.jpg','66HbS_25HCT.jpg','84HbS_22HCT.jpg','86HbS_23HCT.jpg'
]
# #imagenames = ['TestImage1.jpg', 'TestImage2.jpg']

#Load image names from a user input directory. For developing purposes see comme
nted code above.
imagenames = []
imdir = input("Please enter the path of your image directory: ")
valid_images = [".jpg",".gif",".png",".tga", ".jpeg", ".tiff"]
try:
    dirfiles = os.listdir(imdir)
except:
    sy.exit("Unable to find directory " + imdir + " please confirm path.")
for f in dirfiles:
    ext = os.path.splitext(f)[1]
```

```
        if ext.lower() not in valid_images:
            continue
        imagenames.append(f)

    numIms = len(imagenames)
    if numIms <1:
        sy.exit("Unable to find any image files with extension " + str(valid_images)
     + " in directory " + imdir)

    #Some parameters set by the developer after testing, for code to run efficienty
    and provide diagnostic output. The ASrange was learned from the reconstituted me
    tabisulfite data
    ASrange = [3.27,6.42]
    thumbnailsize = (75,75)

    #Some parameters set by the developer for plotting the diagnosis bar graph
    colors = ['g', 'b', 'r']
    barwidth = .8
    maxscore = 0.

    #Main Loop: Loops through each image and performs analysis
    for i in range(numIms):
        #Load and resize image
        im = loadImage(i, imagenames, imdir)
        #resize to ensure the program runs in a decent amount of time
        im = im.resize(thumbnailsize)

        #Do some processing of the loaded image to get 1 channel images that contain
     the ideal information (greatest pixel value contrast between the features in th
    e bloodstains) for this application
        #Split the image by it's color channels
        rgb = im.convert('RGB')
        r,g,b = rgb.split()
    #    #Can also make a grayscale converted verion if desired
    #    gray = im.convert('L')

        #Use the green channel since that provides the most contrast between the whi
    te background and the red/blue center circle points
        im = g


        #Filter the image with a gaussian filter of radius 5 to blur irregularities
    caused by the uneven surface of the chromatogrpahy paper
        im = im.filter(imfilt.GaussianBlur(5))

        #get the pixel data for the green channel image as a 1D flattened list and a
     2D array
        [gpixlist, gpixarr] = getImData(im);

        #Find the centroid of the image
        #Threshold the green channel image using its mean pixel intensity to produce
     a binary image with a white object on a black background. The white object will
     almost always be one of the circles/rings in the input blood stain.
        [thresh, bw] = meanThreshIm(gpixlist)
        ##Option to print the calculated threshold
        #print "Your black and white threshold is " + str(thresh)
        #get the pixel data for the black and white image
        [bwpixlist, bwpixarr] = getImData(bw)
        #calculate the centroid of the thresholded image
        centroid = getCentroid(bwpixarr)
```

```
189.        ##Option to display the black and white image with an x over its centroid
190.        #dispCentroid(bw, centroid);
191.
192.        #Use the inverse of the blue channel and a mask over the inner circle to mat
        ch published MatLab code
193.        im = imops.invert(b)
194.        innerCirc = 12
195.        #Filter the image with a gaussian filter of radius 5 to blur irregularities
        caused by the uneven surface of the chromatogrpahy paper
196.        #im = im.filter(imfilt.GaussianBlur(5))
197.        #Median Filter optional
198.        #im = im.filter(imfilt.MedianFilter(5))
199.
200.        [bipixlist, bipixarr] = getImData(im);
201.        #Use the greenchannel image and the centroid of the stain to analyze the col
        or intensity of circular regions concentric with the stain, to produce a signal
        that can provide a diagnosis
202.        #Take the centroid as the center of a circle that we will grow incrementaly,
         each time calculating the mean pixel intesity on the inside of the circle divid
        ed by the mean pixel intensity on the outside of the circle.
203.        [radiusVals, inOutVals] = innerVsOuterCirc(bipixarr, centroid)
204.        #The max of this intensity ratio signal (found at the radius of the inner ci
        rcle) can be used to approximate a diagnosis for the stain
205.        score = inOutVals[innerCirc]
206.        d = diagnose(score, imagenames[i], ASrange)
207.
208.        #Plot the signal and the diagnosis for all the stains in your directory
209.        if score>maxscore:
210.            maxscore = score
211.        plt.figure(1)
212.        plt.plot(radiusVals, inOutVals, label = imagenames[i])
213.        plt.figure(2)
214.        plt.bar(i, score, barwidth, color = colors[d])
215.
216.    #Build and format the plots that show the signals and diagnoses for all of the s
        tains
217.    #To plot entire inner/outer signal
218.    plt.figure(1)
219.    plt.title('Signals Used for Diagnosis of Each Input Image')
220.    plt.xlabel('Circle radius from centroid (px)')
221.    plt.ylabel('Mean pixel intensity ratio between inner and outer circle (inner/out
        er)')
222.    #plt.legend(bbox_to_anchor=(1, 0), loc=3, borderaxespad=2.)
223.    plt.savefig("signals")
224.
225.    #To plot scores for diagnosis
226.    plt.figure(2)
227.    plt.title('Diagnoses for Each Input Image')
228.    plt.xlabel('Image')
229.    plt.ylabel('Diagnosis Value')
230.    plt.xticks(np.arange(numIms), imagenames, rotation = 'vertical')
231.    plt.subplots_adjust(bottom = .30)
232.    ylims = [0, maxscore+1]
233.    ylims = plt.gca().set_ylim(ylims)
234.    ylabels = ['Healthy', 'Trait', 'Disease']
235.    plt.yticks([ylims[0]+(ASrange[0]-ylims[0])/2, ASrange[0]+(ASrange[1]-
        ASrange[0])/2, ASrange[1]+(ylims[1]-
        ASrange[1])/2], ylabels, rotation = 'vertical')
236.    plt.hlines(ASrange[0], -barwidth/2, numIms-
        barwidth/2, linestyles = 'dashed', label = ylabels[1])
```

```
237.    plt.hlines(ASrange[1], -barwidth/2, numIms-
        barwidth/2, linestyles = 'dashed', label = ylabels[2])
238.    plt.savefig("diagnoses")
239.
240.    plt.show()
```